

# Designing a fully-tunable and versatile TKE-1 turbulence parameterization for atmospheric models

Étienne VIGNON<sup>1</sup>, Khadija ARJDAL<sup>2</sup>, Frederique Cheruy<sup>3</sup>, Maëlle coulondcorzens<sup>4</sup>, Clément Dehondt<sup>5</sup>, Thomas Dubos<sup>6</sup>, Sébastien Fromang<sup>7</sup>, Frédéric Hourdin<sup>6</sup>, Lucas Lange<sup>8</sup>, Lea Raillard<sup>4</sup>, Gwendal Rivière<sup>4</sup>, Romain Roehrig<sup>9</sup>, Adriana Sima<sup>10</sup>, Aymeric Spiga<sup>11</sup>, and Pierre Tiengou<sup>12</sup>

<sup>1</sup>CNRS

<sup>2</sup>Mohammed VI Polytechnique university

<sup>3</sup>French National Centre for Scientific Research (CNRS)

<sup>4</sup>Laboratoire de Météorologie Dynamique

<sup>5</sup>LSCE

<sup>6</sup>LMD

<sup>7</sup>Laboratoire AIM, CEA/DSM-CNRS-Université Paris 7, Irfu/Departement d'Astrophysique

<sup>8</sup>Laboratoire de Météorologie Dynamique, Institut Pierre-Simon Laplace (LMD/IPSL),

Sorbonne Université, Centre National de la Recherche Scientifique (CNRS), École Polytechnique

<sup>9</sup>CNRM, Université de Toulouse, Météo-France, CNRS

<sup>10</sup>Laboratoire de Météorologie Dynamique, Sorbonne Université / CNRS / École Normale Supérieure

<sup>11</sup>Laboratoire de Météorologie Dynamique/Institut Pierre-Simon Laplace (LMD/IPSL), CNRS, Sorbonne Université

<sup>12</sup>METIS

April 26, 2024

## Abstract

This study presents the development of a TKE-1 parameterization of the diffusion coefficients for the representation of turbulent diffusion in neutral and stable conditions in large-scale atmospheric models. The parameterization has been carefully designed to be completely tunable in the sense that all adjustable parameters have been clearly identified and their number minimized as much as possible to help the calibration and to thoroughly assess the parametric sensitivity. We choose a mixing length formulation that depends on both static stability and wind shear to cover the different regimes of stable boundary layers. We follow a heuristic approach for expressing the stability functions and turbulent Prandtl number in order to guarantee the versatility of the scheme and its applicability for planetary atmospheres composed of an ideal and perfect gas such as that of Earth and Mars. Particular attention has also been paid to the numerical stability at typical time steps used in General Circulation Models. Test, parametric sensitivity assessment and preliminary tuning are performed on single-column idealized simulations of the weakly stable boundary layer. The robustness and versatility of the scheme are also assessed through its implementation in the LMDZ General Circulation Model and the Mars Planetary Climate Model and by running simulations of the Antarctic and Martian nocturnal boundary layers.

# Designing a fully-tunable and versatile TKE-1 turbulence parameterization for atmospheric models

É. Vignon<sup>1</sup>, K. Arjdal<sup>1,2</sup>, F. Cheruy<sup>1</sup>, M. Coulon-Decorzens<sup>1</sup>, C. Dehondt<sup>3</sup>, T.  
Dubos<sup>1</sup>, S. Fromang<sup>3</sup>, F. Hourdin<sup>1</sup>, L. Lange<sup>1</sup>, L. Raillard<sup>1</sup>, G. Rivière<sup>1</sup>, R.  
Roehrig<sup>4</sup>, A. Sima<sup>1</sup>, A. Spiga<sup>1</sup>, P. Tiengou<sup>1,5</sup>

<sup>1</sup>Laboratoire de Météorologie Dynamique- IPSL, Sorbonne Université/CNRS/ Ecole Normale

Supérieure-PSL Université/ Ecole Polytechnique-Institut Polytechnique de Paris, Paris, France

<sup>2</sup>International Water Research Institute (IWRI), CSAES - Mohammed VI Polytechnic University,

Benguerir, Morocco

<sup>3</sup>Laboratoire des Sciences du Climat et de l'Environnement, LSCE/IPSL, CEA-CNRS-UVSQ, Université

Paris-Saclay, F-91191, Gif-sur-Yvette, France.

<sup>4</sup>CNRM, Université de Toulouse, Météo-France, CNRS, Toulouse, France

<sup>5</sup>Milieux environnementaux, transferts et interaction dans les hydrosystèmes et les sols (Metis)/Sorbonne

Université/IPSL/CNRS/ EPHE, Paris, France

## Key Points:

- A simple TKE-1 turbulent diffusion scheme is developed in a semi-heuristic way for applications in models of the Earth and Mars atmospheres.
- The parameterization is designed to be completely tunable and numerically stable at typical GCM time steps.
- The parameterization is tuned over 1D simulations and is able to capture the Antarctic and Martian stable boundary layers in 3D simulations.

---

Corresponding author: Étienne Vignon, [etienne.vignon@lmd.ipsl.fr](mailto:etienne.vignon@lmd.ipsl.fr)

## Abstract

This study presents the development of a TKE-1 parameterization of the diffusion coefficients for the representation of turbulent diffusion in neutral and stable conditions in large-scale atmospheric models. The parameterization has been carefully designed to be completely tunable in the sense that all adjustable parameters have been clearly identified and their number minimized as much as possible to help the calibration and to thoroughly assess the parametric sensitivity. We choose a mixing length formulation that depends on both static stability and wind shear to cover the different regimes of stable boundary layers. We follow a heuristic approach for expressing the stability functions and turbulent Prandtl number in order to guarantee the versatility of the scheme and its applicability for planetary atmospheres composed of an ideal and perfect gas such as that of Earth and Mars. Particular attention has also been paid to the numerical stability at typical time steps used in General Circulation Models. Test, parametric sensitivity assessment and preliminary tuning are performed on single-column idealized simulations of the weakly stable boundary layer. The robustness and versatility of the scheme are also assessed through its implementation in the LMDZ General Circulation Model and the Mars Planetary Climate Model and by running simulations of the Antarctic and Martian nocturnal boundary layers.

## Plain Language Summary

In planetary atmospheres, turbulent motions actively contribute to the mixing of quantities such as heat, momentum and chemical species. Such motions are not resolved in coarse-grid atmospheric models and have to be parameterized. The parameterization of turbulent mixing should be based on physical laws and sufficiently sophisticated to realistically represent the full spectrum of motions over the full range of stability encountered in the atmospheres. However, it also necessarily contains a number of closure parameters not always well identified and whose values are determined empirically - thereby questioning the universality of the parameterization and its potential application over the full globe or even to other planets - or adjusted to guarantee the numerical stability of the model. This study presents the design of a turbulent mixing parameterization that can be fully calibrated and applied in planetary atmospheres such as that of Mars. We then calibrate the parameterization on an idealised simulation set-up and test its robustness and performance by running simulations of the Antarctic and Martian atmospheres.

## 1 Introduction

Turbulence efficiently transports momentum, energy, moisture and matter in the atmosphere, particularly in the planetary boundary layer where it controls sensible and latent heat fluxes as well as the transfer of momentum between the air and the ground surface. It thereby directly affects the diurnal cycle of the near-surface atmospheric quantities and also impacts on the lifetime and structure of synoptic-scale dynamical systems. Turbulent transport is therefore an essential component of the physics of climate models, numerical weather prediction models and more generally of General Circulation Models (GCMs) of planetary atmospheres. As turbulent eddies manifests on scales ranging from a few millimeters to a few tens of kilometers in deep convective systems, modellers develop conceptually separated subgrid parameterizations targeting different types - or different scales - of transport processes. Non-local turbulent transport resulting from large and organised convective cells, being deep or shallow, is often treated with so-called mass flux schemes (e.g., Tiedtke (1989); Emanuel (1991); Hourdin et al. (2002); Golaz et al. (2002)). Local turbulent mixing which results from eddies whose typical size is smaller or similar to the typical grid cell thickness - namely a few tens of meters - is often parameterized with a local K-gradient diffusion scheme. In those schemes, the turbulent flux is parameterized with a Fick's law type down-gradient diffusion formulation that relies on the introduction of a turbulent diffusion coefficient. Such schemes are particularly critical to simulate the stable and neutral

72 atmospheric boundary layers (Delage, 1997; Cuxart et al., 2006; Sandu et al., 2013), the  
 73 land-atmosphere coupling as well as the thermal inversion at the top of convective boundary  
 74 layers.

75 Several K-gradient diffusion parameterizations have been developed since the pioneering  
 76 work of Louis (1979) and have been the subject of a substantial body of literature in at-  
 77 mospheric sciences. Among them, the moderate-complexity 1.5 order schemes, or TKE-l  
 78 schemes, consist in expressing the diffusion coefficients as function of a diagnostic vertical  
 79 turbulent length-scale, or mixing length, and of a prognostic estimation of the Turbulent  
 80 Kinetic Energy (TKE) (Mellor & Yamada, 1982; Yamada, 1983).

81 The closure of the TKE evolution equation and the empirical and/or heuristic formu-  
 82 lation of the mixing-length necessarily introduce free parameters in the parameterization,  
 83 and therefore a certain degree of empiricism in the expression of the diffusion coefficients (Li  
 84 et al., 2016). Indeed, such parameters do not have, by essence, fixed and universal values.  
 85 Some of them - and the associated variability range thereof - are determined empirically  
 86 using field observations, laboratory experiments, Large Eddy Simulations (LES) or Direct  
 87 Numerical Simulations (DNS) while others are arbitrarily set. In practice, in climate and  
 88 numerical weather prediction models, the value of some coefficients is often retuned to match  
 89 large-scale or meteorological targets. For instance as all subgrid mixing processes are not  
 90 parameterized - such as small scale internal waves or submeso-scale motions - the mixing in  
 91 stable conditions is often artificially enhanced to prevent unrealistic runaway surface cool-  
 92 ing due to surface-atmosphere mechanical decoupling and to maintain sufficient surface drag  
 93 and Ekman pumping in extratropical cyclones (Holtslag et al., 2013; Sandu et al., 2013).  
 94 Such empiricism and Earth-oriented tuning can somewhat question the applicability of these  
 95 turbulent mixing parameterizations in planetary GCMs, even in GCMs of Mars (e.g., Forget  
 96 et al. (1999); Colaitis et al. (2013)) where the planetary boundary layer shares similarities  
 97 with that on Earth (Spiga et al., 2010a).

98 In addition, arbitrary parameter calibration - sometimes beyond reasonable ranges -  
 99 is often required to improve the numerical convergence and stability of the parameteriza-  
 100 tion once it is implemented in models with typical physics time steps of a few minutes to  
 101 a few tens of minutes. Indeed, the numerical implementation of a K-gradient turbulence  
 102 scheme is prone to spurious oscillations called ‘fibrillations’ (Kalnay & Kanamitsu, 1988;  
 103 Girard & Delage, 1990). Such fibrillations are due to *i*) the coupling between momentum  
 104 and potential temperature via the turbulent diffusion coefficients and *ii*) the discretization  
 105 of the vertical diffusion in which the nonlinear exchange coefficient is often treated explicitly  
 106 in time. Even though the TKE budget is often close to a local equilibrium (Lenderink &  
 107 Holtslag, 2004), the prognostic prediction of the TKE generally makes TKE-l schemes less  
 108 sensitive to the time discretization and less prone to fibrillation than traditional first-order  
 109 schemes (Bougeault & Lacarrère, 1989; Bazile et al., 2011) in which the diffusion coefficients  
 110 are explicit and diagnostic functions of the mean static stability and wind shear (Louis, 1979;  
 111 Louis et al., 1982; Delage, 1997). This is mostly explained by the fact that the prognostic  
 112 TKE plays a role of ‘reservoir’ that damps the sometimes abrupt evolution of the diffusion  
 113 coefficients with time (Mašek et al., 2022). However, even TKE-based schemes can also  
 114 be affected by numerical instabilities which can be related to the numerical treatment of  
 115 the TKE equation itself (Deleersnijder, 1992; Vignon et al., 2018) or to the coupling with  
 116 other prognostic quantities such as the turbulent potential energy (Mašek et al., 2022). The  
 117 numerical treatment of the TKE equation and more generally of the turbulent diffusion  
 118 thereby comes out as a forefront issue in atmospheric modeling. Hence, one has to find  
 119 a good trade-off between the complexity and sophistication of a turbulent mixing scheme  
 120 and its practical implementation in large scale atmospheric models avoiding as much as  
 121 possible unrealistic parameter calibration to guarantee numerical stability and fair model  
 122 performances.

123

The sensitivity of the stable boundary layer representation to turbulent diffusion calibration in a large scale atmospheric model was assessed in a game-changing study by Audouin et al. (2021) using a semi-automatic tuning tool based on uncertainty quantification (Couvreur et al., 2021; Hourdin et al., 2021). The authors identified a few key tuning parameters - and their acceptable ranges of values - in the TKE-1 turbulent diffusion scheme of the ARPEGE-Climat model and assessed to what extent biases in the simulation of the extremely stable Antarctic boundary layer are explained by structural parameterization deficiencies or tuning choices. However, the boundary layer and surface layer schemes of ARPEGE-Climat contain a large number of tuning parameters, sometimes subtly interdependent, and considering all of them in a tuning exercise may be confusing, thereby challenging.

The present study aims to design a new and simple TKE-1 turbulent diffusion scheme for large scale atmospheric models

1. that is sufficiently robust and versatile to be applicable on both Earth and Mars, and potentially on other planetary atmospheres and ;
2. that is built to be completely tuned in the sense that all adjustable parameters are clearly identified and their number minimized to help the calibration - or parameter adjustment - and assess the parametric sensitivity.

The scheme will be referred to as the ATKE scheme - for Adjustable TKE-1 scheme - in the paper.

We follow a simple heuristic approach - as in Lenderink and Holtslag (2004) and He et al. (2019) - for expressing the stability functions and turbulent Prandtl number to guarantee the versatility of the scheme and its potential applicability for planetary atmospheres composed of an ideal and perfect gas. A particular attention is also paid to the numerical treatment of the TKE prognostic equation to ensure the numerical stability even in conditions of strong wind shear or strong stratification. It is worth emphasizing that the ‘local’ nature of the scheme makes it mostly adapted for neutral and stably stratified conditions, hence the particular focus on stable boundary layers in the paper. The scheme is tested and tuned - using the same Uncertainty Quantification approach as in Audouin et al. (2021) and Hourdin et al. (2021) - on idealized single column simulations of the stable boundary layer. The parameterization is then implemented and tested in the Earth LMDZ GCM (Hourdin et al., 2020; Cheruy et al., 2020) and the Mars Planetary Climate model (Forget et al., 1999) to verify its robustness and assess its performances when challenging the stable Antarctic and Martian nocturnal boundary layers.

## 2 Parameterization development

This section presents the derivation of the ATKE scheme, starting briefly and purposely with some generalities to clearly set the parameterization in the framework of turbulent diffusion in GCMs of planetary atmospheres.

### 2.1 General framework

The conservation law for an extensive quantity  $c$  - being for example the potential temperature, wind components or concentration in chemical species - in a compressible atmosphere reads:

$$\frac{\partial \rho c}{\partial t} + \vec{\nabla}(\rho \vec{u} c) = P_c \quad (1)$$

With, in Cartesian coordinates  $(x, y, z)$ ,  $\vec{u} = u\vec{i} + v\vec{j} + w\vec{k}$  the wind vector,  $\rho$  the air density and  $P_c$  the net source/loss term. We note the statistical (ensemble) average with

an overline and introduce the air weighting average operator  $\sim$  such that

$$\tilde{c} = \frac{\overline{\rho c}}{\bar{\rho}} \quad (2)$$

Note that  $\tilde{c}$  is an extensive variable per mass unit. We decompose  $c$  into a mean state and a fluctuation such that  $c = \tilde{c} + c'$ . We then apply the statistical average operator (overline) on Eq. 1 that now reads:

$$\underbrace{\frac{\partial \overline{\rho \tilde{c}}}{\partial t} + \vec{\nabla}(\overline{\rho \tilde{c} \tilde{u}})}_{(1)} = - \underbrace{\vec{\nabla}(\overline{\rho \tilde{u}' c'}) + \overline{P_c}}_{(2)} \quad (3)$$

In large-scale atmospheric models the scale separation is imposed by the size of the grid cells which determines the resolved and unresolved components. In this framework, the term (1) in Eq.3 is handled by the dynamical core while the term (2) is the essence of the physical subgrid parameterizations. Further assuming that the subgrid horizontal variations of  $c$  are dominated by vertical variations, it follows that  $\vec{\nabla}(\overline{\rho \tilde{u}' c'}) \approx \partial_z(\overline{\rho w' c'})$ . A local turbulent mixing parameterization aims at calculating a tendency on the mean state variable  $\tilde{c}$  due to the vertical turbulent diffusion as follows:

$$\left. \frac{\partial \tilde{c}}{\partial t} \right|_{diffusion} = - \frac{1}{\bar{\rho}} \frac{\partial \overline{\rho w' c'}}{\partial z} \quad (4)$$

163 For better readability and conciseness, we leave the  $\sim$  notation out for mean state quantities  
 164 and note  $\rho = \bar{\rho}$  in the following.

For local and mostly shear driven turbulent eddies, the mixing of any conservative quantity during turbulent mixing - such as the common Betts (1973)' variables - can be represented as a diffusive process (e.g. Louis (1979)). Turbulent fluxes can then be expressed with a down-gradient form:  $\overline{\rho w' c'} = -\rho K_c \partial_z c$ ,  $K_c$  being a diffusion coefficient. Eq. 4 hence reads:

$$\left. \frac{\partial c}{\partial t} \right|_{diffusion} = \frac{1}{\rho} \frac{\partial}{\partial z} \left( \rho K_c \frac{\partial c}{\partial z} \right) \quad (5)$$

165 Once the  $K_c$  coefficient has been calculated at vertical model layer interfaces, such an  
 166 equation can be numerically solved with an implicit approach through the inversion of a  
 167 tri-diagonal matrix.

We now focus on the closure of the  $K_c$  coefficient which is the main scope of the present study. We follow here an approach historically proposed by Mellor and Yamada (1974); Yamada (1975) that is, a 1.5 order closure or TKE-1 scheme. In this framework,  $K_c$  coefficients are expressed as the product of a vertical turbulent length scale or mixing length  $l$  with a turbulent vertical velocity scale taken proportional to the square root of the TKE  $e = \frac{1}{2}(\overline{u'^2} + \overline{v'^2} + \overline{w'^2})$ . The latter is multiplied by a stability function  $S_c$  that accounts for the fact that the turbulence anisotropy - thus the contribution of TKE to vertical turbulent mixing - varies with the local stability of the atmosphere characterized by the gradient Richardson number  $Ri$ . The diffusion coefficient  $K_c$  is then expressed as (Yamada, 1983; Zilitinkevich et al., 2007):

$$K_c = l S_c (Ri) \sqrt{e} \quad (6)$$

168 In the following sections, we describe the estimation of the three different terms of  $K_c$ ,  
 169 namely  $e$ ,  $S_c$  and  $l$ . As we want our turbulent scheme to be applicable on Earth and Mars  
 170 (and potentially other planetary environments), we have to ensure that their expressions  
 171 are as planet-independent as possible.

172

## 2.2 TKE prognostic equation

173

### 2.2.1 Parameterization of the source and loss terms

Assuming the horizontal homogeneity of the subgrid-scale statistics, the TKE obeys the following evolution equation (Stull, 1990):

$$\frac{\partial e}{\partial t} = \underbrace{-\overline{u'w'}\frac{\partial u}{\partial z} - \overline{v'w'}\frac{\partial v}{\partial z}}_{\mathcal{W}} + \underbrace{\overline{b'w'}}_{\mathcal{B}} - \underbrace{\frac{1}{\rho}\frac{\partial}{\partial z}(\overline{\rho w'e} + \overline{w'p'})}_{\mathcal{T}} \underbrace{-\epsilon}_{\mathcal{D}} \quad (7)$$

174

175

$\mathcal{W}$  is the wind shear production term that can be expressed with the down-gradient expression of fluxes with a diffusion coefficient for momentum hereafter denoted as  $K_m$ :

$$-\overline{u'w'}\frac{\partial u}{\partial z} - \overline{v'w'}\frac{\partial v}{\partial z} = K_m S^2 = l S_m \sqrt{e} S^2 \quad (8)$$

with  $S^2 = (\partial_z u)^2 + (\partial_z v)^2$  the wind shear and  $S_m$  the stability function for momentum.  $\mathcal{B}$  is the buoyancy  $b$  production/consumption term. For a dry air under the ideal gas assumption, one can write:

$$\overline{b'w'} = \frac{-g}{\rho} \left. \frac{\partial \rho}{\partial \theta} \right|_p \overline{w'\theta'} = \frac{g}{\theta} \overline{w'\theta'} = -K_h \frac{g}{\theta} \frac{\partial \theta}{\partial z} = -K_h N^2 = -l S_h \sqrt{e} N^2 \quad (9)$$

where  $g$  is the gravity acceleration of the planet,  $\theta$  the potential temperature,  $N$  the Brünt-Väisälä pulsation,  $K_h$  the diffusion coefficient for heat and  $S_h$  the stability function for heat. In the case of an atmosphere containing water vapor or chemical species  $\xi$ , buoyancy reads  $\overline{b'w'} = \frac{-g}{\rho} \left( \left. \frac{\partial \rho}{\partial \theta} \right|_{p,\xi} \overline{w'\theta'} + \left. \frac{\partial \rho}{\partial \xi} \right|_{p,\theta} \overline{w'\xi'} \right)$ . For water vapor - in absence of phase change - or for non-reactive chemical species, one can define a virtual temperature  $T_v$  (and a subsequent virtual potential temperature  $\theta_v$ ) corresponding to the temperature that dry air would have if its pressure and density were equal to those of a given sample of the mixture of gas. In this case:

$$\overline{b'w'} \simeq \frac{g}{\theta_v} \overline{w'\theta'_v} = -\frac{g}{\theta_v} K_h \frac{\partial \theta_v}{\partial z} \quad (10)$$

176

177

178

179

180

181

182

It is worth noting here that the expression of the buoyancy term (or Brünt-Väisälä pulsation) is gravity-dependent thus planet-dependent. For simplicity and consistency with previous literature on turbulent mixing schemes, we keep the formalism with explicit gravity in the following. However, a more universal derivation of the scheme can be achieved with a gravity-invariant formulation of the TKE and turbulent diffusion equations. Such a formulation is proposed in Appendix A.

$\mathcal{D}$  is the viscous TKE dissipation term that can be expressed following Kolmogorov (1941):

$$\epsilon = \frac{e^{3/2}}{l_\epsilon} \quad (11)$$

183

184

185

186

187

188

189

190

with  $l_\epsilon$  the dissipation length-scale characterizing the size of the most dissipative and energy-containing eddies. Following for instance Yamada (1983) and Bougeault and Lacarrère (1989), we assume that  $l_\epsilon$  scales with  $l$  such that  $l_\epsilon = c_\epsilon l$ ,  $c_\epsilon$  being a scalar. Its value roughly ranges between 1.2 and 10.0 (Yamada, 1983; Audouin et al., 2021; He et al., 2019) since dissipation length scale - characterizing the dissipation of turbulence as a whole - might be larger than vertical mixing length in stable conditions due to the fact that kinetic energy can dissipate through wavy motion with little transfer to the smaller turbulent scales (Cuxart et al., 2006).

The vertical turbulent flux of TKE and the pressure term gathered in  $\mathcal{T}$  redistribute TKE through the depth of the atmospheric column. Hence, those two terms are commonly

grouped together and expressed as a TKE turbulent diffusion term:

$$-\frac{1}{\rho} \frac{\partial}{\partial z} (\overline{\rho w' e} + \overline{w' p'}) = \frac{1}{\rho} \frac{\partial}{\partial z} (\rho K_e \frac{\partial e}{\partial z}) \quad (12)$$

191  $K_e$  being taken proportional to  $K_m$  (Yamada, 1983; Bougeault & Lacarrère, 1989;  
 192 Lenderink & Holtslag, 2004):  $K_e = c_e K_m$ .  $c_e$  is a constant whose value is generally around  
 193 1 - 2 and that we will arbitrarily allow to vary between 1 and 5 (Bougeault & Lacarrère,  
 194 1989; Lenderink & Holtslag, 2004; Baas et al., 2018). The lower boundary condition of  $e$   
 195 that is, the surface value of the TKE  $e_s$ , is estimated by assuming stationary near-neutral  
 196 conditions in the surface layer. On such a condition (Baas et al., 2018; Lenderink & Holtslag,  
 197 2004):

$$e_s = c_s u_*^2 \quad (13)$$

with  $c_s$  a constant and  $u_*$  the surface friction velocity calculated from the surface drag  
 coefficient for momentum and the wind speed at the first model level. A proper scaling of  
 the TKE-l parameterization with the Monin-Obukhov similarity in the surface layer requires  
 (He et al., 2019):

$$c_s = c_\epsilon^{2/3} \quad (14)$$

### 198 **2.2.2 Numerical treatment**

199 Once the different TKE source and loss terms have been expressed, Eq. 7 has to be  
 200 integrated in time. The numerical treatment of Eq. 7 is critical as the solution must be  
 201 stable and converge at typical physical time steps used in atmospheric GCMs namely, of  
 202 the order of  $\approx 15$  min. Several methods have been proposed in the literature, particularly  
 203 regarding the treatment of the dissipation term with different degrees of implicitation (Bazile  
 204 et al., 2011).

205 Here, we propose a 2-step resolution method which allows for an exact treatment of  
 206 the dissipation term - under some assumptions - while the transport term is calculated  
 207 separately.

208 *Step 1* We calculate the TKE tendency due to the shear, buoyancy and dissipation  
 209 terms. Noting  $q = \sqrt{2e}$ , one can rewrite Eq. 7 with no transport term as:

$$\frac{\partial q}{\partial t} = \frac{l S_m}{\sqrt{2}} S^2 \left( 1 - \frac{Ri}{Pr} \right) - \frac{q^2}{2^{3/2} c_\epsilon l} \quad (15)$$

210 with  $Pr = \frac{K_m}{K_h} = \frac{S_m}{S_h}$  the turbulent Prandtl number. We then solve this equation through  
 211 an implicit treatment of  $q$  assuming that the mean temperature and wind field does not  
 212 vary much during the time step  $\delta t$  and thus keeping the explicit value - that is the value at  
 213 the beginning of the time step - of  $Ri$ ,  $S_m$ ,  $Pr$  and  $l$ . Eq. 16 then reads:

$$\frac{q_{t+\delta t} - q_t}{\delta t} = \frac{l S_m}{\sqrt{2}} S^2 \left( 1 - \frac{Ri}{Pr} \right) - \frac{q_{t+\delta t}^2}{2^{3/2} c_\epsilon l} \quad (16)$$

than can be rewritten in a second-order polynomial form after some rearrangement :

$$q_{t+\delta t}^2 + A_t q_{t+\delta t} + B_t = 0 \quad (17)$$

214 with  $A_t = \frac{c_\epsilon l 2^{3/2}}{\delta t}$  and  $B_t = -\left( \frac{q_t c_\epsilon l 2^{3/2}}{\delta t} + 2l^2 c_\epsilon S_m S^2 \left( 1 - \frac{Ri}{Pr} \right) \right)$

215 One can show that given the choice we will make for the formulation of the turbulent  
 216 Prandtl number in the next section,  $Ri/Pr$  namely the flux Richardson number, is by con-  
 217 struction always  $< 1$ . This in fact reflects a condition imposed by steady-state TKE budget

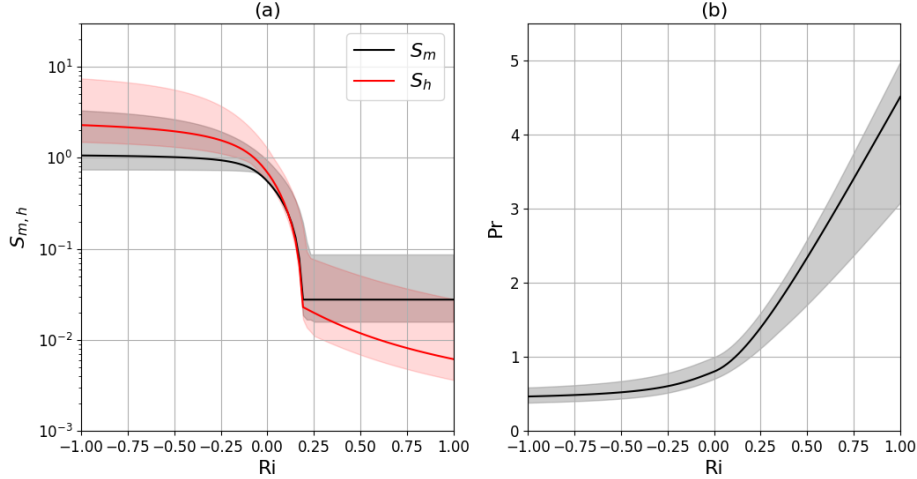


**Figure 1.**  $S_{m,h}$  (panel a) and  $Pr$  (panel b) as functions of the Richardson number  $Ri$  following Eq. 20 and 23. Envelopes show the range of variation when adjustable parameters evolve in their range of acceptable values (Table 1). Solid lines show the curves for the following arbitrary set of parameters' values:  $c_\epsilon = 5.9$ ,  $Pr_n = 0.8$ ,  $\alpha_{Pr} = 4.5$ ,  $r_\infty = 2$ ,  $Pr_\infty = 0.4$ ,  $S_{min} = 0.05$  and  $Ri_c = 0.2$ .

218 equation for which the wind shear production term and the buoyancy term cannot exceed  
 219 unity to maintain a non-zero TKE dissipation thus a non-zero turbulence (e.g, Zilitinkevich  
 220 et al. (2008)).

The discriminant  $\Delta = A_t^2 - 4B_t$  of Eq. 17 is thus always  $> 0$  and the latter always admits a positive solution for  $q$  thus  $e$  that reads:

$$e = \frac{(-A_t + \sqrt{\Delta})^2}{8} \quad (18)$$

221 *Step 2* The TKE variation due to the transport term  $\mathcal{T}$  is then calculated and added  
 222 to the value found in step 1. The calculation of this term consists in resolving the following  
 223 equation:

$$\frac{\partial e}{\partial t} = \frac{1}{\rho} \frac{\partial}{\partial z} \left( \rho K_e \frac{\partial e}{\partial z} \right) \quad (19)$$

224 With an *a priori* knowledge of  $K_e$  - namely an explicit value of  $K_e$  calculated with the  $e$   
 225 value from Step 1 - Eq 19 is a typical diffusion equation that is solved implicitly in time  
 226 through a tri-diagonal matrix inversion (Dufresne & Ghattas, 2009).

### 227 **2.3 Heuristic expressions for the stability functions and turbulent Prandtl** 228 **number**

229 We now have to derive a heuristic expression for the stability function  $S_m$  of the  
 230 gradient Richardson number  $Ri = N^2/S^2$  to be used in the formulation of the diffusion  
 231 coefficient for momentum. On one hand,  $S_m$  should increase when an atmospheric layer  
 232 locally becomes more unstable and thus with decreasing negative  $Ri$ . On another hand, we  
 233 want to prevent  $S_m$  from reaching infinite value when  $Ri \rightarrow -\infty$  to avoid risk of numerical  
 234 instabilities when  $K_m \rightarrow \infty$  (Lenderink & Holtslag, 2000). It is worth recalling here that

235 in unstable conditions, turbulent transport becomes non-local and another type of parame-  
 236 terization such as a mass-flux scheme should come in support of the K-diffusion. In stable  
 237 conditions as turbulent mixing intensity decreases with increasing stability, we assume a  
 238 simple linear decrease with  $Ri$  down to a minimum value attained when the Richardson  
 239 number equals a critical value (Mellor & Yamada, 1974).

Following Lenderink and Holtslag (2004), we propose the following expression for  $S_m$   
 plotted in Figure 1a:

$$S_m(Ri) = \begin{cases} c_n + \frac{2}{\pi}(c_\infty - c_n) \arctan\left(\frac{-Ri}{Ri_0}\right) & \text{if } Ri < 0 \\ \max\left(c_n\left(1 - \frac{Ri}{Ri_c}\right), S_{min}\right) & \text{if } Ri \geq 0 \end{cases} \quad (20)$$

240  $c_n$  is the value of  $S_m$  at  $Ri = 0$  and  $c_\infty$  is the  $S_m$  value in the convective limit.  
 241  $r_\infty = c_\infty/c_n$  is comprised between 1.2 and 5 (Mellor & Yamada, 1982; Lenderink & Holtslag,  
 242 2004).  $Ri_c$  is a critical Richardson number whose inverse value controls the slope of  $S_m$  in  
 243 stable conditions. Previous literature suggests  $Ri_c$  values comprised between 0.19 and 0.25  
 244 (Mellor & Yamada, 1974, 1982; He et al., 2019). As the turbulence vertical anisotropy does  
 245 not reach 0 in very stable conditions (Zilitinkevich et al., 2007; Li et al., 2016),  $S_m$  must be  
 246 lower-bounded by a value  $S_{min}$  which is roughly around 0.05 and that we will make vary  
 247 between 0.025 and 0.1.

The continuity in slope for  $Ri = 0$  further gives:

$$Ri_0 = \frac{2}{\pi}(c_\infty - c_n) \frac{Ri_c}{c_n} \quad (21)$$

Furthermore, the so-called local-scaling similarity theory in stable boundary layers (Nieuwtsadt,  
 1984; Derbyshire, 1990; van de Wiel et al., 2010) implies that in stationary conditions, tur-  
 bulent fluxes and vertical gradient wind speed must scale such that  $\frac{K_m}{lS^2}$  converges towards  
 1 in the neutral limit. This conditions leads to a direct relationship between  $c_n$  and the  
 coefficient  $c_\epsilon$  (Baas et al., 2018; He et al., 2019), the latter being the ratio between the  
 mixing length  $l$  and the TKE dissipation length scale (Sect. 2.2.1):

$$c_n = c_\epsilon^{-1/3} \quad (22)$$

248 The stability function for the heat flux  $S_h$  is estimated through a parametrization of the  
 249 turbulent Prandtl number  $Pr$ . Under unstable conditions, the dominant coherent structures  
 250 such as rising plumes and thermals have vertical velocity anomalies which generally better  
 251 correlate with buoyancy and temperature anomalies than momentum anomalies in average.  
 252 Therefore, one expects  $Pr$  to decrease with increasing instability (Li, 2019). In stably  
 253 stratified conditions, buoyancy is expected to suppress the transport of heat but the existence  
 254 of gravity waves can maintain some transport of momentum inducing an increase in  $Pr$  with  
 255 increasing stability. Collection of field experiments, laboratory data and LES and DNS  
 256 results shows a consistent increase in  $Pr$  with  $Ri$  with a asymptotical linear behaviour at  
 257 strong stability (Zilitinkevich et al., 2008; Li, 2019). We therefore propose the following  
 258 expression of  $Pr$  that is plotted in Figure 1b:

$$Pr(Ri) = \begin{cases} Pr_n - \frac{2}{\pi}(Pr_\infty - Pr_n) \arctan\left(\frac{-Ri}{Ri_1}\right) & \text{if } Ri < 0 \\ Pr_n e^{\frac{1-\alpha_{Pr}}{Pr_n} Ri} + \alpha_{Pr} Ri & \text{if } Ri \geq 0 \end{cases} \quad (23)$$

The formulation in stable conditions is inspired from Venayagamoorthy and Stretch  
 (2010) and it shows fair agreement with experimental data (Li, 2019).  $\alpha_{Pr}$  is the slope of  
 the asymptotical linear trend at high stability and its value ranges from 3 to 5 (Grisogono,  
 2010).  $Pr_n$  is the neutral value of Prandtl number which from extensive laboratory and field

experiments as well as theoretical works range from 0.7 to 1 (Grisogono, 2010; Li, 2019). The continuity in slope at  $Ri = 0$  gives

$$Ri_1 = \frac{2}{\pi}(Pr_\infty - Pr_n) \quad (24)$$

259  $Pr_\infty$  is the value of  $Pr$  in the convective limit and its value roughly ranges between 0.3 and  
260 0.5 (Li, 2019).

## 261 **2.4 Vertical turbulent mixing length formulation**

In near-neutral conditions, we choose a turbulent vertical length-scale formulation  $l_n$  similar to Blackadar (1962) in which the displacement of eddies is limited by the distance to the ground in the neutral limit:

$$l_n = \frac{\kappa z l_\infty}{\kappa z + l_\infty} \quad (25)$$

262 where  $\kappa$  is the Von Kármán constant.  $l_\infty$  is the mixing-length far above the ground whose  
263 value in near-neutral conditions is generally estimated between 15 and 75 m (Sun, 2011;  
264 Lenderink & Holtslag, 2004) In stable conditions, the vertical displacement of eddies -  
265 whose size is roughly above the so-called Ozmidov scale - is limited by the stratification of  
266 the flow (e.g. van de Wiel et al. (2008)). André et al. (1978) and Deardoff (1980) introduced  
267 a widely used buoyancy length-scale which depends on the flow stratification characterised  
268 by Brunt-Väisälä pulsation  $N$ . The mixing length in stable conditions  $l_s$  then read :

$$l_s = c_l \frac{\sqrt{e}}{N} \quad (26)$$

269  $c_l$  being a scalar whose value varies between 0.1 and 2 (Deardoff, 1980; Nieuwtsadt,  
270 1984; Grisogono & Belušić, 2008; Baas et al., 2018).

271 More recent studies introduced wind-shear dependent formulation of  $l_s$  to account  
272 for the deformation of eddies - whose size is above a so-called Corrsin scale - by vertical  
273 wind shear (e.g. Grisogono and Belušić (2008); Grisogono (2010); Rodier et al. (2017)).  
274 Grisogono and Belušić (2008) proposed a mixing-length formulation including both the  
275 effect of stratification and vertical wind shear  $S^2$  that reads:

$$l_s = c_l \frac{\sqrt{e}}{2\sqrt{S^2}(1 + \sqrt{Ri}/2)} \quad (27)$$

The final mixing-length  $l$ , being either ground-limited or stratification-limited is the minimum between  $l_n$  and  $l_s$ . In the model implementation, we choose a commonly-used continuous interpolation formulation:

$$l = \left( \frac{1}{l_n^\delta} + \frac{1}{l_s^\delta} \right)^{-1/\delta} \quad (28)$$

276  $\delta = 1$  by default. The two expressions of  $l_s$  can be used independently in the param-  
277 eterization but unless otherwise stated, the results presented in the rest of the paper have  
278 been obtained with formulation dependent on both stratification and wind shear (Eq. 27).  
279 In practice,  $l$  is also lower bounded by a value  $l_{min} = 1$  cm to prevent it from reaching value  
280 below the Kolmogorov length scale in planetary atmospheric motions (Chen et al., 2016).  
281 As  $l_s$  depends on the TKE, in practice  $l$  is calculated with an explicit value of the TKE i.e.  
282 the value at the beginning of the time-step.

283

## 2.5 Surface layer scheme matching

284

285

286

Neglecting the vertical diffusion term of TKE  $\mathcal{T}$ , Eq. 7 in stationary conditions ( $\partial_t e = 0$ ) can be re-arranged to give a first-order turbulent closure like expressions of the eddy diffusion coefficients for momentum and heat (Cuxart et al., 2006):

$$K_m = l^2 \sqrt{S^2} F_m(Ri) \quad (29)$$

$$K_h = l^2 \sqrt{S^2} F_h(Ri) \quad (30)$$

where

$$F_m(Ri) = S_m^{3/2} \sqrt{c_\epsilon} \left(1 - \frac{Ri}{Pr}\right)^{1/2} \quad (31)$$

$$F_h(Ri) = S_m^{7/4} Pr^{-1} \sqrt{c_\epsilon} \left(1 - \frac{Ri}{Pr}\right)^{1/2} \quad (32)$$

are first-order like stability functions. Near the ground in the surface layer,  $l \approx \kappa z$  and England and McNider (1995) then show that  $F_{m,h}$  functions are identical to the stability functions involved in the bulk expressions of the surface drag coefficients used to calculate surface fluxes of momentum and heat in models :

$$C_{m,h} = \frac{\kappa^2}{\log(z/z_{0m}) \log(z/z_{0m,h})} F_{m,h} \quad (33)$$

287

288

289

290

291

with  $z_{0m}$  and  $z_{0h}$  the surface roughness lengths for momentum and heat respectively. Provided turbulence in the surface layer can be assumed to be close to a stationary state, using the same formulations for  $S_m$  and  $Pr$  in both the turbulent diffusion and surface layer schemes leads to a fully consistent formulation of turbulent fluxes from the surface layer up to the top of the boundary-layer.

292

## 2.6 Degrees of freedom of the scheme and adjustable parameters

293

294

295

296

297

298

299

300

Table 1 summarises all the 10 adjustable parameters of the new parameterization and their ranges of acceptable values as previously introduced in the text. The 8 first parameters in bold are those affecting the simulation of the neutral and stable boundary layers and taken into account in the tuning phase in the next section. It is worth mentioning that we also lower-bound the turbulent diffusion coefficients with the kinematic molecular viscosity and conductivity of the air, which are not tuning parameters per se but pressure and temperature dependent - thus planet dependent - quantities.

300

## 3 Implementation in General Circulation Models, evaluation and tuning

301

### 3.1 Implementation in the LMDZ GCM and Mars Planetary Climate Model

302

303

304

305

306

307

308

309

310

311

312

313

314

The ATKE parameterization has been implemented in the LMDZ Earth GCM (Hourdin et al., 2020; Cheruy et al., 2020), atmospheric component of the French IPSL Coupled-Model (Boucher et al., 2020) involved in the Coupled Model Intercomparison Project (CMIP) exercises. The turbulent-mixing parameterization of LMDZ has received a lot of attention in the past two decades, particularly regarding the convective boundary layer and the very stable boundary layer. It is a hybrid scheme in the sense that turbulent fluxes are expressed as a sum of a K-diffusion term - from the TKE-1 scheme of Yamada (1983) and revisited in Hourdin et al. (2002) and Vignon, Hourdin, et al. (2017) - and a non-local transport term by convective plumes (Rio et al., 2010; Hourdin et al., 2019). Despite those efforts, recent tests revealed that the latest version of the model - the CMIP6 version - still exhibits numerical instabilities in near-neutral boundary layers in presence of strong wind shear. As a proof of concept, the ATKE scheme has also been implemented in the Mars Planetary Climate Model (Mars PCM, Forget et al. (1999)). This model also uses a hybrid scheme

**Table 1.** Name, definition and range of acceptable values for the adjustable parameters. Parameters are dimensionless exception  $l_\infty$  which is a length in m. Parameters in bold are those which affect the simulation of the neutral and stable boundary layer.

Name	Definition	Range
$c_\epsilon$	controls the value of the dissipation length scale	[1.2 - 10]
$c_e$	controls the value of the diffusion coefficient of TKE	[1 - 5]
$l_\infty$	asymptotic mixing length far from the ground	[15 - 75]
$c_l$	controls the value of the mixing length in stratified conditions	[0.1 - 2]
<b><math>Ri_c</math></b>	critical Richardson number controlling the slope of $S_m$ in stable conditions	[0.19 - 0.25]
<b><math>S_{min}</math></b>	minimum value of $S_m$ in very stable conditions	[0.025 - 0.1]
<b><math>Pr_n</math></b>	neutral value of the Prandtl number	[0.7 - 1]
$\alpha_{Pr}$	linear slope of $Pr$ with $Ri$ in the very stable regime	[3 - 5]
$r_\infty$	ratio between $c_\infty$ and $c_n$ controlling the convective limit of $S_m$	[1.2 - 5.0]
$Pr_\infty$	value of $Pr$ in the convective limit	[0.3 - 0.5]

315 with a TKE-1 diffusion scheme inspired from Yamada (1983) and a dry parameterization of  
 316 convective plumes (Colaïtis et al., 2013). Colaïtis et al. (2013) have pointed out that the  
 317 default TKE-1 scheme of Hourdin et al. (2002) leads to numerical oscillations in strongly  
 318 stratified Martian nighttime conditions. They addressed this issue by imposing a mini-  
 319 mum mixing coefficient  $K_{min}$  whose value depends on the boundary layer height following  
 320 Holtslag and Boville (1993).

## 321 **3.2 Parametric sensitivity of the ATKE scheme and tuning**

### 322 **3.2.1 Initial test on the GABLS1 case and parametric sensitivity**

323 The ATKE scheme is first tested on single column simulations using the 1D version of  
 324 LMDZ with a 95-level vertical grid introduced in Hourdin et al. (2019). We run 1D simu-  
 325 lations on the GEWEX Atmospheric Boundary Layer Study 1 (GABLS1) single column model  
 326 intercomparison exercise. The latter consists in a no-radiation idealized 9 hour simulation of  
 327 the development of a weakly stable boundary layer, with a constant zonal geostrophic wind  
 328 of  $8 \text{ m s}^{-1}$  and a constant surface cooling of  $-0.25 \text{ K h}^{-1}$  (Cuxart et al., 2006). The fair  
 329 convergence of 3D LES on this case - with the exact same initial and boundary conditions as  
 330 those for single column models - make LES suitable references for GABLS1. Nonetheless, to  
 331 sample the small variability between LES runs, we consider hereafter 5 reference LES which  
 332 correspond to the MO-1m, MO-2m, UIB-2m, IMUK-1m, IMUK-2m simulations listed in  
 333 Table 2 of Beare et al. (2006), the suffix referring to the vertical resolution.

334 Given the ranges of acceptable values associated with each of the  $n = 8$  free param-  
 335 eters affecting the simulation of the stable boundary layer listed in Table 1, we need to  
 336 run simulations with different sets of parameters to assess the parametric sensitivity of the  
 337 scheme. For this purpose, we use the HighTune explorer statistical tool originally developed  
 338 in the Uncertainty Quantification community and now applicable in atmospheric modeling  
 339 (Couvreur et al., 2021). This tool allows to make a first perturbed physics ensemble exper-  
 340 iment through an exploration of the initial  $n$ -dimension hypercube of parameters defined  
 341 by the intervals given in Table 1 using a Latin Hyper Cube sampling method. Here 80  
 342 (10 times  $n$ ) sets of parameters or free parameters' vectors are sampled. Unless otherwise  
 343 stated, the simulations are run with a 15 min time step, i.e. the typical value used for the  
 344 LMDZ physics and that used for the ensemble of CMIP6 simulations.

345 Figure 2 shows the results of this *a priori* sensitivity analysis to free parameters' values  
 346 for the vertical profiles of potential temperature, wind speed and TKE averaged over the

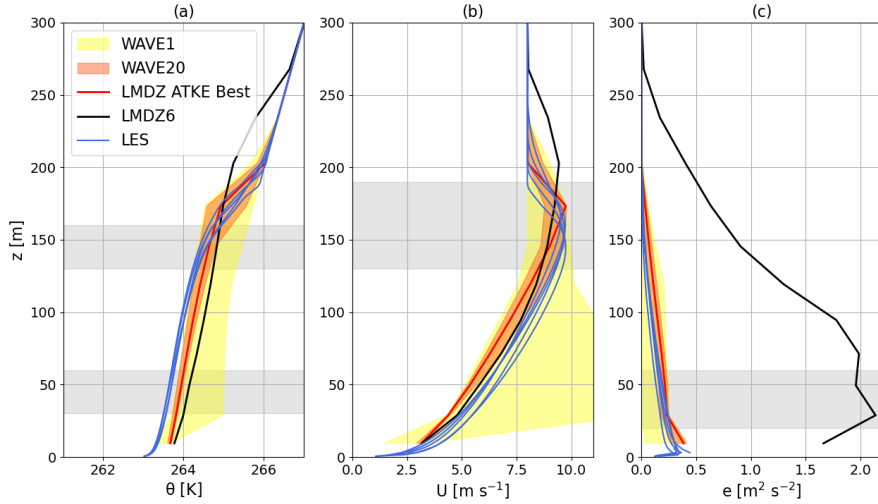


**Figure 2.** Evolution of envelopes of the vertical profiles of potential temperature (panel a), wind speed (panel b) and TKE (panel c) after 9 hours of GABLS1 simulation. Yellow and orange envelopes correspond to waves 1 and 20 respectively i.e. to the 1st and 20th set of 80 simulations during the tuning exercise. Blue curves show the 5 reference LES. The red curve shows the ‘best’ LMDZ simulation. The black curve shows the CMIP6 version of LMDZ for comparison. The horizontal light grey band show the vertical ranges over which the metrics are calculated for each variable. In panel c, note that the full (resolved+subgrid) TKE from the LES is shown.

347 eighth hour of the simulation. The yellow envelope displays the variability (minimum and  
 348 maximum values) amongst the 80 simulations from this first so-called ‘wave’ of simulations.  
 349 Albeit encompassing the five reference LES coming from the GABLS1 LES intercomparison  
 350 exercise (Beare et al., 2006), this yellow envelope highlights the large range of vertical  
 351 profiles obtained. This is a signature of the high sensitivity of the results to the parameters as  
 352 they are varied across the range given in Table 1. In particular, very strong and unrealistic  
 353 momentum decoupling manifesting as very strong wind speed gradient near the surface is  
 354 allowed by the scheme in regions of the parameter space where the negative feedback of  
 355 the wind shear on the mixing length (Eq. 27) is overappreciated. Interestingly, Figure 3b  
 356 shows that such a decoupling is never simulated when using the buoyancy-only dependent  
 357 length scale (Eq. 26). However, even if the yellow envelop is reasonable for the potential  
 358 temperature and wind speed (Figure 3a,b), the use of the buoyancy-only dependent length  
 359 scale can lead to unrealistically strong values of TKE in the middle of the boundary layer  
 360 (Figure 3c) owing to overly high mixing length values.

361 Overall, the large width of the yellow envelope in Figure 2 and the possible large discrep-  
 362 ancy with respect to the LES call for a reduction of the parameter space and a calibration  
 363 of the ATKE scheme.  
 364

### 365 **3.2.2 History matching with iterative refocusing**

366 For this purpose, we follow a history matching with iterative refocusing procedure  
 367 which in practice is performed with HighTune explorer. This procedure is made of 6 steps  
 368 and is fully described in Couvreur et al. (2021) and Hourdin et al. (2021). We refer the

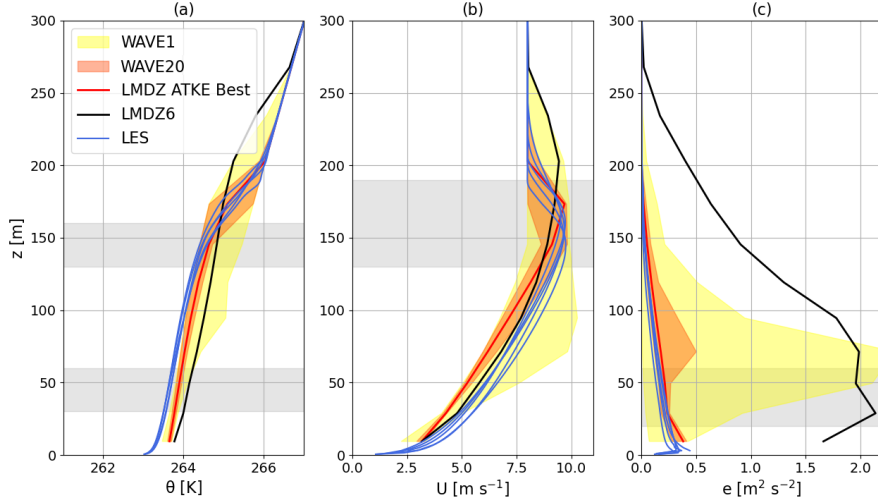


**Figure 3.** Same as Figure 2 but for simulations using the buoyancy length-scale formulation (Eq. 26) instead of the stratification and wind-shear dependent formulation (Eq. 27) in stable conditions.

369 reader to the aforementioned papers for details on the method and describe here the main  
 370 steps for our application.

371 *Step 1* We first define 5 metrics, i.e. targets for the model with respect to the LES  
 372 reference, to properly capture the boundary layer structure. Those metrics are the potential  
 373 temperature at the bottom (average between 30 and 60 m) and top (average between 130  
 374 and 160 m) part of the boundary layer, the zonal wind speed at the low-level jet height  
 375 (average between 130 and 190 m) and the TKE at the bottom (average between 20 and 60  
 376 m) and middle (average between 60 and 100 m) part of the boundary layer. All metrics are  
 377 calculated on hourly-mean profiles between the 8th and 9th hour of the simulation, when  
 378 the stable boundary layer is well developed.

379 *Step 2* We then define the initial parameter space consisting in a 8-dimension space  
 380 corresponding to the 8 parameters in bold in Figure 1 and their associated range of possible  
 381 values.

382 *Step 3* This parameter space is then sampled 80 times and experimented on GABLS1  
 383 simulation as in Sect. 3.2.1.

384 *Step 4* Based on those 80 simulations, an emulator is built for each metric based on  
 385 a Gaussian Process providing values for the expectation and variance at any location in the  
 386 parameter space.

*Step 5* We then compare the simulated metrics with respect to those from the LES  
 reference through the calculation of an implausibility  $I$  for each metrics at each point  $\lambda$  of  
 the parameter space:

$$I(\lambda) = \frac{|r - E[e_m(\lambda)]|}{\sqrt{\sigma_r^2 + \sigma_d^2 + \text{Var}(e_m(\lambda))}} \quad (34)$$

387 where the numerator is the absolute difference between the reference metrics  $r$  and the  
 388 corresponding expectation from the emulator  $E[e_m(\lambda)]$ ; and the denominator is the stan-  
 389 dard deviation of this difference, which includes the reference uncertainty (i.e. the spread

390 between LES  $\sigma_r^2$ ), the uncertainty associated to the emulator ( $Var(e_m(\lambda))$ ), and model struc-  
 391 tural uncertainty ( $\sigma_d^2$ , see Couvreur et al. (2021) for details). As the latter is not a priori  
 392 known, one has to prescribe an arbitrary ‘tolerance to error’ (see thorough discussion on the  
 393 rationale behind this tolerance in Hourdin et al. (2021)) that we set to 0.25 K for potential  
 394 temperature,  $0.25 \text{ m s}^{-1}$  for wind speed and  $0.01 \text{ m}^2 \text{ s}^{-2}$  for TKE. History matching then  
 395 rules out a part of the parameter space that corresponds to unacceptable model behaviour  
 396 - i.e. with an implausibility higher than a given cut-off value of 3 - and keeps a not-ruled  
 397 out yet (NROY) space.

398 *Step 6* Iterative refocusing then consists in sampling 80 new free parameter vectors  
 399 in the NROY space and reiterates over several tuning ‘waves’ from step 4 to 6.

400 Note that this procedure is not an optimization method providing in the end a single  
 401 set of parameters, but a method ruling-out a non-plausible part of the initial parameter  
 402 space and giving the space of acceptable free parameters - given the chosen metrics and  
 403 tolerances - once it has converged.

404 The results after 20 waves of tuning are shown with orange envelopes for the potential  
 405 temperature, wind speed and TKE profiles in Figure 2. Compared to the initial and first  
 406 wave (yellow envelopes), one can first notice the convergence towards LES curves. Consider-  
 407 able improvement is obtained with respect to the CMIP6 version of LMDZ, with a shallower  
 408 and more realistic - compared to LES - boundary-layer height, a more peaked low-level jet  
 409 and lower and much closer-to-LES TKE values. Nonetheless, the potential temperature  
 410 (resp. wind speed) in the first tens of meters above the surface remains slightly overesti-  
 411 mated (resp. underestimated). Such biases can be reduced by adding metrics targeting the  
 412 lowermost part of the profiles and increasing the vertical resolution close to the surface (not  
 413 shown).  
 414

415 We now examine the 10 ‘best’ simulations obtained during the tuning exercise. The  
 416 adjective ‘best’ is employed here as in Hourdin et al. (2021) in the sense that the maximum  
 417 (across metrics) value of the ratio of the distance to LES divided by the tolerance to error  
 418 is the smallest at the end of the tuning exercise. Note that this choice of 10 simulations and  
 419 the denomination ‘best’ goes beyond the history matching philosophy as there is *a priori*  
 420 no reason to prefer specific configurations than others in the final NROY spaces given the  
 421 chosen metrics and tolerances. A choice is done here to illustrate the behaviour of the ATKE  
 422 scheme for single sets of parameters obtained at the end of the tuning process in 1D and  
 423 3D simulations.

424 Figure 4a,c) show that they reproduce fairly well the profiles of heat and momentum  
 425 turbulent fluxes, i.e. two quantities that were not directly targeted during the tuning.  $K_{m,h}$   
 426 values are also much lower than those in the CMIP6 physics simulation (Figure 4b,d) which  
 427 concurs with conclusions regarding the profiles of TKE in Figure 2c. In addition, Figure  
 428 5 reveals the good numerical stability and convergence properties of the TKE in these  
 429 simulations, as well as the considerable improvement regarding these aspects with respect  
 430 to the CMIP6 version of the LMDZ physics. This makes us confident with the robustness and  
 431 efficiency and the numerical resolution method for the TKE evolution equation presented  
 432 in 2.2.2.

433 When inspecting more deeply the NROY space after 20 waves of tuning (Figure 6),  
 434 one can notice that its final shape has been mostly constrained by the  $c_l$  and  $c_\epsilon$ , and to a  
 435 lesser extent by  $l_\infty$ . This does not absolutely mean that the other 5 parameters do not play  
 436 role in the overall behaviour of the scheme but this shows that the representation of the  
 437 GABLS1 weakly stable boundary layer with ATKE mostly depends upon the value of  $c_l$ ,  $c_\epsilon$   
 438 and  $l_\infty$ . This point is further shown by the strong similarity between Figure 7 - which has  
 439 been produced with a tuning on  $c_l$ ,  $c_\epsilon$  and  $l_\infty$  only - and Figure 2. Such a result is not that  
 440 surprising since the turbulent diffusion in weakly stable boundary layer mostly results from

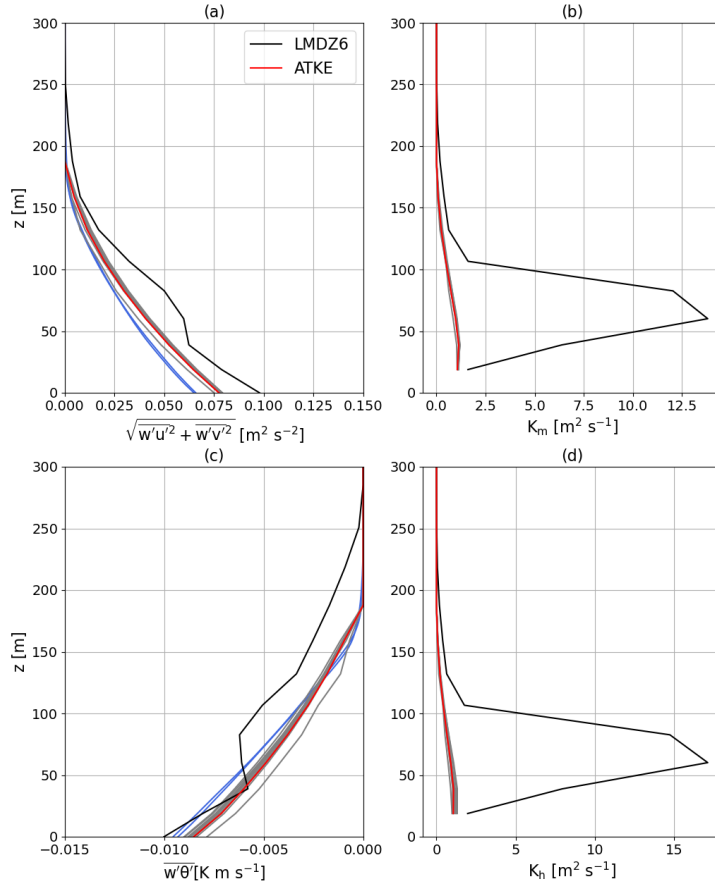


**Figure 4.** Vertical profiles of momentum flux (panel a), heat flux (panel c), eddy diffusivity coefficient for momentum (panel b) and heat (panel d) after 9 hours of GABLS1 simulation. Grey curves show the LMDZ simulations run with the 10 best parameter vectors after the tuning exercise. Blue curves in panels a and c show the 5 reference LES. The red curve shows the ‘best’ LMDZ simulation obtained during the tuning exercise (see main text for details). The black curve shows the CMIP6 version of LMDZ for comparison.

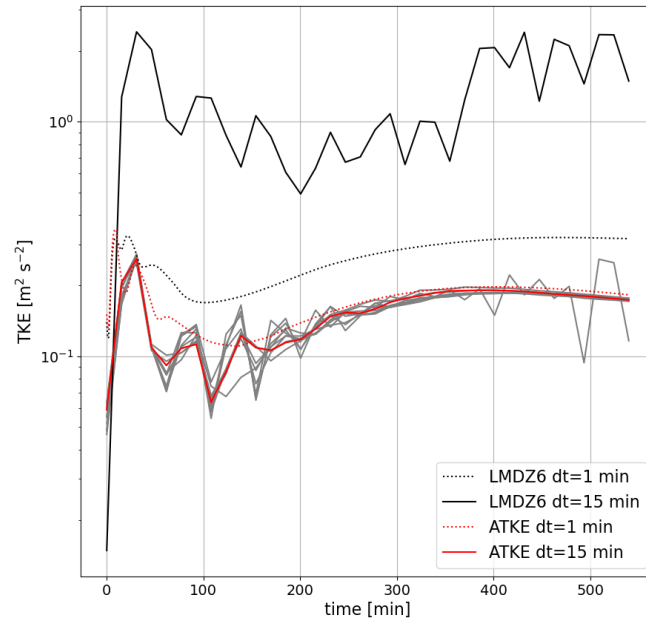


**Figure 5.** Time evolution of the TKE at 40 m a.g.l. in LMDZ single column model GABLS1 simulations. Solid grey curves show the simulations run with the 10 best parameter vectors after the tuning exercise and a 15 min time step. The solid and dotted red curves shows simulations run with the best parameter vector and a time step of 15 and 1 min respectively. The solid and dotted black curves shows simulations run with CMIP6 version of LMDZ and a time step of 15 and 1 min respectively.

441 eddies whose size and energy are controlled by wind shear intensity and TKE dissipation.  
 442 In addition, the weak dependence upon  $c_e$  may have somewhat been expected given the  
 443 relatively weak contribution of the transport term  $\mathcal{T}$  is the overall TKE budget (not shown).  
 444 Regarding  $S_{min}$ ,  $Ri_c$  and  $\alpha_{Pr}$ , one may expect a more important role of those parameters in  
 445 very stable boundary layers i.e. with a stratification more pronounced compared to that in  
 446 GABLS1. Their values might thus be more constrained if we were to tune the ATKE scheme  
 447 over a more stable boundary layer case such as GABLS4 (Couvreur et al., 2020) instead  
 448 of or in addition to GABLS1. However LES do not converge that well on GABLS4 which  
 449 makes the tuning exercise more delicate. Moreover, the role of radiation in determining  
 450 the structure of the boundary-layer becomes increasingly important as stability increases  
 451 (Edwards, 2009) and in addition to turbulent diffusion, the coupling between turbulence  
 452 and radiation becomes an essential feature to capture with models. We therefore leave this  
 453 aspect for further research.

### 454 3.3 Challenging the Antarctic and Martian stable boundary layers

455 We now conduct two short and arbitrary applications of the ATKE parameterization  
 456 in simulations with the LMDZ GCM and Mars PCM.

#### 457 3.3.1 Stable boundary layer regimes at Dome C, Antarctic Plateau

458 First, we verify that the proposed scheme is able to reproduce the dichotomous be-  
 459 haviour of the stable boundary layer at Dome C on the Antarctic Plateau that is, a very  
 460 stable regime with strong temperature surface-based inversions and collapsed turbulence  
 461 versus a weakly stable state with weak inversions. The sharp transition between those 2  
 462 regimes occurs in a narrow range of wind speed (Vignon, van de Wiel, et al., 2017; Baas  
 463 et al., 2019). Such a test was proposed in Vignon et al. (2018) to verify the ability of the  
 464 CMIP6 version of LMDZ to reproduce the overall dynamics of the stable boundary layers  
 465 and it is performed here as capturing the Dome C boundary layer was identified as a *target*  
 466 during the development of LMDZ for CMIP6 (Cheruy et al., 2020). This is an aspect that  
 467 we want to conserve throughout the development of the LMDZ physics and particularly  
 468 when introducing a new turbulent diffusion scheme. It is also worth noting that such a test  
 469 was also used for the recent development of the CanAM model (He et al., 2019) as well  
 470 as for verifying the robustness of LES of the stable boundary layer (van der Linden et al.,  
 471 2019). We follow here the exact same LMDZ simulation configuration as in Vignon et al.  
 472 (2018) that is, one year (2015) simulations are conducted with the zooming capability of  
 473 the LMDZ to refine a  $64 \times 64$  global grid to reach a  $50 \times 50$  km on the Dome C. One slight  
 474 difference though with respect to Vignon et al. (2018) is that we use the 95-level vertical grid  
 475 used in the previous section instead of the 79-level grid in the reference paper. Nudging in  
 476 wind, temperature and humidity towards ERA5 reanalyses (Hersbach et al., 2020) is applied  
 477 outside the zoom area to evaluate the sub-components of the physics of the model apart  
 478 from likely deficiencies in representing the large scale meteorological fields. The reader is  
 479 referred to Vignon et al. (2018) for details on the simulation configuration as well as the  
 480 surface snow treatment in LMDZ. The simulation has been run with the CMIP6 version of  
 481 the LMDZ physics as well as by an adapted versions using the ATKE diffusion scheme and  
 482 the 10 ‘best’ sets of parameters found from the single column model tuning.

483 A simple diagnostics to assess the representation of the two stable boundary layer  
 484 regimes is to investigate the dependence of the surface-based temperature inversion upon  
 485 the wind speed in clear sky conditions. Data align along a well-defined ‘inverted-S’ shape  
 486 curve (Vignon, van de Wiel, et al., 2017; van de Wiel et al., 2017), the two horizontal  
 487 branches corresponding to the two regimes and the vertical one to the non-linear transition  
 488 between them as the wind speed increases or decreases (Figure 8a). As shown in Figure 8b,  
 489 the CMIP6 version of LMDZ reasonably captures the strong surface-atmosphere decoupling  
 490 in very stable conditions and the 2-regime behaviour. LMDZ with the ATKE scheme run  
 491 with the ‘best’ set of parameters (Figure 8c) retained in Sect. 3.2 reproduces even more

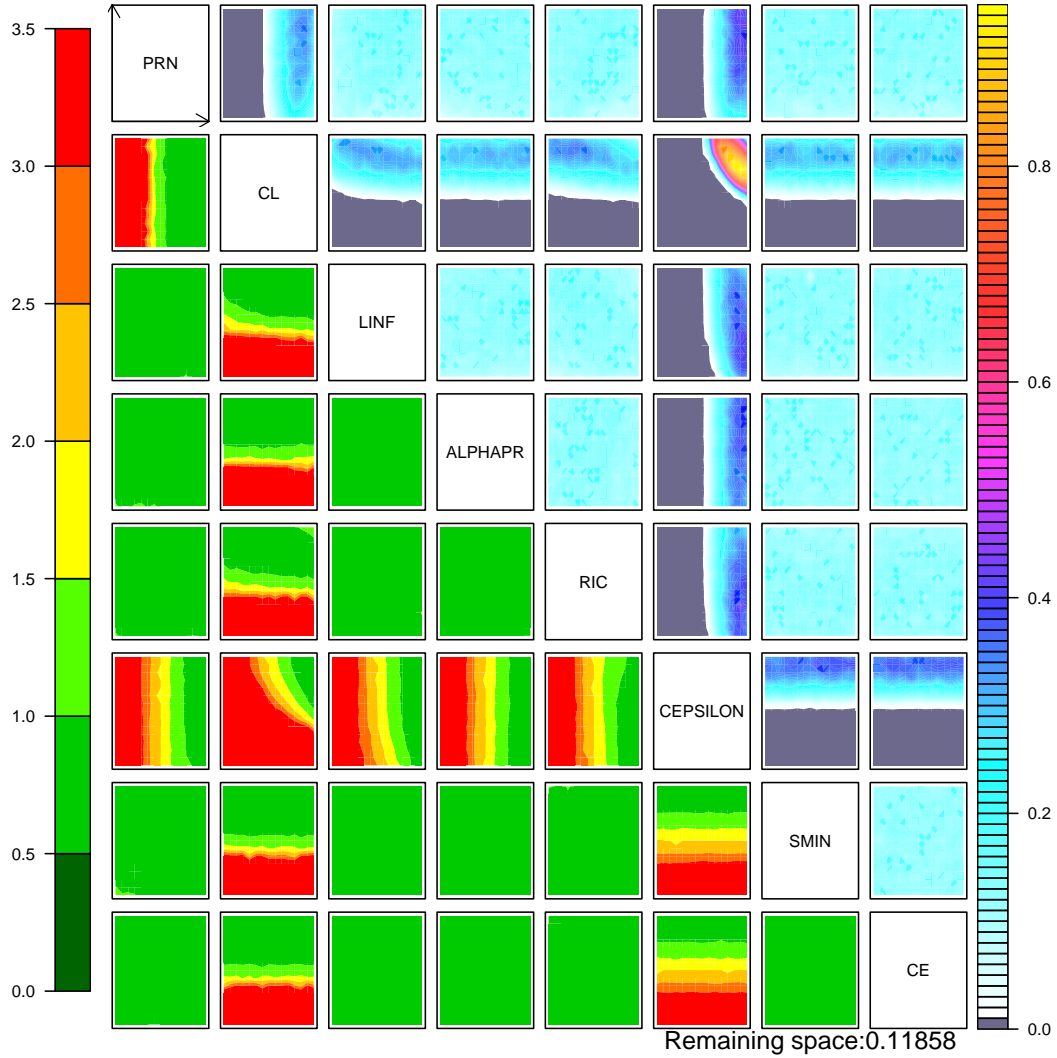


**Figure 6.** Implausibility matrix after 20 waves of history matching exploration. The upper-right triangle is made of sub-matrices that show the fraction of points with implausibility lower than the chosen cutoff while the sub-matrices of the lower-left triangle show the minimum value of the implausibility when all the parameters are varied except those used as x- and y-axis, the name of which are given on the diagonal of the main matrix. The number at the bottom of the graph shows the NROY space value (fraction of the initial parameter space) after 20 waves.

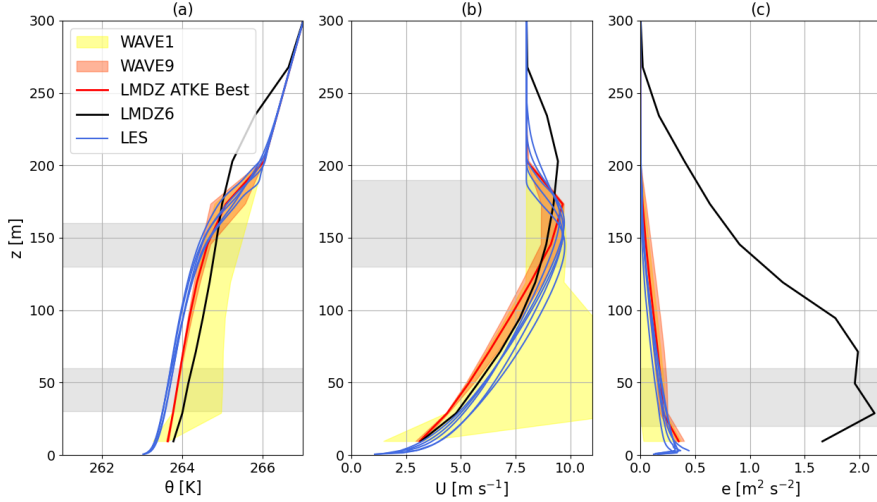


**Figure 7.** Same as Figure 2 but after a tuning on  $c_e$ ,  $c_l$  and  $l_\infty$  only. The other parameters have been arbitrarily set to the following values:  $Ri_c = 0.2$ ,  $S_{min} = 0.05$ ,  $Pr_n = 0.8$ ,  $\alpha_{Pr} = 4.5$  and  $c_e = 2.0$ . Note that we have stopped the tuning exercise at the 9th wave here since convergence has been attained.

492 realistically reproduce the 2-regime behaviour - that is, the reversed ‘S’ shape pattern - and  
 493 the decoupling in very stable conditions despite an overestimation of the strong temperature  
 494 inversions. The latter can be attributed to an overly weak downward longwave radiative  
 495 flux from the very dry and cold Dome C atmosphere in clear-sky conditions (Vignon et al.,  
 496 2018).

497 An important point here is that such results are obtained with all the 10 ‘best’ sets  
 498 of parameters after 20 waves of tuning on GABLS1 (Figures 8c-l) and despite the fact that  
 499 such a GABLS1-based tuning has not substantially constrained parameters that may be *a*  
 500 *priori* important in very stable conditions such as  $S_{min}$ ,  $Ri_c$  and  $\alpha_{Pr}$ . In fact, the transition  
 501 between the weakly and very stable regimes of the stable boundary-layer primarily relies on  
 502 the ability of a TKE-l scheme to allow for a turbulence collapse in very stable conditions  
 503 (Vignon et al., 2018). This is the case with the ATKE scheme - whatever the  $S_{min}$ ,  $Ri_c$   
 504 and  $\alpha_{Pr}$  value chosen in their corresponding ranges of acceptable values - as no artificial  
 505 threshold or lower-bound has been prescribed to maintain a certain amount of TKE in very  
 506 stable conditions.

### 507 3.3.2 Nocturnal stable boundary layer collapse on Mars

508 Mars has a thinner and much less dense atmosphere compared to Earth and its plan-  
 509 etary boundary layer exhibits stronger diurnal variations (Spiga et al., 2010b; Petrosyan et  
 510 al., 2011) with a abrupt collapse at the day-night transition. During night-time, the Mar-  
 511 tian boundary layer exhibits numerous similarities with that of the polar regions on Earth  
 512 such as strong surface-based temperature inversions associated with very weak turbulence  
 513 (Banfield et al., 2020), the latter being able to re-activate through wind shear production  
 514 associated with low-level jets (Chatain et al., 2021).

515 This extreme environment enables us to challenge the versatility of ATKE param-  
 516 eterization and compare its performance with the default TKE-l scheme used in the current  
 517 Mars PCM (Colaïtis et al., 2013).

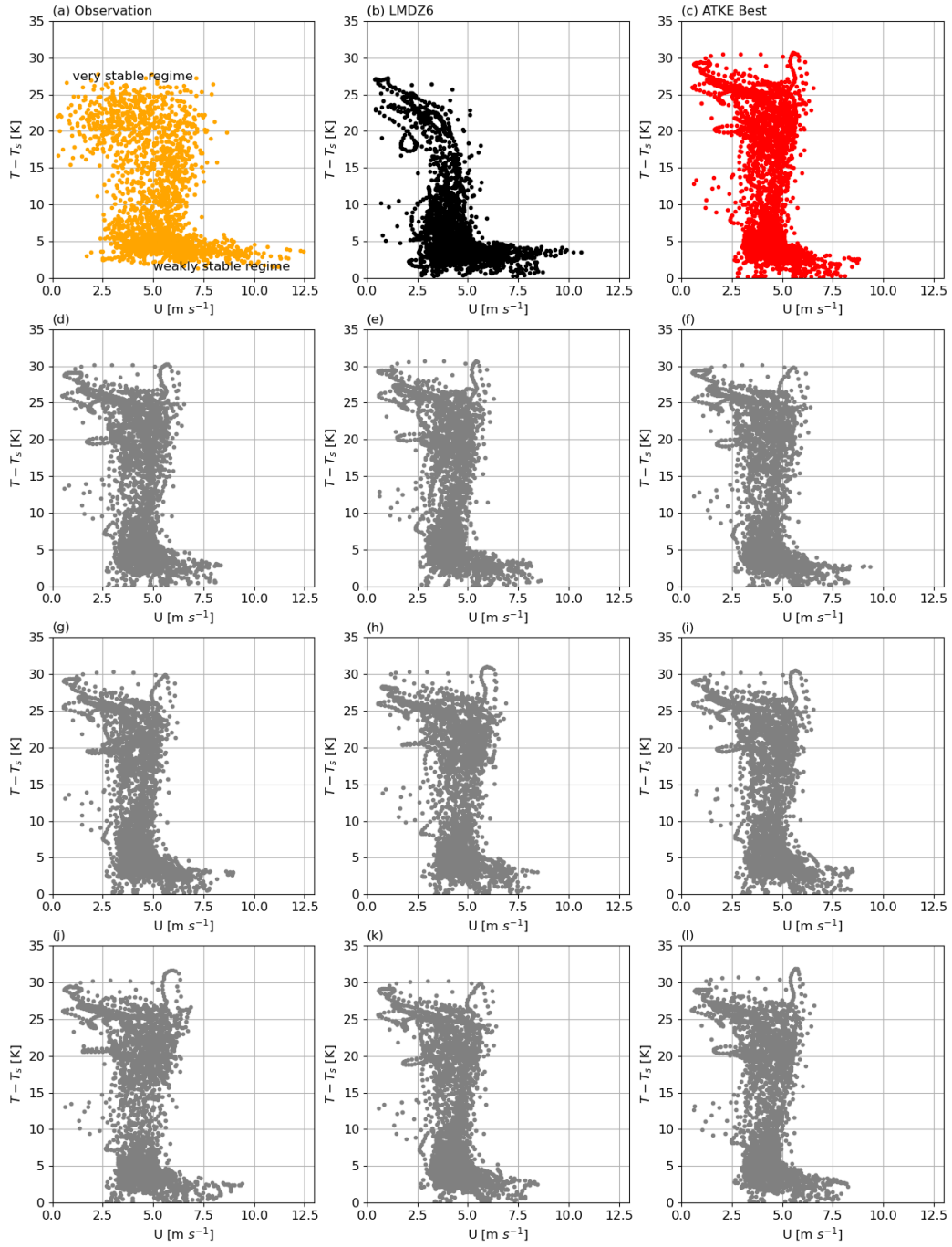


**Figure 8.** Temperature inversion between 10 m and the ground surface plotted as a function of the 10-m wind speed in clear-sky conditions (downward longwave radiative flux  $< 100 \text{ W m}^{-2}$ ) from April to September 2015. Panel a shows results from in situ observations. Panel b (resp. c) show the LMDZ simulation in the CMIP6 physics configuration (resp. with the ATKE scheme using the best set of parameters retained in Sect. 3.2). Panels d to l show results from 9 simulations with the ATKE scheme using 9 following ‘best’ sets of parameters after the tuning phase on GABLS1. Dome C measurement data are from Genthon et al. (2021).

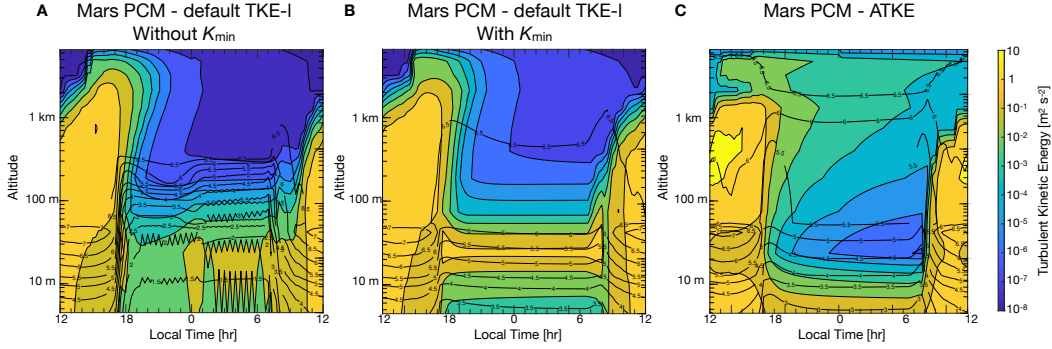


**Figure 9.** Evolution of the TKE through the Martian day in a) the baseline physics configuration; b) the same configuration with no minimum mixing coefficient  $K_{min}$ ; c) the simulation using the ATKE scheme for turbulent diffusion. Black contours indicate the wind speed in  $\text{m s}^{-1}$ .

518 As a first test, we compare the two parameterizations using the single-column version  
 519 of the Mars PCM to assess the overall behaviour of the diurnal cycle of the boundary  
 520 layer and the numerical stability of the model. The single-column version of the Mars  
 521 PCM uses the same physics as the 3D model (Lange et al., 2023) and a vertical grid with  
 522 6 levels in the first km above the ground. No lateral advection of heat and momentum  
 523 is prescribed, the initial temperature profile is set to 180 K and the zonal wind speed  
 524 is nudged towards a constant value of  $7 \text{ m s}^{-1}$  which corresponds to values measured at the  
 525 Mars Equator by the InSight lander (Banfield et al., 2020). Simulations are performed at  
 526 the Equator, with no dust aerosols, and ran for several Martian days until the diurnal cycle  
 527 reaches an equilibrium after 10 days. The nocturnal boundary layer simulated is weakly  
 528 to moderately stable, with a near-surface gradient Richardson not exceeding 0.1. Figure  
 529 9 shows the evolution of the TKE (colour shading) and wind speed (contours) in the first  
 530 km above the ground surface during a typical diurnal cycle. As explained in Sect. 3.1, the  
 531 nocturnal TKE field simulated by the default TKE-I scheme of the Mars PCM is affected  
 532 by strong numerical oscillations (Figure 9a) which are mitigated when adding a minimum  
 533 mixing coefficient  $K_{min}$  (Figure 9b). When using the ATKE scheme with the ‘best’ set of  
 534 parameters retained from the tuning on GABLS1 in Sect. 3.2.2 (Figure 9c) and with no  
 535 prescription of  $K_{min}$ , the structure of the nocturnal boundary layer is well captured and no  
 536 numerical oscillations affect the TKE and wind fields. Unlike in Figure 9b, the TKE exhibits  
 537 a continuous decrease with increasing height in the nocturnal boundary layer, which better  
 538 concurs with the typical TKE structure in weakly stable boundary layers (e.g., (Acevedo et  
 539 al., 2015)).

540 We then assess the performance of the ATKE model by performing simulations with  
 541 the 3D Mars PCM and comparing the results to in situ wind observations collected by the  
 542 InSight lander deployed at a latitude  $4.5^\circ \text{ N}$  and a longitude of  $135^\circ \text{ E}$ . InSight continuously  
 543 monitored the wind at a height of 1.2 m for almost one martian year with an unprecedented  
 544 time resolution (Banfield et al., 2020). Two striking phenomena have been detected. First,  
 545 a dramatic reduction of the wind speed, following the collapse of the boundary layer is  
 546 observed around 17-18 local time during the clear season (Figure 10a) i.e., the first half  
 547 of the Martian year when a relatively small amount of dust is present in the Martian sky  
 548 (Kahre et al., 2017). The abruptness of this change is related to both the very low thermal  
 549 inertia of the Martian ground surface and the thinness of the Martian atmosphere. Second,  
 550 during the dusty season i.e. the second half of the Martian year, substantial night-time  
 551 turbulence is observed (Chatain et al., 2021) and the decrease in near-surface wind speed  
 552 is less pronounced (Figure 10d). Those two phenomena have been shown to be poorly

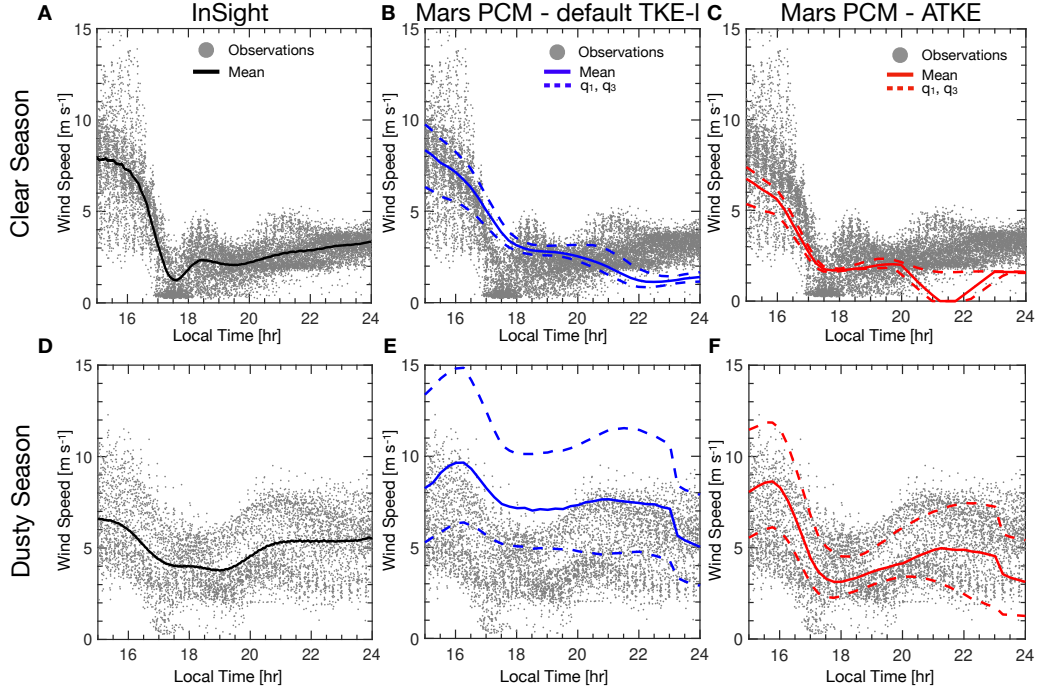


**Figure 10.** Comparison between InSight wind speed measurements (grey dots and black curves in panels a and d ) and Mars PCM simulations using the default TKE-l scheme (b, e) and the ATKE scheme (c, f). For model fields, the mean wind speed over the period considered is presented in solid lines, and the diurnal variability is shown with the envelope of dashed lines ( $q_1$  and  $q_3$  referring to the first and third quartiles).

553 reproduced by the Mars PCM, in particular, the collapse of winds at sunset (Forget et al.,  
554 2021).

555 Here, as a proof of concept, we run the 3D Mars PCM using either the default TKE-l  
556 scheme and the ATKE scheme with the ‘best’ set of parameters from the GABLS1 tuning i.e.  
557 with no specific tuning for Martian conditions. Global simulations are performed over one  
558 complete martian year with a resolution of  $3.75^\circ$  in latitude and  $135.9^\circ$  in longitude. Initial  
559 conditions are derived from 10-year simulations which provide equilibrium states of water  
560 and  $\text{CO}_2$  cycles (Pottier et al., 2017). The seasonal and geographic variations of dust opacity  
561 in the sky are prescribed using dust observations by (Montabone et al., 2015). Results are  
562 presented in Figure 10. Concurring with Forget et al. (2021), the model in its standard  
563 configuration fails to reproduce the sharp transition from high to low wind speeds at sunset  
564 (Figure 10b). This aspect is significantly improved when using the ATKE scheme (Figure  
565 10c). However, the wind speed in the second part of the night remains underestimated in  
566 both configurations which questions the representation of the surface-atmosphere decoupling  
567 in this period (Chatain et al., 2021). In the dusty season, the current model overestimates  
568 the surface wind speed owing to an excess of turbulent mixing (Figure 10e), while the ATKE  
569 parameterization leads to more realistic wind speeds (Figure 10f).

570 Overall, this preliminary experiment demonstrates: i) the applicability of the ATKE  
571 parameterization on Mars and the promising results that can be obtained with a set of  
572 parameters not specifically tuned for Mars conditions and; ii) the improvement of the model  
573 both numerically and physically in stable conditions. Nonetheless, Mars simulations with  
574 the ATKE scheme would further benefit from a more adapted tuning using references such as  
575 Mars LES (Spiga et al., 2010a) or InSight observations (Banfield et al., 2020). It is also worth

576 noting that the Mars atmosphere, particularly at the poles i.e. far from the InSight landing  
 577 site, exhibits particularities that cannot be properly captured with the current version of  
 578 the ATKE scheme. A key aspect is that air buoyancy can be created by compositional  
 579 vertical gradients of both water vapor and carbon dioxide, i.e. the prevailing gas of Mars'  
 580 atmosphere. In particular, during the winter polar night, CO<sub>2</sub> condenses upon the ice cap  
 581 surface (e.g., (Weiss & Ingersoll, 2000)) changing dramatically the near-surface atmospheric  
 582 composition. Such an effect cannot be taken into account given with Brünt-Vaisala pulsation  
 583 and Richardson number expressions based on a virtual potential temperature. This aspect  
 584 deserves attention for further improvement of the ATKE scheme.

## 585 4 Summary and Conclusions

586 This study presents the development of a simple TKE-l parameterization of turbulent  
 587 eddy coefficients for the simulation of the neutral and stable boundary layer in large-scale  
 588 atmospheric models. The parameterization has been carefully designed such that all ad-  
 589 justable parameters have been clearly identified and their ranges of possible values defined  
 590 to help the calibration and assess the parametric sensitivity. Instead of using fixed and  
 591 empirical expressions of stability functions and turbulent Prandtl number, we have derived  
 592 fully tunable and heuristic formulae to improve the versatility of the scheme and its potential  
 593 applicability for planetary atmospheres composed of an ideal and perfect gas. A wind-shear  
 594 and buoyancy dependent formulation for the mixing length in stratified conditions is con-  
 595 sidered. A 2-step numerical treatment of the TKE equation is further proposed and shows  
 596 good convergence and stability properties at typical time steps used in large scale atmo-  
 597 spheric models. The parametric sensitivity of the ATKE scheme has been assessed with  
 598 the HighTune explorer tools using 1D simulations of the GABLS1 weakly stable boundary  
 599 layer case with the single-column version of LMDZ. Using a History-Matching approach,  
 600 we carried out a first calibration of the scheme allowing us to reduce the initial parameter  
 601 space to keep an ensemble that satisfies the representation of weakly stable boundary layer.  
 602 Substantial improvement with respect to the CMIP6 version of LMDZ has been achieved in  
 603 terms of vertical profiles of temperature, wind, TKE and turbulent fluxes of momentum and  
 604 heat, as well as in terms of numerical stability. However this tuning experiment restricted  
 605 to the weakly stable GABLS1 case has not enabled us to clearly evidence a potential added  
 606 value of a wind-shear and buoyancy dependent formulation for the mixing length in strat-  
 607 ified conditions compared to a buoyancy only-dependent one, even if the vertical profile of  
 608 TKE is slightly better captured.

609 The ability of the ATKE scheme to simulate the stable boundary layer as well as its  
 610 applicability to planetary atmospheres have then been assessed through simulations of the  
 611 Antarctic and Martian boundary layer with the LMDZ and Mars Planetary Climate model  
 612 respectively. In particular the 2-regime behaviour of the stable boundary layer at Dome C,  
 613 a challenge for turbulent diffusion schemes in GCMs, is reasonably well captured with the  
 614 ATKE scheme. In addition, promising results have been obtained for the representation of  
 615 the nocturnal Martian boundary layer with improvements regarding the numerical stability  
 616 compared to the original model. Such results pave the way for a Mars-specific tuning of the  
 617 ATKE scheme in the future.

618 A prospect of our work is to verify the physical and numerical robustness of the  
 619 ATKE parameterization in atmospheric flows with extremely strong wind shear such as  
 620 katabatic winds developing over ice caps. Such an application could also make it possible to  
 621 assess a potential added value of a wind shear-dependent formulation of the mixing length.  
 622 Moreover, in view of a fully reliable application in a climate model such as LMDZ, the  
 623 key parameters of the ATKE scheme - especially  $c_l$  and  $c_e$  - should be included in a more  
 624 thorough tuning exercise including parameters from other parameterizations and considering  
 625 additional metrics on convective boundary layer simulations (Hourdin et al., 2021).

626 Last but not least, we would like to emphasize that this work was initiated and fos-  
 627 tered during collaborative work sessions dedicated to the transfer of knowledge and critical  
 628 questioning on the physics and assumptions behind the parameterizations used in planetary  
 629 GCMs. Those sessions spontaneously emerged following students' questions and gathered  
 630 atmospheric and planetary scientists experts and non experts of turbulent mixing and pa-  
 631 rameterization development. The motivations behind the ATKE scheme development went  
 632 beyond the need to advance the turbulent diffusion scheme in our models but were also - and  
 633 maybe firstly - a reason and a need to teach and learn the parameterization development in  
 634 a 'learning-by-doing' way.

## 635 **Appendix A A gravity-invariant formulation of our TKE-1 turbulent dif-** 636 **fusion scheme**

637 For the sake of universality of a turbulent diffusion parameterization and in particular  
 638 for potential application on different planets, one may want to develop a framework as in-  
 639 dependent as possible upon planet's characteristics, in particular upon planet's gravity. In  
 640 the main paper, gravity appears in the expression of the Brünt Väisälä frequency thus in  
 641 the expression of the gradient Richardson number and in the buoyancy term of the TKE  
 642 evolution equation Eq 7. In this appendix, we briefly introduce a framework using geopo-  
 643 tential as vertical coordinate and in which gravity is no longer involved. Such a framework  
 644 is proposed here as a prospect for a further new implementation of the parameterisation.

Let's introduce the geopotential  $\phi$  defined such that  $d\phi = g dz$  as well as a 're-scaled'  
 time  $\tau$  defined by  $d\tau = g dt$ . The diffusion equation of a quantity  $c$  (Eq. 5) can be written in  
 the form:

$$\frac{\partial c}{\partial \tau} = \frac{1}{\rho} \frac{\partial}{\partial \phi} \left( \rho K_c^\phi \frac{\partial c}{\partial \phi} \right) \quad (\text{A1})$$

645 where  $K_c^\phi = g K_c$ . In such a framework, assuming down-gradient expression of tur-  
 646 bulent fluxes and the same closures for the TKE dissipation and transport terms as in the  
 647 main manuscript, the TKE evolution equation A1 reads:

$$\frac{\partial e}{\partial \tau} = K_m^\phi [(S^\phi)^2 - Pr(Ri)(N^\phi)^2] + \frac{1}{\rho} \frac{\partial}{\partial \phi} (\rho c_e K_m^\phi \frac{\partial e}{\partial \phi}) - \frac{e^{3/2}}{c_\epsilon l^\phi} \quad (\text{A2})$$

648 with  $l^\phi = gl$ ,  $(S^\phi)^2 = (\partial_\phi u)^2 + (\partial_\phi v)^2$  and  $(N^\phi)^2 = \frac{1}{\theta_v} \frac{\partial \theta_v}{\partial \phi}$ .

One can then express  $K_m^\phi = l^\phi(\phi, e, Ri) S_m(Ri) \sqrt{e}$ . Noting the gravity independent  
 form of the gradient Richardson number  $Ri = (N^\phi)^2 / (S^\phi)^2$ , the expressions for  $S_m(Ri)$  and  
 $Pr(Ri)$  can be taken identically from Eq. 20 and 23 as they are gravity-independent. For  
 the mixing length  $l^\phi$  expression, one can use a similar approach as in Sect. 2.4 replacing  
 the neutral-limit formulation with

$$l_n^\phi = \frac{\kappa \phi l_\infty^\phi}{\kappa \phi + l_\infty^\phi} \quad (\text{A3})$$

649  $l_\infty^\phi$  being a tuning parameter. In such a way Eq. A1 and A2 combined with the  
 650 proposed expressions for  $K_m$ ,  $Pr$  and  $l^\phi$  establish a complete gravity-invariant formulation  
 651 of the turbulent diffusion parameterization.

## 652 **Open Research Section**

653 The latest version of the LMDZ source code can be downloaded freely from the LMDZ  
 654 web site. The version used for the specific simulation runs for this paper is the 'svn' re-  
 655 lease 4781 from 21 December 2023, which can be downloaded and installed on a Linux

656 computer by running the `install_lmdz.sh` script available here: [http://www.lmd.jussieu](http://www.lmd.jussieu.fr/~tilde/pub/install_lmdz.sh)  
 657 [.fr/~tilde/pub/install\\_lmdz.sh](http://www.lmd.jussieu.fr/~tilde/pub/install_lmdz.sh). The Mars PCM used in this work can be down-  
 658 loaded with documentation from the SVN repository at [https://svn.lmd.jussieu.fr/](https://svn.lmd.jussieu.fr/Planeto/trunk/LMDZ.MARS/)  
 659 [Planeto/trunk/LMDZ.MARS/](https://svn.lmd.jussieu.fr/Planeto/trunk/LMDZ.MARS/). Forcings for the GABLS1 single-column cases are provided  
 660 under the DEPHY-SCM standard at the following link: [https://github.com/GdR-DEPHY/](https://github.com/GdR-DEPHY/DEPHY-SCM/)  
 661 [DEPHY-SCM/](https://github.com/GdR-DEPHY/DEPHY-SCM/). GABLS1 LES used in the intercomparison exercise of Beare et al. (2006) are  
 662 distributed here: [https://gabls.metoffice.gov.uk/lem\\_data.html](https://gabls.metoffice.gov.uk/lem_data.html)  
 663 Dome C temperature and wind speed data are freely distributed on PANGAEA data repos-  
 664 itories at <https://doi.org/10.1594/PANGAEA.932512> and [https://doi.org/10.1594/](https://doi.org/10.1594/PANGAEA.932513)  
 665 [PANGAEA.932513](https://doi.org/10.1594/PANGAEA.932513). InSight wind data can be retrieved from the Planetary Data System  
 666 (Jose Rodriguez-Manfredi, 2019).

## 667 Acknowledgments

668 This project has received funding from the European Research Council (ERC) under the  
 669 European Union’s Horizon 2020 research and innovation programme (grant no. 951596)  
 670 through the AWACA project. The part of the work related to the Martian atmosphere is  
 671 supported by the ANR project MAGIS. We acknowledge support from the DEPHY research  
 672 group, funded by CNRS/INSU and Météo-France, as well as from the PEPR TRACCS  
 673 project (no. ANR-22-EXTR-0008) funded from the Agence Nationale de la Recherche -  
 674 France 2030. Éric Bazile is gratefully acknowledged for fruitful discussions. This study was  
 675 conducted using the ESPRI (Ensemble de Services Pour la Recherche l’IPSL) computing and  
 676 data center (<https://mesocentre.ipsl.fr>) which is supported by CNRS, Sorbonne Université,  
 677 Ecole Polytechnique, and CNES and through national and international grants. Simulations  
 678 were performed using HPC resources from the IDRIS (Institut du Développement et des  
 679 Ressources en Informatique Scientifique, CNRS, France), project RLMD AD010107632R1.  
 680 Simulations with the Mars PCM were performed using HPC resources of Centre Informa-  
 681 tique National de l’Enseignement Supérieur (CINES) under the allocation n°A0100110391  
 682 made by Grand Equipement National de Calcul Intensif (GENCI).

## 683 References

- 684 Acevedo, O. C., Mahrt, L., Puhales, F. S., Costa, F. D., Medeiros, L. E., & Degrazia, G. A.  
 685 (2015). Contrasting structures between the decoupled and coupled states of the stable  
 686 boundary layer. *Q J R Meteorol Soc*, *142*(695), 693-702. (doi: 10.1002/qj.2693)
- 687 André, J. C., Moor, G. D., Lacarrère, P., & du Vachat, R. (1978). Model-  
 688 ing the 24-hour evolution of the mean and turbulent structures of the plane-  
 689 tary boundary layer. *Journal of Atmospheric Sciences*, *35*(10), 1861 - 1883.  
 690 Retrieved from [https://journals.ametsoc.org/view/journals/atsc/35/10/1520-](https://journals.ametsoc.org/view/journals/atsc/35/10/1520-0469_1978_035_1861_mtheot_2_0_co_2.xml)  
 691 [-0469\\_1978\\_035\\_1861\\_mtheot\\_2\\_0\\_co\\_2.xml](https://journals.ametsoc.org/view/journals/atsc/35/10/1520-0469_1978_035_1861_mtheot_2_0_co_2.xml) doi: [https://doi.org/10.1175/1520-](https://doi.org/10.1175/1520-0469(1978)035(1861:MTHEOT)2.0.CO;2)  
 692 [-0469\(1978\)035\(1861:MTHEOT\)2.0.CO;2](https://doi.org/10.1175/1520-0469(1978)035(1861:MTHEOT)2.0.CO;2)
- 693 Audouin, O., Roehrig, R., Couvreur, F., & Williamson, D. (2021). Modeling the gabls4  
 694 strongly-stable boundary layer with a gcm turbulence parameterization: Parametric  
 695 sensitivity or intrinsic limits? *Journal of Advances in Modeling Earth Systems*, *13*(3),  
 696 e2020MS002269. doi: <https://doi.org/10.1029/2020MS002269>
- 697 Baas, P., Van De Wiel, B., Van der Linden, S., & Bosveld, F. (2018). From near-neutral to  
 698 strongly stratified: Adequately modelling the clear-sky nocturnal boundary layer at  
 699 cabauw. *Boundary-Layer Meteorology*, *166*, 217–238.
- 700 Baas, P., van de Wiel, B. J. H., van Meijgaard, E., Vignon, E., Genthon, C., van der  
 701 Linden, S. J. A., & de Roode, S. R. (2019). Transitions in the wintertime near-  
 702 surface temperature inversion at dome c, antarctica. *Quarterly Journal of the Royal*  
 703 *Meteorological Society*, *145*(720), 930-946. doi: <https://doi.org/10.1002/qj.3450>
- 704 Banfield, D., Spiga, A., Newman, C., Forget, F., Lemmon, M., Lorenz, R., . . . others (2020).  
 705 The atmosphere of mars as observed by insight. *Nature Geoscience*, *13*(3), 190–198.
- 706 Bazile, E., Marquet, P., Bouteloup, Y., & Bouysse, F. (2011). The turbulent kinetic energy

- (tke) scheme in the nwp models at météo-france. In *Workshop on diurnal cycles and the stable boundary layer, ecmwf* (pp. 127–136).
- 707  
708
- 709 Beare, R. J., Macvean, M. K., Holtslag, A. A. M., Cuxart, J., Esau, I., Golaz, J.-C.,  
710 ... Sullivan, P. (2006). An intercomparison of large-eddy simulations of the stable  
711 boundary layer. *Boundary-Layer Meteorology*, *118*(2), 247–272. doi: 10.1007/s10546-  
712 -004-2820-6
- 713 Betts, A. K. (1973). Non-precipitating cumulus convection and its parameteri-  
714 zation. *Quarterly Journal of the Royal Meteorological Society*, *99*(419), 178-  
715 196. Retrieved from [https://rmets.onlinelibrary.wiley.com/doi/abs/10.1002/](https://rmets.onlinelibrary.wiley.com/doi/abs/10.1002/qj.49709941915)  
716 [qj.49709941915](https://doi.org/10.1002/qj.49709941915) doi: <https://doi.org/10.1002/qj.49709941915>
- 717 Blackadar, A. K. (1962). The vertical distribution of wind and turbulent exchange in neutral  
718 atmosphere. *J Geophys Res*, *67*, 3095-3102.
- 719 Boucher, O., Servonnat, J., Albright, A. L., Aumont, O., Balkanski, Y., Bastrikov, V.,  
720 ... Vuichard, N. (2020). Presentation and evaluation of the ipsl-cm6a-lr climate  
721 model. *Journal of Advances in Modeling Earth Systems*, *12*(7), e2019MS002010. doi:  
722 10.1029/2019MS002010
- 723 Bougeault, P., & Lacarrère, P. (1989). Parametrization of orography-induced turbulence in  
724 a mesobeta-scale model. *Monthly-Weather Rev*, *117*, 1872-1891.
- 725 Chatain, A., Spiga, A., Banfield, D., Forget, F., & Murdoch, N. (2021). Sea-  
726 sonal variability of the daytime and nighttime atmospheric turbulence experi-  
727 enced by insight on mars. *Geophysical Research Letters*, *48*(22), e2021GL095453.  
728 Retrieved from [https://agupubs.onlinelibrary.wiley.com/doi/abs/10.1029/](https://agupubs.onlinelibrary.wiley.com/doi/abs/10.1029/2021GL095453)  
729 [2021GL095453](https://doi.org/10.1029/2021GL095453) doi: <https://doi.org/10.1029/2021GL095453>
- 730 Chen, W., Lovejoy, S., & Muller, J.-P. (2016). Mars’ atmosphere: The sister planet,  
731 our statistical twin. *Journal of Geophysical Research: Atmospheres*, *121*(20), 11,968-  
732 11,988. doi: <https://doi.org/10.1002/2016JD025211>
- 733 Cheruy, F., Ducharne, A., Hourdin, F., Musat, I., Vignon, , Gastineau, G., ... Zhao, Y.  
734 (2020). Improved near-surface continental climate in ipsl-cm6a-lr by combined evolu-  
735 tions of atmospheric and land surface physics. *Journal of Advances in Modeling Earth*  
736 *Systems*, *12*(10), e2019MS002005. doi: <https://doi.org/10.1029/2019MS002005>
- 737 Colàitis, A., Spiga, A., Hourdin, F., Rio, C., Forget, F., & Millour, E. (2013). A ther-  
738 mal plume model for the Martian convective boundary layer. *Journal of Geophysical*  
739 *Research: Planets*, *118*(7), 1468-1487. doi: 10.1002/jgre.20104
- 740 Couvreur, F., Bazile, E., Rodier, Q., Maronga, B., Matheou, G., Chinita, M. J., ... others  
741 (2020). Intercomparison of large-eddy simulations of the antarctic boundary layer  
742 for very stable stratification. *Boundary-Layer Meteorology*, *176*(3), 369–400. doi:  
743 10.1007/s10546-020-00539-4
- 744 Couvreur, F., Hourdin, F., Williamson, D., Roehrig, R., Volodina, V., Villefranche, N., ...  
745 Xu, W. (2021). Process-based climate model development harnessing machine learn-  
746 ing: I. a calibration tool for parameterization improvement. *Journal of Advances in*  
747 *Modeling Earth Systems*, *13*(3), e2020MS002217. Retrieved from [https://agupubs](https://agupubs.onlinelibrary.wiley.com/doi/abs/10.1029/2020MS002217)  
748 [.onlinelibrary.wiley.com/doi/abs/10.1029/2020MS002217](https://doi.org/10.1029/2020MS002217) doi: [https://doi](https://doi.org/10.1029/2020MS002217)  
749 [.org/10.1029/2020MS002217](https://doi.org/10.1029/2020MS002217)
- 750 Cuxart, J., Holtslag, A. A. M., Beare, R. J., Bazile, E., Beljaars, A., Cheng, A., ... Xu, K.-  
751 M. (2006). Single-column model intercomparison for a stably stratified atmospheric  
752 boundary layer. *Boundary-Layer Meteorol*, *118*(2), 273-303. (doi:10.1007/s10546-005-  
753 3780-1)
- 754 Deardoff, J. W. (1980). Stratocumulus-capped mixed layers derived from a threee dimen-  
755 sionnal model. *Boundary-Layer Meteorol*, *18*, 495-527.
- 756 Delage, Y. (1997). Parametrising sub-grid scale vertical transport in atmospheric models  
757 under statically stable conditions. *Boundary-Layer Meteorol*, *82*, 23-48.
- 758 Deleersnijder, E. (1992). *Modélisation hydrodynamique tridimensionnelle de la circulation*  
759 *générale estivale de la région du détroit de bering (in french)* (Unpublished doctoral  
760 dissertation). Université Catholique de Louvain.
- 761 Derbyshire, S. H. (1990). Nieuwstadt’s stable boundary layer revisited. *Q J R Meteorol*

- 762 *Soc*, 126, 127-158.
- 763 Dufresne, J.-L., & Ghattas, J. (2009). Description du schéma de la couche limite turbulente  
764 et l'interface avec la surface planétaire dans lmdz. *ORCHIDEE documentation*.  
765 Retrieved from [http://forge.ipsl.jussieu.fr/orchidee/attachment/wiki/](http://forge.ipsl.jussieu.fr/orchidee/attachment/wiki/Documentation/CouplingLMDZ/Dufresne,%20Ghattas%20-%202009-Coupling-ORC-LMDZ.pdf)  
766 [Documentation/CouplingLMDZ/Dufresne,%20Ghattas%20-%202009-Coupling](http://forge.ipsl.jussieu.fr/orchidee/attachment/wiki/Documentation/CouplingLMDZ/Dufresne,%20Ghattas%20-%202009-Coupling-ORC-LMDZ.pdf)  
767 [-ORC-LMDZ.pdf](http://forge.ipsl.jussieu.fr/orchidee/attachment/wiki/Documentation/CouplingLMDZ/Dufresne,%20Ghattas%20-%202009-Coupling-ORC-LMDZ.pdf) (in french)
- 768 Edwards, J. M. (2009). Radiative processes in the stable boundary layer: Part i. radiatives  
769 aspects. *Boundary-Layer Meteorology*, 131(1). doi: 10.1007/s10546-009-9364-8
- 770 Emanuel, K. A. (1991). A scheme for representing cumulus convection in large-scale models.  
771 *Journal of Atmospheric Sciences*, 48(21), 2313 - 2329. doi: [https://doi.org/10.1175/](https://doi.org/10.1175/1520-0469(1991)048(2313:ASFRCC)2.0.CO;2)  
772 [1520-0469\(1991\)048\(2313:ASFRCC\)2.0.CO;2](https://doi.org/10.1175/1520-0469(1991)048(2313:ASFRCC)2.0.CO;2)
- 773 England, D. E., & McNider, R. T. (1995). Stability functions based upon shear functions.  
774 *Boundary-Layer Meteorol*, 74, 113-130.
- 775 Forget, F., Banfield, D., Spiga, A., Millour, E., Borella, A., Lange, L., ... Banerdt, W. B.  
776 (2021). More than one Martian year of meteorology observed by the InSight Lander. In  
777 *European planetary science congress* (p. EPSC2021-273). doi: 10.5194/epsc2021-273
- 778 Forget, F., Hourdin, F., Fournier, R., Hourdin, C., Talagrand, O., Collins, M., ... Huot,  
779 J.-P. (1999). Improved general circulation models of the martian atmosphere from  
780 the surface to above 80 km. *Journal of Geophysical Research: Planets*, 104(E10),  
781 24155-24175. Retrieved from [https://agupubs.onlinelibrary.wiley.com/doi/](https://agupubs.onlinelibrary.wiley.com/doi/abs/10.1029/1999JE001025)  
782 [abs/10.1029/1999JE001025](https://agupubs.onlinelibrary.wiley.com/doi/abs/10.1029/1999JE001025) doi: <https://doi.org/10.1029/1999JE001025>
- 783 Genthon, C., Veron, D., Vignon, E., Six, D., Dufresne, J.-L., Madeleine, J.-B., ... Forget,  
784 F. (2021). 10 years of temperature and wind observation on a 45 m tower at dome  
785 c, east antarctic plateau. *Earth System Science Data*, 13(12), 5731-5746. Retrieved  
786 from <https://essd.copernicus.org/articles/13/5731/2021/> doi: 10.5194/essd-  
787 13-5731-2021
- 788 Girard, C., & Delage, Y. (1990). Stable schemes for nonlinear vertical diffusion  
789 in atmospheric circulation models. *Monthly Weather Review*, 118(3), 737 -  
790 745. Retrieved from [https://journals.ametsoc.org/view/journals/mwre/118/](https://journals.ametsoc.org/view/journals/mwre/118/3/1520-0493_1990_118_0737_ssfvnd_2_0_co_2.xml)  
791 [3/1520-0493\\_1990\\_118\\_0737\\_ssfvnd\\_2\\_0\\_co\\_2.xml](https://journals.ametsoc.org/view/journals/mwre/118/3/1520-0493_1990_118_0737_ssfvnd_2_0_co_2.xml) doi: [https://doi.org/10.1175/](https://doi.org/10.1175/1520-0493(1990)118(0737:SSFNVD)2.0.CO;2)  
792 [1520-0493\(1990\)118\(0737:SSFNVD\)2.0.CO;2](https://doi.org/10.1175/1520-0493(1990)118(0737:SSFNVD)2.0.CO;2)
- 793 Golaz, J.-C., Larson, V. E., & Cotton, W. R. (2002). A pdf-based model for boundary  
794 layer clouds. part i: Method and model description. *Journal of the Atmospheric*  
795 *Sciences*, 59(24), 3540 - 3551. Retrieved from [https://journals.ametsoc.org/](https://journals.ametsoc.org/view/journals/atsc/59/24/1520-0469_2002_059_3540_apbmf_2_0_co_2.xml)  
796 [view/journals/atsc/59/24/1520-0469\\_2002\\_059\\_3540\\_apbmf\\_2\\_0\\_co\\_2.xml](https://journals.ametsoc.org/view/journals/atsc/59/24/1520-0469_2002_059_3540_apbmf_2_0_co_2.xml) doi:  
797 [https://doi.org/10.1175/1520-0469\(2002\)059\(3540:APBMFB\)2.0.CO;2](https://doi.org/10.1175/1520-0469(2002)059(3540:APBMFB)2.0.CO;2)
- 798 Grisogono, B. (2010). Generalizing 'z-less' mixing length for stable boundary layers.  
799 *Quarterly Journal of the Royal Meteorological Society*, 136(646), 213-221. doi:  
800 <https://doi.org/10.1002/qj.529>
- 801 Grisogono, B., & Belušić, D. (2008). Improving mixing length-scale for stable boundary lay-  
802 ers. *Quarterly Journal of the Royal Meteorological Society*, 134(637), 2185-2192. Re-  
803 trieved from <https://rmets.onlinelibrary.wiley.com/doi/abs/10.1002/qj.347>  
804 doi: <https://doi.org/10.1002/qj.347>
- 805 He, Y., McFarlane, N. A., & Monahan, A. H. (2019). A new tke-based parameterization of  
806 atmospheric turbulence in the canadian global and regional climate models. *Journal of*  
807 *Advances in Modeling Earth Systems*, 11(5), 1153-1188. doi: [https://doi.org/10.1029/](https://doi.org/10.1029/2018MS001532)  
808 [2018MS001532](https://doi.org/10.1029/2018MS001532)
- 809 Hersbach, H., Bell, B., Berrisford, P., Hirahara, S., Horányi, A., Muñoz-Sabater, J., ...  
810 Thépaut, J.-N. (2020). The era5 global reanalysis. *Quarterly Journal of the Royal*  
811 *Meteorological Society*, 146, 1999-2049. doi: 10.1002/qj.3803
- 812 Holtslag, A. A. M., & Boville, B. A. (1993). Local versus non-local boundary layer diffusion  
813 in a global climate model. *J Clim*, 6, 1825-1842.
- 814 Holtslag, A. A. M., Svensson, G., Baas, P., Basu, S., Beare, B., Beljaars, A. C. M., ...  
815 Van de Wiel, B. J. H. (2013). Stable boundary layers and diurnal cycles. *Bull Amer*  
816 *Meteor Soc*, 94, 1691-1706. (doi:10.1175/BAMS-D-11-00187.1.)

- 817 Hourdin, F., Couvreaux, F., & Menut, L. (2002). Parameterization of the dry convective  
818 boundary layer based on a mass flux representation of thermals. *J Atmos Sci*, *59*,  
819 1105-1123.
- 820 Hourdin, F., Jam, A., Rio, C., Couvreaux, F., Sandu, I., Lefebvre, M.-P., ... Idelkadi, A.  
821 (2019). Unified parameterization of convective boundary layer transport and clouds  
822 with the thermal plume model. *Journal of Advances in Modeling Earth Systems*,  
823 *11*(9), 2910-2933. doi: <https://doi.org/10.1029/2019MS001666>
- 824 Hourdin, F., Rio, C., Grandpeix, J.-Y., Madeleine, J.-B., Cheruy, F., Rochetin, N., ...  
825 Ghattas, J. (2020). Lmdz6a: the atmospheric component of the ipsl climate model  
826 with improved and better tuned physics. *Journal of Advances in Modeling Earth  
827 Systems*. doi: 10.1029/2019MS001892
- 828 Hourdin, F., Williamson, D., Rio, C., Couvreaux, F., Roehrig, R., Villefranque, N., ...  
829 Volodina, V. (2021). Process-based climate model development harnessing machine  
830 learning: Ii. model calibration from single column to global. *Journal of Advances in  
831 Modeling Earth Systems*, *13*(6), e2020MS002225. Retrieved from [https://agupubs  
832 .onlinelibrary.wiley.com/doi/abs/10.1029/2020MS002225](https://agupubs.onlinelibrary.wiley.com/doi/abs/10.1029/2020MS002225) doi: [https://doi  
833 .org/10.1029/2020MS002225](https://doi.org/10.1029/2020MS002225)
- 834 Jose Rodriguez-Manfredi. (2019). *Apss twins data*. NASA Planetary Data System. Re-  
835 trieved from [https://pds.nasa.gov/ds-view/pds/viewBundle.jsp?identifier=  
836 urn:nasa:pds:insight\\_twins&version=3.2](https://pds.nasa.gov/ds-view/pds/viewBundle.jsp?identifier=urn:nasa:pds:insight_twins&version=3.2) doi: 10.17189/1518950
- 837 Kahre, M. A., Murphy, J. R., Newman, C. E., Wilson, R. J., Cantor, B. A., Lemmon, M. T.,  
838 & Wolff, M. J. (2017). The Mars dust cycle. In *The atmosphere and climate of Mars*  
839 (p. 295-337). Cambridge University Press. doi: 10.1017/9781139060172.010
- 840 Kalnay, E., & Kanamitsu, M. (1988). Time schemes for strongly nonlinear  
841 damping equations. *Monthly Weather Review*, *116*(10), 1945 - 1958. Re-  
842 trieved from [https://journals.ametsoc.org/view/journals/mwre/116/10/1520  
843 -0493\\_1988\\_116\\_1945\\_tsfsnd\\_2\\_0\\_co\\_2.xml](https://journals.ametsoc.org/view/journals/mwre/116/10/1520-0493_1988_116_1945_tsfsnd_2_0_co_2.xml) doi: [https://doi.org/10.1175/1520  
844 -0493\(1988\)116\(1945:TSFSND\)2.0.CO;2](https://doi.org/10.1175/1520-0493(1988)116(1945:TSFSND)2.0.CO;2)
- 845 Kolmogorov, A. N. (1941). Energy dissipation in locally isotropic turbulence. *Doklady AN  
846 SSSR*, *32*, 19-21.
- 847 Lange, L., Forget, F., Dupont, E., Vandemeulebrouck, R., Spiga, A., Millour, E., ...  
848 Bierjon, A. (2023). Modeling slope microclimates in the mars planetary climate  
849 model. *Journal of Geophysical Research: Planets*, *128*(10), e2023JE007915. doi:  
850 10.1029/2023JE007915
- 851 Lenderink, G., & Holtslag, A. A. M. (2000). Evaluation of the kinetic energy approach  
852 for modeling turbulent fluxes in stratocumulus. *Monthly Weather Review*, *128*(1), 244  
853 - 258. Retrieved from [https://journals.ametsoc.org/view/journals/mwre/128/  
854 1/1520-0493\\_2000\\_128\\_0244\\_eotkea\\_2\\_0\\_co\\_2.xml](https://journals.ametsoc.org/view/journals/mwre/128/1/1520-0493_2000_128_0244_eotkea_2_0_co_2.xml) doi: [https://doi.org/10.1175/  
855 1520-0493\(2000\)128\(0244:EOTKEA\)2.0.CO;2](https://doi.org/10.1175/1520-0493(2000)128(0244:EOTKEA)2.0.CO;2)
- 856 Lenderink, G., & Holtslag, A. A. M. (2004). An updated length-scale formulation for  
857 turbulent mixing in clear and cloudy boundary layers. *Quarterly Journal of the  
858 Royal Meteorological Society*, *130*(604), 3405-3427. Retrieved from [https://rmets  
859 .onlinelibrary.wiley.com/doi/abs/10.1256/qj.03.117](https://rmets.onlinelibrary.wiley.com/doi/abs/10.1256/qj.03.117) doi: [https://doi.org/  
860 10.1256/qj.03.117](https://doi.org/10.1256/qj.03.117)
- 861 Li, D. (2019). Turbulent prandtl number in the atmospheric boundary layer - where  
862 are we now? *Atmospheric Research*, *216*, 86-105. Retrieved from [https://  
863 www.sciencedirect.com/science/article/pii/S0169809518307324](https://www.sciencedirect.com/science/article/pii/S0169809518307324) doi: [https://  
864 doi.org/10.1016/j.atmosres.2018.09.015](https://doi.org/10.1016/j.atmosres.2018.09.015)
- 865 Li, D., Katul, G. G., & Zilitinkevich, S. S. (2016). Closure schemes for stably stratified  
866 atmospheric flows without turbulence cutoff. *Journal of the Atmospheric Sciences*,  
867 *73*(12), 4817 - 4832. doi: <https://doi.org/10.1175/JAS-D-16-0101.1>
- 868 Louis, J.-F. (1979). A parametric model of vertical eddy fluxes in the atmosphere. *Boundary-  
869 Layer Meteorol*, *17*, 187-202. (doi: 10.1007/BF00712379)
- 870 Louis, J. F., Tiedtke, M., & Geleyn, J.-F. (1982). A short history of the operational pbl  
871 parametrization at ECMWF. *Paper presented at the ECMWF workshop on boundary*

- 872 *layer parametrization, ECMWF, Reading.*
- 873 Mašek, J., Ďurán, I. B., & Brožková, R. (2022). Stable numerical implementation of  
874 a turbulence scheme with two prognostic turbulence energies. *Monthly Weather*  
875 *Review*, 150(7), 1667 - 1688. Retrieved from [https://journals.ametsoc.org/  
876 view/journals/mwre/150/7/MWR-D-21-0172.1.xml](https://journals.ametsoc.org/view/journals/mwre/150/7/MWR-D-21-0172.1.xml) doi: [https://doi.org/10.1175/  
877 MWR-D-21-0172.1](https://doi.org/10.1175/MWR-D-21-0172.1)
- 878 Mellor, G. L., & Yamada, T. (1974). A hierarchy of turbulence closure models for planetary  
879 boundary layers. *J Atmos Sci*, 30, 1061-1069.
- 880 Mellor, G. L., & Yamada, T. (1982). Development of a turbulence closure model for  
881 geophysical fluid problems. *Rev Geophys Space Phys*, 20(4), 851-875.
- 882 Montabone, L., Forget, F., Millour, E., Wilson, R., Lewis, S., Cantor, B., ... Wolff, M.  
883 (2015). Eight-year climatology of dust optical depth on mars. *Icarus*, 251, 65–95. doi:  
884 10.1016/j.icarus.2014.12.034
- 885 Nieuwtsadt, F. T. M. (1984). The turbulent structure of the stable, nocturnal boundary  
886 layer. *J Atmos Sci*, 41, 2202-2217.
- 887 Petrosyan, A., Galperin, B., Larsen, S. E., Lewis, S. R., Määttänen, A., Read, P. L., ...  
888 Vázquez, L. (2011). The martian atmospheric boundary layer. *Reviews of Geo-*  
889 *physics*, 49(3). Retrieved from [https://agupubs.onlinelibrary.wiley.com/doi/  
890 abs/10.1029/2010RG000351](https://agupubs.onlinelibrary.wiley.com/doi/abs/10.1029/2010RG000351) doi: <https://doi.org/10.1029/2010RG000351>
- 891 Pottier, A., Forget, F., Montmessin, F., Navarro, T., Spiga, A., Millour, E., ... Madeleine,  
892 J.-B. (2017). Unraveling the martian water cycle with high-resolution global climate  
893 simulations. *Icarus*, 291, 82–106. doi: 10.1016/j.icarus.2017.02.016
- 894 Rio, C., Hourdin, F., Couvreur, F., & Jam, A. (2010). Resolved versus parametrized  
895 boundary-layer plumes. Part II: continuous formulations of mixing rates for mass-flux  
896 schemes. *Boundary-layer Meteorol.* (Doi:10.1007/s10546-010-9478)
- 897 Rodier, Q., Masson, V., Couvreur, F., & Paci, A. (2017). Evaluation of a buoyancy and  
898 shear based mixing length for a turbulence scheme. *Frontiers in Earth Science*, 5, 65.  
899 doi: 10.3389/feart.2017.00065
- 900 Sandu, I., Beljaars, A., Bechtold, P., Mauritsen, T., & Balsamo, G. (2013). Why is it so  
901 difficult to represent stably stratified conditions in numerical weather prediction (nwp)  
902 models. *J Adv Model Earth Syst*, 5, 117-133. (doi: 10.1002/jame.20013)
- 903 Spiga, A., Forget, F., Lewis, S. R., & Hinson, D. P. (2010a). Structure and dynamics of  
904 the convective boundary layer on mars as inferred from large-eddy simulations and  
905 remote-sensing measurements. *Quarterly Journal of the Royal Meteorological Society*,  
906 136(647), 414-428. Retrieved from [https://rmets.onlinelibrary.wiley.com/doi/  
907 abs/10.1002/qj.563](https://rmets.onlinelibrary.wiley.com/doi/abs/10.1002/qj.563) doi: <https://doi.org/10.1002/qj.563>
- 908 Spiga, A., Forget, F., Lewis, S. R., & Hinson, D. P. (2010b). Structure and dynamics of  
909 the convective boundary layer on Mars as inferred from large-eddy simulations and  
910 remote-sensing measurements. *Quarterly Journal of the Royal Meteorological Society*,  
911 136(647), 414-428. doi: 10.1002/qj.563
- 912 Stull, R. B. (1990). *An introduction to boundary layer meteorology*. Kluwer, Boston.
- 913 Sun, J. (2011). Vertical variations of mixing lengths under neutral and stable conditions  
914 during cases-99. *Journal of Applied Meteorology and Climatology*, 50(10), 2030 - 2041.  
915 Retrieved from [https://journals.ametsoc.org/view/journals/apme/50/10/jamc-  
916 -d-10-05006.1.xml](https://journals.ametsoc.org/view/journals/apme/50/10/jamc-d-10-05006.1.xml) doi: <https://doi.org/10.1175/JAMC-D-10-05006.1>
- 917 Tiedtke, M. (1989). A comprehensive mass flux scheme for cumulus parameterization in  
918 large-scale models. *Monthly Weather Review*, 117(8), 1779 - 1800. doi: [https://  
919 doi.org/10.1175/1520-0493\(1989\)117<1779:ACMFSF>2.0.CO;2](https://doi.org/10.1175/1520-0493(1989)117<1779:ACMFSF>2.0.CO;2)
- 920 van der Linden, S. J., Edwards, J. M., van Heerwaarden, C. C., Vignon, E., Genthon, C.,  
921 Petenko, I., ... van de Wiel, B. J. (2019). Large-eddy simulations of the steady  
922 wintertime antarctic boundary layer. *Boundary-Layer Meteorology*, 173(2), 165–192.  
923 doi: 10.1007/s10546-019-00461-4
- 924 van de Wiel, B. J. H., Moene, A. F., H., D. R. W., & Jonker, H. J. J. (2008). Local similarity  
925 in the stable boundary layer and mixing-length approaches: consistency of concepts.  
926 *Boundary-Layer Meteorol*, 128, 103-116.

- 927 van de Wiel, B. J. H., Moene, A. F., Steeneveld, G. J., Baas, P., Bosveld, F. C., & Holstlag,  
 928 A. A. M. (2010). A conceptual view on inertial oscillations and nocturnal low-level  
 929 jets. *J Atmos Sci*, *67*, 2679-2689. (doi: 10.1175/2010JAS3289.1)
- 930 van de Wiel, B. J. H., Vignon, E., Baas, P., van Hooijdonk, I. G. S., van der Linden,  
 931 S. J. A., van Hooft, J. A., ... Genthon, C. (2017). Regime transition in near-  
 932 surface temperature inversions: a conceptual model. *J Atmos Sci*, *74*, 1057-1073.  
 933 (doi:10.1175/JAS-D-16-0180.1)
- 934 Venayagamoorthy, S. K., & Stretch, D. D. (2010). On the turbulent prandtl number in  
 935 homogeneous stably stratified turbulence. *Journal of Fluid Mechanics*, *644*, 359-369.  
 936 doi: 10.1017/S002211200999293X
- 937 Vignon, E., Hourdin, F., Genthon, C., Gallée, H., Bazile, E., Lefebvre, M.-P., ... Van de  
 938 Wiel, B. J. H. (2017). Parametrization of the boundary layer over the antarctic plateau  
 939 in a general circulation model: 1D simulations against summertime observations at  
 940 Dome C. *J Geophys Res Atmos*, *122*. (doi: 10.1002/2017JD026802)
- 941 Vignon, E., Hourdin, F., Genthon, C., Van de Wiel, B. J. H., , Gallée, H., ... Beaumet, J.  
 942 (2018). Modeling the dynamics of the atmospheric boundary layer over the antarctic  
 943 plateau with a general circulation model. *Journal of Advances in Modeling Earth*  
 944 *Systems*. (10.1002/2017MS001184)
- 945 Vignon, E., van de Wiel, B. J. H., van Hooijdonk, I. G. S., Genthon, C., van der Linden,  
 946 S. J. A., van Hooft, J. A., ... Casasanta, G. (2017). Stable boundary layer regimes  
 947 at Dome C, Antarctica: observation and analysis. *Q J R Meteorol Soc*, *143*(704),  
 948 1241-1253. (doi:10.1002/qj.2998)
- 949 Weiss, B. P., & Ingersoll, A. P. (2000). Cold spots in the martian polar regions: Evidence  
 950 of carbon dioxide depletion? *Icarus*, *144*(2), 432-435. doi: 10.1006/icar.1999.6302
- 951 Yamada, T. (1975). A simulation of the wangara atmospheric boundary layer data. *J Atmos*  
 952 *Sci*, *32*, 2309-2320.
- 953 Yamada, T. (1983). Simulations of nocturnal drainage flows by a  $q^2l$  turbulence closure  
 954 model. *J Atmos Sci*, *40*, 91-106.
- 955 Zilitinkevich, S., Elperin, T., Kleeorin, N., & Rogachevskii, I. (2007). Energy and flux-  
 956 budget turbulence closure model for stably stratified flows. Part I: Steady state, ho-  
 957 mogeneous regime. *Boundary-Layer Meteorol*, *125*, 167-191. (doi:10.1007/s10546-007-  
 958 9189-2)
- 959 Zilitinkevich, S., Elperin, T., Kleeorin, N., Rogachevskii, I., Esau, I., Mauritsen, T., & Miles,  
 960 M. W. (2008). Turbulence energetics in stably stratified geophysical flows: Strong  
 961 and weak mixing regimes. *Q J R Meteorol Soc*, *134*, 793-799. (doi:10.1002/qj.264)

# Designing a fully-tunable and versatile TKE-1 turbulence parameterization for atmospheric models

É. Vignon<sup>1</sup>, K. Arjdal<sup>1,2</sup>, F. Cheruy<sup>1</sup>, M. Coulon-Decorzens<sup>1</sup>, C. Dehondt<sup>3</sup>, T.  
Dubos<sup>1</sup>, S. Fromang<sup>3</sup>, F. Hourdin<sup>1</sup>, L. Lange<sup>1</sup>, L. Raillard<sup>1</sup>, G. Rivière<sup>1</sup>, R.  
Roehrig<sup>4</sup>, A. Sima<sup>1</sup>, A. Spiga<sup>1</sup>, P. Tiengou<sup>1,5</sup>

<sup>1</sup>Laboratoire de Météorologie Dynamique- IPSL, Sorbonne Université/CNRS/ Ecole Normale

Supérieure-PSL Université/ Ecole Polytechnique-Institut Polytechnique de Paris, Paris, France

<sup>2</sup>International Water Research Institute (IWRI), CSAES - Mohammed VI Polytechnic University,

Benguerir, Morocco

<sup>3</sup>Laboratoire des Sciences du Climat et de l'Environnement, LSCE/IPSL, CEA-CNRS-UVSQ, Université

Paris-Saclay, F-91191, Gif-sur-Yvette, France.

<sup>4</sup>CNRM, Université de Toulouse, Météo-France, CNRS, Toulouse, France

<sup>5</sup>Milieux environnementaux, transferts et interaction dans les hydrosystèmes et les sols (Metis)/Sorbonne

Université/IPSL/CNRS/ EPHE, Paris, France

## Key Points:

- A simple TKE-1 turbulent diffusion scheme is developed in a semi-heuristic way for applications in models of the Earth and Mars atmospheres.
- The parameterization is designed to be completely tunable and numerically stable at typical GCM time steps.
- The parameterization is tuned over 1D simulations and is able to capture the Antarctic and Martian stable boundary layers in 3D simulations.

---

Corresponding author: Étienne Vignon, [etienne.vignon@lmd.ipsl.fr](mailto:etienne.vignon@lmd.ipsl.fr)

**Abstract**

This study presents the development of a TKE-1 parameterization of the diffusion coefficients for the representation of turbulent diffusion in neutral and stable conditions in large-scale atmospheric models. The parameterization has been carefully designed to be completely tunable in the sense that all adjustable parameters have been clearly identified and their number minimized as much as possible to help the calibration and to thoroughly assess the parametric sensitivity. We choose a mixing length formulation that depends on both static stability and wind shear to cover the different regimes of stable boundary layers. We follow a heuristic approach for expressing the stability functions and turbulent Prandtl number in order to guarantee the versatility of the scheme and its applicability for planetary atmospheres composed of an ideal and perfect gas such as that of Earth and Mars. Particular attention has also been paid to the numerical stability at typical time steps used in General Circulation Models. Test, parametric sensitivity assessment and preliminary tuning are performed on single-column idealized simulations of the weakly stable boundary layer. The robustness and versatility of the scheme are also assessed through its implementation in the LMDZ General Circulation Model and the Mars Planetary Climate Model and by running simulations of the Antarctic and Martian nocturnal boundary layers.

**Plain Language Summary**

In planetary atmospheres, turbulent motions actively contribute to the mixing of quantities such as heat, momentum and chemical species. Such motions are not resolved in coarse-grid atmospheric models and have to be parameterized. The parameterization of turbulent mixing should be based on physical laws and sufficiently sophisticated to realistically represent the full spectrum of motions over the full range of stability encountered in the atmospheres. However, it also necessarily contains a number of closure parameters not always well identified and whose values are determined empirically - thereby questioning the universality of the parameterization and its potential application over the full globe or even to other planets - or adjusted to guarantee the numerical stability of the model. This study presents the design of a turbulent mixing parameterization that can be fully calibrated and applied in planetary atmospheres such as that of Mars. We then calibrate the parameterization on an idealised simulation set-up and test its robustness and performance by running simulations of the Antarctic and Martian atmospheres.

**1 Introduction**

Turbulence efficiently transports momentum, energy, moisture and matter in the atmosphere, particularly in the planetary boundary layer where it controls sensible and latent heat fluxes as well as the transfer of momentum between the air and the ground surface. It thereby directly affects the diurnal cycle of the near-surface atmospheric quantities and also impacts on the lifetime and structure of synoptic-scale dynamical systems. Turbulent transport is therefore an essential component of the physics of climate models, numerical weather prediction models and more generally of General Circulation Models (GCMs) of planetary atmospheres. As turbulent eddies manifests on scales ranging from a few millimeters to a few tens of kilometers in deep convective systems, modellers develop conceptually separated subgrid parameterizations targeting different types - or different scales - of transport processes. Non-local turbulent transport resulting from large and organised convective cells, being deep or shallow, is often treated with so-called mass flux schemes (e.g., Tiedtke (1989); Emanuel (1991); Hourdin et al. (2002); Golaz et al. (2002)). Local turbulent mixing which results from eddies whose typical size is smaller or similar to the typical grid cell thickness - namely a few tens of meters - is often parameterized with a local K-gradient diffusion scheme. In those schemes, the turbulent flux is parameterized with a Fick's law type down-gradient diffusion formulation that relies on the introduction of a turbulent diffusion coefficient. Such schemes are particularly critical to simulate the stable and neutral

72 atmospheric boundary layers (Delage, 1997; Cuxart et al., 2006; Sandu et al., 2013), the  
 73 land-atmosphere coupling as well as the thermal inversion at the top of convective boundary  
 74 layers.

75 Several K-gradient diffusion parameterizations have been developed since the pioneering  
 76 work of Louis (1979) and have been the subject of a substantial body of literature in at-  
 77 mospheric sciences. Among them, the moderate-complexity 1.5 order schemes, or TKE-l  
 78 schemes, consist in expressing the diffusion coefficients as function of a diagnostic vertical  
 79 turbulent length-scale, or mixing length, and of a prognostic estimation of the Turbulent  
 80 Kinetic Energy (TKE) (Mellor & Yamada, 1982; Yamada, 1983).

81 The closure of the TKE evolution equation and the empirical and/or heuristic formu-  
 82 lation of the mixing-length necessarily introduce free parameters in the parameterization,  
 83 and therefore a certain degree of empiricism in the expression of the diffusion coefficients (Li  
 84 et al., 2016). Indeed, such parameters do not have, by essence, fixed and universal values.  
 85 Some of them - and the associated variability range thereof - are determined empirically  
 86 using field observations, laboratory experiments, Large Eddy Simulations (LES) or Direct  
 87 Numerical Simulations (DNS) while others are arbitrarily set. In practice, in climate and  
 88 numerical weather prediction models, the value of some coefficients is often retuned to match  
 89 large-scale or meteorological targets. For instance as all subgrid mixing processes are not  
 90 parameterized - such as small scale internal waves or submeso-scale motions - the mixing in  
 91 stable conditions is often artificially enhanced to prevent unrealistic runaway surface cool-  
 92 ing due to surface-atmosphere mechanical decoupling and to maintain sufficient surface drag  
 93 and Ekman pumping in extratropical cyclones (Holtslag et al., 2013; Sandu et al., 2013).  
 94 Such empiricism and Earth-oriented tuning can somewhat question the applicability of these  
 95 turbulent mixing parameterizations in planetary GCMs, even in GCMs of Mars (e.g., Forget  
 96 et al. (1999); Colaitis et al. (2013)) where the planetary boundary layer shares similarities  
 97 with that on Earth (Spiga et al., 2010a).

98 In addition, arbitrary parameter calibration - sometimes beyond reasonable ranges -  
 99 is often required to improve the numerical convergence and stability of the parameteriza-  
 100 tion once it is implemented in models with typical physics time steps of a few minutes to  
 101 a few tens of minutes. Indeed, the numerical implementation of a K-gradient turbulence  
 102 scheme is prone to spurious oscillations called ‘fibrillations’ (Kalnay & Kanamitsu, 1988;  
 103 Girard & Delage, 1990). Such fibrillations are due to *i*) the coupling between momentum  
 104 and potential temperature via the turbulent diffusion coefficients and *ii*) the discretization  
 105 of the vertical diffusion in which the nonlinear exchange coefficient is often treated explicitly  
 106 in time. Even though the TKE budget is often close to a local equilibrium (Lenderink &  
 107 Holtslag, 2004), the prognostic prediction of the TKE generally makes TKE-l schemes less  
 108 sensitive to the time discretization and less prone to fibrillation than traditional first-order  
 109 schemes (Bougeault & Lacarrère, 1989; Bazile et al., 2011) in which the diffusion coefficients  
 110 are explicit and diagnostic functions of the mean static stability and wind shear (Louis, 1979;  
 111 Louis et al., 1982; Delage, 1997). This is mostly explained by the fact that the prognostic  
 112 TKE plays a role of ‘reservoir’ that damps the sometimes abrupt evolution of the diffusion  
 113 coefficients with time (Mašek et al., 2022). However, even TKE-based schemes can also  
 114 be affected by numerical instabilities which can be related to the numerical treatment of  
 115 the TKE equation itself (Deleersnijder, 1992; Vignon et al., 2018) or to the coupling with  
 116 other prognostic quantities such as the turbulent potential energy (Mašek et al., 2022). The  
 117 numerical treatment of the TKE equation and more generally of the turbulent diffusion  
 118 thereby comes out as a forefront issue in atmospheric modeling. Hence, one has to find  
 119 a good trade-off between the complexity and sophistication of a turbulent mixing scheme  
 120 and its practical implementation in large scale atmospheric models avoiding as much as  
 121 possible unrealistic parameter calibration to guarantee numerical stability and fair model  
 122 performances.

123

The sensitivity of the stable boundary layer representation to turbulent diffusion calibration in a large scale atmospheric model was assessed in a game-changing study by Audouin et al. (2021) using a semi-automatic tuning tool based on uncertainty quantification (Couvreur et al., 2021; Hourdin et al., 2021). The authors identified a few key tuning parameters - and their acceptable ranges of values - in the TKE-1 turbulent diffusion scheme of the ARPEGE-Climat model and assessed to what extent biases in the simulation of the extremely stable Antarctic boundary layer are explained by structural parameterization deficiencies or tuning choices. However, the boundary layer and surface layer schemes of ARPEGE-Climat contain a large number of tuning parameters, sometimes subtly interdependent, and considering all of them in a tuning exercise may be confusing, thereby challenging.

The present study aims to design a new and simple TKE-1 turbulent diffusion scheme for large scale atmospheric models

1. that is sufficiently robust and versatile to be applicable on both Earth and Mars, and potentially on other planetary atmospheres and ;
2. that is built to be completely tuned in the sense that all adjustable parameters are clearly identified and their number minimized to help the calibration - or parameter adjustment - and assess the parametric sensitivity.

The scheme will be referred to as the ATKE scheme - for Adjustable TKE-1 scheme - in the paper.

We follow a simple heuristic approach - as in Lenderink and Holtslag (2004) and He et al. (2019) - for expressing the stability functions and turbulent Prandtl number to guarantee the versatility of the scheme and its potential applicability for planetary atmospheres composed of an ideal and perfect gas. A particular attention is also paid to the numerical treatment of the TKE prognostic equation to ensure the numerical stability even in conditions of strong wind shear or strong stratification. It is worth emphasizing that the ‘local’ nature of the scheme makes it mostly adapted for neutral and stably stratified conditions, hence the particular focus on stable boundary layers in the paper. The scheme is tested and tuned - using the same Uncertainty Quantification approach as in Audouin et al. (2021) and Hourdin et al. (2021) - on idealized single column simulations of the stable boundary layer. The parameterization is then implemented and tested in the Earth LMDZ GCM (Hourdin et al., 2020; Cheruy et al., 2020) and the Mars Planetary Climate model (Forget et al., 1999) to verify its robustness and assess its performances when challenging the stable Antarctic and Martian nocturnal boundary layers.

## 2 Parameterization development

This section presents the derivation of the ATKE scheme, starting briefly and purposely with some generalities to clearly set the parameterization in the framework of turbulent diffusion in GCMs of planetary atmospheres.

### 2.1 General framework

The conservation law for an extensive quantity  $c$  - being for example the potential temperature, wind components or concentration in chemical species - in a compressible atmosphere reads:

$$\frac{\partial \rho c}{\partial t} + \vec{\nabla}(\rho \vec{u} c) = P_c \quad (1)$$

With, in Cartesian coordinates  $(x, y, z)$ ,  $\vec{u} = u\vec{i} + v\vec{j} + w\vec{k}$  the wind vector,  $\rho$  the air density and  $P_c$  the net source/loss term. We note the statistical (ensemble) average with

an overline and introduce the air weighting average operator  $\sim$  such that

$$\tilde{c} = \frac{\overline{\rho c}}{\bar{\rho}} \quad (2)$$

Note that  $\tilde{c}$  is an extensive variable per mass unit. We decompose  $c$  into a mean state and a fluctuation such that  $c = \tilde{c} + c'$ . We then apply the statistical average operator (overline) on Eq. 1 that now reads:

$$\underbrace{\frac{\partial \overline{\rho \tilde{c}}}{\partial t} + \vec{\nabla}(\overline{\rho \tilde{c} \tilde{u}})}_{(1)} = - \underbrace{\vec{\nabla}(\overline{\rho \tilde{u}' c'}) + \overline{P_c}}_{(2)} \quad (3)$$

In large-scale atmospheric models the scale separation is imposed by the size of the grid cells which determines the resolved and unresolved components. In this framework, the term (1) in Eq.3 is handled by the dynamical core while the term (2) is the essence of the physical subgrid parameterizations. Further assuming that the subgrid horizontal variations of  $c$  are dominated by vertical variations, it follows that  $\vec{\nabla}(\overline{\rho \tilde{u}' c'}) \approx \partial_z(\overline{\rho w' c'})$ . A local turbulent mixing parameterization aims at calculating a tendency on the mean state variable  $\tilde{c}$  due to the vertical turbulent diffusion as follows:

$$\left. \frac{\partial \tilde{c}}{\partial t} \right|_{diffusion} = - \frac{1}{\bar{\rho}} \frac{\partial \overline{\rho w' c'}}{\partial z} \quad (4)$$

163 For better readability and conciseness, we leave the  $\sim$  notation out for mean state quantities  
164 and note  $\rho = \bar{\rho}$  in the following.

For local and mostly shear driven turbulent eddies, the mixing of any conservative quantity during turbulent mixing - such as the common Betts (1973)' variables - can be represented as a diffusive process (e.g. Louis (1979)). Turbulent fluxes can then be expressed with a down-gradient form:  $\overline{\rho w' c'} = -\rho K_c \partial_z c$ ,  $K_c$  being a diffusion coefficient. Eq. 4 hence reads:

$$\left. \frac{\partial c}{\partial t} \right|_{diffusion} = \frac{1}{\rho} \frac{\partial}{\partial z} \left( \rho K_c \frac{\partial c}{\partial z} \right) \quad (5)$$

165 Once the  $K_c$  coefficient has been calculated at vertical model layer interfaces, such an  
166 equation can be numerically solved with an implicit approach through the inversion of a  
167 tri-diagonal matrix.

We now focus on the closure of the  $K_c$  coefficient which is the main scope of the present study. We follow here an approach historically proposed by Mellor and Yamada (1974); Yamada (1975) that is, a 1.5 order closure or TKE-1 scheme. In this framework,  $K_c$  coefficients are expressed as the product of a vertical turbulent length scale or mixing length  $l$  with a turbulent vertical velocity scale taken proportional to the square root of the TKE  $e = \frac{1}{2}(\overline{u'^2} + \overline{v'^2} + \overline{w'^2})$ . The latter is multiplied by a stability function  $S_c$  that accounts for the fact that the turbulence anisotropy - thus the contribution of TKE to vertical turbulent mixing - varies with the local stability of the atmosphere characterized by the gradient Richardson number  $Ri$ . The diffusion coefficient  $K_c$  is then expressed as (Yamada, 1983; Zilitinkevich et al., 2007):

$$K_c = l S_c (Ri) \sqrt{e} \quad (6)$$

168 In the following sections, we describe the estimation of the three different terms of  $K_c$ ,  
169 namely  $e$ ,  $S_c$  and  $l$ . As we want our turbulent scheme to be applicable on Earth and Mars  
170 (and potentially other planetary environments), we have to ensure that their expressions  
171 are as planet-independent as possible.

172

## 2.2 TKE prognostic equation

173

### 2.2.1 Parameterization of the source and loss terms

Assuming the horizontal homogeneity of the subgrid-scale statistics, the TKE obeys the following evolution equation (Stull, 1990):

$$\frac{\partial e}{\partial t} = \underbrace{-\overline{u'w'}\frac{\partial u}{\partial z} - \overline{v'w'}\frac{\partial v}{\partial z}}_{\mathcal{W}} + \underbrace{\overline{b'w'}}_{\mathcal{B}} - \underbrace{\frac{1}{\rho}\frac{\partial}{\partial z}(\overline{\rho w'e} + \overline{w'p'})}_{\mathcal{T}} \underbrace{-\epsilon}_{\mathcal{D}} \quad (7)$$

174

$\mathcal{W}$  is the wind shear production term that can be expressed with the down-gradient expression of fluxes with a diffusion coefficient for momentum hereafter denoted as  $K_m$ :

175

$$-\overline{u'w'}\frac{\partial u}{\partial z} - \overline{v'w'}\frac{\partial v}{\partial z} = K_m S^2 = l S_m \sqrt{e} S^2 \quad (8)$$

with  $S^2 = (\partial_z u)^2 + (\partial_z v)^2$  the wind shear and  $S_m$  the stability function for momentum.  $\mathcal{B}$  is the buoyancy  $b$  production/consumption term. For a dry air under the ideal gas assumption, one can write:

$$\overline{b'w'} = \frac{-g}{\rho} \left. \frac{\partial \rho}{\partial \theta} \right|_p \overline{w'\theta'} = \frac{g}{\theta} \overline{w'\theta'} = -K_h \frac{g}{\theta} \frac{\partial \theta}{\partial z} = -K_h N^2 = -l S_h \sqrt{e} N^2 \quad (9)$$

where  $g$  is the gravity acceleration of the planet,  $\theta$  the potential temperature,  $N$  the Brünt-Väisälä pulsation,  $K_h$  the diffusion coefficient for heat and  $S_h$  the stability function for heat. In the case of an atmosphere containing water vapor or chemical species  $\xi$ , buoyancy reads  $\overline{b'w'} = \frac{-g}{\rho} \left( \left. \frac{\partial \rho}{\partial \theta} \right|_{p,\xi} \overline{w'\theta'} + \left. \frac{\partial \rho}{\partial \xi} \right|_{p,\theta} \overline{w'\xi'} \right)$ . For water vapor - in absence of phase change - or for non-reactive chemical species, one can define a virtual temperature  $T_v$  (and a subsequent virtual potential temperature  $\theta_v$ ) corresponding to the temperature that dry air would have if its pressure and density were equal to those of a given sample of the mixture of gas. In this case:

$$\overline{b'w'} \simeq \frac{g}{\theta_v} \overline{w'\theta'_v} = -\frac{g}{\theta_v} K_h \frac{\partial \theta_v}{\partial z} \quad (10)$$

176

It is worth noting here that the expression of the buoyancy term (or Brünt-Väisälä pulsation) is gravity-dependent thus planet-dependent. For simplicity and consistency with previous literature on turbulent mixing schemes, we keep the formalism with explicit gravity in the following. However, a more universal derivation of the scheme can be achieved with a gravity-invariant formulation of the TKE and turbulent diffusion equations. Such a formulation is proposed in Appendix A.

177

178

179

180

181

182

$\mathcal{D}$  is the viscous TKE dissipation term that can be expressed following Kolmogorov (1941):

$$\epsilon = \frac{e^{3/2}}{l_\epsilon} \quad (11)$$

183

184

185

186

187

188

189

190

with  $l_\epsilon$  the dissipation length-scale characterizing the size of the most dissipative and energy-containing eddies. Following for instance Yamada (1983) and Bougeault and Lacarrère (1989), we assume that  $l_\epsilon$  scales with  $l$  such that  $l_\epsilon = c_\epsilon l$ ,  $c_\epsilon$  being a scalar. Its value roughly ranges between 1.2 and 10.0 (Yamada, 1983; Audouin et al., 2021; He et al., 2019) since dissipation length scale - characterizing the dissipation of turbulence as a whole - might be larger than vertical mixing length in stable conditions due to the fact that kinetic energy can dissipate through wavy motion with little transfer to the smaller turbulent scales (Cuxart et al., 2006).

The vertical turbulent flux of TKE and the pressure term gathered in  $\mathcal{T}$  redistribute TKE through the depth of the atmospheric column. Hence, those two terms are commonly

grouped together and expressed as a TKE turbulent diffusion term:

$$-\frac{1}{\rho} \frac{\partial}{\partial z} (\overline{\rho w' e} + \overline{w' p'}) = \frac{1}{\rho} \frac{\partial}{\partial z} (\rho K_e \frac{\partial e}{\partial z}) \quad (12)$$

191  $K_e$  being taken proportional to  $K_m$  (Yamada, 1983; Bougeault & Lacarrère, 1989;  
 192 Lenderink & Holtslag, 2004):  $K_e = c_e K_m$ .  $c_e$  is a constant whose value is generally around  
 193 1 - 2 and that we will arbitrarily allow to vary between 1 and 5 (Bougeault & Lacarrère,  
 194 1989; Lenderink & Holtslag, 2004; Baas et al., 2018). The lower boundary condition of  $e$   
 195 that is, the surface value of the TKE  $e_s$ , is estimated by assuming stationary near-neutral  
 196 conditions in the surface layer. On such a condition (Baas et al., 2018; Lenderink & Holtslag,  
 197 2004):

$$e_s = c_s u_*^2 \quad (13)$$

with  $c_s$  a constant and  $u_*$  the surface friction velocity calculated from the surface drag  
 coefficient for momentum and the wind speed at the first model level. A proper scaling of  
 the TKE-1 parameterization with the Monin-Obukhov similarity in the surface layer requires  
 (He et al., 2019):

$$c_s = c_\epsilon^{2/3} \quad (14)$$

### 198 **2.2.2 Numerical treatment**

199 Once the different TKE source and loss terms have been expressed, Eq. 7 has to be  
 200 integrated in time. The numerical treatment of Eq. 7 is critical as the solution must be  
 201 stable and converge at typical physical time steps used in atmospheric GCMs namely, of  
 202 the order of  $\approx 15$  min. Several methods have been proposed in the literature, particularly  
 203 regarding the treatment of the dissipation term with different degrees of implicitation (Bazile  
 204 et al., 2011).

205 Here, we propose a 2-step resolution method which allows for an exact treatment of  
 206 the dissipation term - under some assumptions - while the transport term is calculated  
 207 separately.

208 *Step 1* We calculate the TKE tendency due to the shear, buoyancy and dissipation  
 209 terms. Noting  $q = \sqrt{2e}$ , one can rewrite Eq. 7 with no transport term as:

$$\frac{\partial q}{\partial t} = \frac{l S_m}{\sqrt{2}} S^2 \left( 1 - \frac{Ri}{Pr} \right) - \frac{q^2}{2^{3/2} c_\epsilon l} \quad (15)$$

210 with  $Pr = \frac{K_m}{K_h} = \frac{S_m}{S_h}$  the turbulent Prandtl number. We then solve this equation through  
 211 an implicit treatment of  $q$  assuming that the mean temperature and wind field does not  
 212 vary much during the time step  $\delta t$  and thus keeping the explicit value - that is the value at  
 213 the beginning of the time step - of  $Ri$ ,  $S_m$ ,  $Pr$  and  $l$ . Eq. 16 then reads:

$$\frac{q_{t+\delta t} - q_t}{\delta t} = \frac{l S_m}{\sqrt{2}} S^2 \left( 1 - \frac{Ri}{Pr} \right) - \frac{q_{t+\delta t}^2}{2^{3/2} c_\epsilon l} \quad (16)$$

than can be rewritten in a second-order polynomial form after some rearrangement :

$$q_{t+\delta t}^2 + A_t q_{t+\delta t} + B_t = 0 \quad (17)$$

214 with  $A_t = \frac{c_\epsilon l 2^{3/2}}{\delta t}$  and  $B_t = -\left( \frac{q_t c_\epsilon l 2^{3/2}}{\delta t} + 2l^2 c_\epsilon S_m S^2 \left( 1 - \frac{Ri}{Pr} \right) \right)$

215 One can show that given the choice we will make for the formulation of the turbulent  
 216 Prandtl number in the next section,  $Ri/Pr$  namely the flux Richardson number, is by con-  
 217 struction always  $< 1$ . This in fact reflects a condition imposed by steady-state TKE budget

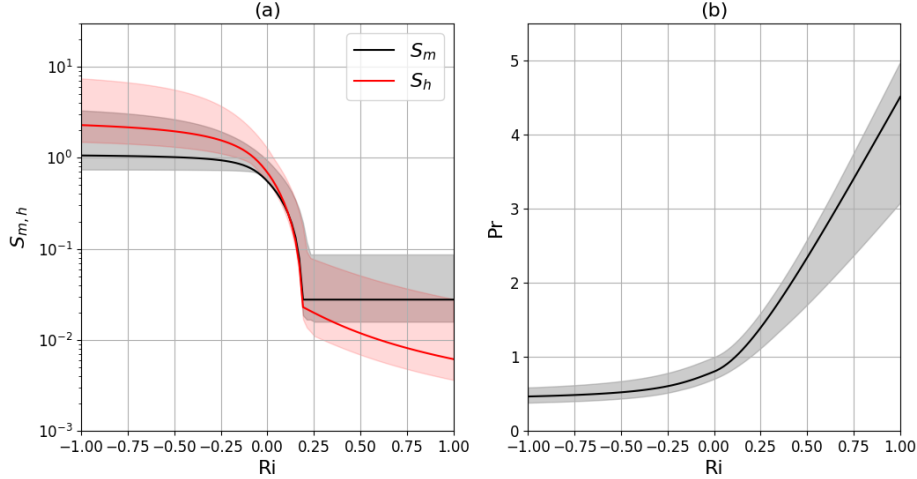


**Figure 1.**  $S_{m,h}$  (panel a) and  $Pr$  (panel b) as functions of the Richardson number  $Ri$  following Eq. 20 and 23. Envelopes show the range of variation when adjustable parameters evolve in their range of acceptable values (Table 1). Solid lines show the curves for the following arbitrary set of parameters' values:  $c_\epsilon = 5.9$ ,  $Pr_n = 0.8$ ,  $\alpha_{Pr} = 4.5$ ,  $r_\infty = 2$ ,  $Pr_\infty = 0.4$ ,  $S_{min} = 0.05$  and  $Ri_c = 0.2$ .

218 equation for which the wind shear production term and the buoyancy term cannot exceed  
 219 unity to maintain a non-zero TKE dissipation thus a non-zero turbulence (e.g. Zilitinkevich  
 220 et al. (2008)).

The discriminant  $\Delta = A_t^2 - 4B_t$  of Eq. 17 is thus always  $> 0$  and the latter always admits a positive solution for  $q$  thus  $e$  that reads:

$$e = \frac{(-A_t + \sqrt{\Delta})^2}{8} \quad (18)$$

221 *Step 2* The TKE variation due to the transport term  $\mathcal{T}$  is then calculated and added  
 222 to the value found in step 1. The calculation of this term consists in resolving the following  
 223 equation:

$$\frac{\partial e}{\partial t} = \frac{1}{\rho} \frac{\partial}{\partial z} \left( \rho K_e \frac{\partial e}{\partial z} \right) \quad (19)$$

224 With an *a priori* knowledge of  $K_e$  - namely an explicit value of  $K_e$  calculated with the  $e$   
 225 value from Step 1 - Eq 19 is a typical diffusion equation that is solved implicitly in time  
 226 through a tri-diagonal matrix inversion (Dufresne & Ghattas, 2009).

### 227 **2.3 Heuristic expressions for the stability functions and turbulent Prandtl** 228 **number**

229 We now have to derive a heuristic expression for the stability function  $S_m$  of the  
 230 gradient Richardson number  $Ri = N^2/S^2$  to be used in the formulation of the diffusion  
 231 coefficient for momentum. On one hand,  $S_m$  should increase when an atmospheric layer  
 232 locally becomes more unstable and thus with decreasing negative  $Ri$ . On another hand, we  
 233 want to prevent  $S_m$  from reaching infinite value when  $Ri \rightarrow -\infty$  to avoid risk of numerical  
 234 instabilities when  $K_m \rightarrow \infty$  (Lenderink & Holtslag, 2000). It is worth recalling here that

235 in unstable conditions, turbulent transport becomes non-local and another type of param-  
 236 etrization such as a mass-flux scheme should come in support of the K-diffusion. In stable  
 237 conditions as turbulent mixing intensity decreases with increasing stability, we assume a  
 238 simple linear decrease with  $Ri$  down to a minimum value attained when the Richardson  
 239 number equals a critical value (Mellor & Yamada, 1974).

Following Lenderink and Holtslag (2004), we propose the following expression for  $S_m$   
 plotted in Figure 1a:

$$S_m(Ri) = \begin{cases} c_n + \frac{2}{\pi}(c_\infty - c_n) \arctan\left(\frac{-Ri}{Ri_0}\right) & \text{if } Ri < 0 \\ \max\left(c_n\left(1 - \frac{Ri}{Ri_c}\right), S_{min}\right) & \text{if } Ri \geq 0 \end{cases} \quad (20)$$

240  $c_n$  is the value of  $S_m$  at  $Ri = 0$  and  $c_\infty$  is the  $S_m$  value in the convective limit.  
 241  $r_\infty = c_\infty/c_n$  is comprised between 1.2 and 5 (Mellor & Yamada, 1982; Lenderink & Holtslag,  
 242 2004).  $Ri_c$  is a critical Richardson number whose inverse value controls the slope of  $S_m$  in  
 243 stable conditions. Previous literature suggests  $Ri_c$  values comprised between 0.19 and 0.25  
 244 (Mellor & Yamada, 1974, 1982; He et al., 2019). As the turbulence vertical anisotropy does  
 245 not reach 0 in very stable conditions (Zilitinkevich et al., 2007; Li et al., 2016),  $S_m$  must be  
 246 lower-bounded by a value  $S_{min}$  which is roughly around 0.05 and that we will make vary  
 247 between 0.025 and 0.1.

The continuity in slope for  $Ri = 0$  further gives:

$$Ri_0 = \frac{2}{\pi}(c_\infty - c_n) \frac{Ri_c}{c_n} \quad (21)$$

Furthermore, the so-called local-scaling similarity theory in stable boundary layers (Nieuwtsadt,  
 1984; Derbyshire, 1990; van de Wiel et al., 2010) implies that in stationary conditions, tur-  
 bulent fluxes and vertical gradient wind speed must scale such that  $\frac{K_m}{lS^2}$  converges towards  
 1 in the neutral limit. This conditions leads to a direct relationship between  $c_n$  and the  
 coefficient  $c_\epsilon$  (Baas et al., 2018; He et al., 2019), the latter being the ratio between the  
 mixing length  $l$  and the TKE dissipation length scale (Sect. 2.2.1):

$$c_n = c_\epsilon^{-1/3} \quad (22)$$

248 The stability function for the heat flux  $S_h$  is estimated through a parametrization of the  
 249 turbulent Prandtl number  $Pr$ . Under unstable conditions, the dominant coherent structures  
 250 such as rising plumes and thermals have vertical velocity anomalies which generally better  
 251 correlate with buoyancy and temperature anomalies than momentum anomalies in average.  
 252 Therefore, one expects  $Pr$  to decrease with increasing instability (Li, 2019). In stably  
 253 stratified conditions, buoyancy is expected to suppress the transport of heat but the existence  
 254 of gravity waves can maintain some transport of momentum inducing an increase in  $Pr$  with  
 255 increasing stability. Collection of field experiments, laboratory data and LES and DNS  
 256 results shows a consistent increase in  $Pr$  with  $Ri$  with a asymptotical linear behaviour at  
 257 strong stability (Zilitinkevich et al., 2008; Li, 2019). We therefore propose the following  
 258 expression of  $Pr$  that is plotted in Figure 1b:

$$Pr(Ri) = \begin{cases} Pr_n - \frac{2}{\pi}(Pr_\infty - Pr_n) \arctan\left(\frac{-Ri}{Ri_1}\right) & \text{if } Ri < 0 \\ Pr_n e^{\frac{1-\alpha_{Pr}}{Pr_n} Ri} + \alpha_{Pr} Ri & \text{if } Ri \geq 0 \end{cases} \quad (23)$$

The formulation in stable conditions is inspired from Venayagamoorthy and Stretch  
 (2010) and it shows fair agreement with experimental data (Li, 2019).  $\alpha_{Pr}$  is the slope of  
 the asymptotical linear trend at high stability and its value ranges from 3 to 5 (Grisogono,  
 2010).  $Pr_n$  is the neutral value of Prandtl number which from extensive laboratory and field

experiments as well as theoretical works range from 0.7 to 1 (Grisogono, 2010; Li, 2019). The continuity in slope at  $Ri = 0$  gives

$$Ri_1 = \frac{2}{\pi}(Pr_\infty - Pr_n) \quad (24)$$

259  $Pr_\infty$  is the value of  $Pr$  in the convective limit and its value roughly ranges between 0.3 and  
260 0.5 (Li, 2019).

## 261 **2.4 Vertical turbulent mixing length formulation**

In near-neutral conditions, we choose a turbulent vertical length-scale formulation  $l_n$  similar to Blackadar (1962) in which the displacement of eddies is limited by the distance to the ground in the neutral limit:

$$l_n = \frac{\kappa z l_\infty}{\kappa z + l_\infty} \quad (25)$$

262 where  $\kappa$  is the Von Kármán constant.  $l_\infty$  is the mixing-length far above the ground whose  
263 value in near-neutral conditions is generally estimated between 15 and 75 m (Sun, 2011;  
264 Lenderink & Holtslag, 2004) In stable conditions, the vertical displacement of eddies -  
265 whose size is roughly above the so-called Ozmidov scale - is limited by the stratification of  
266 the flow (e.g. van de Wiel et al. (2008)). André et al. (1978) and Deardoff (1980) introduced  
267 a widely used buoyancy length-scale which depends on the flow stratification characterised  
268 by Brunt-Väisälä pulsation  $N$ . The mixing length in stable conditions  $l_s$  then read :

$$l_s = c_l \frac{\sqrt{e}}{N} \quad (26)$$

269  $c_l$  being a scalar whose value varies between 0.1 and 2 (Deardoff, 1980; Nieuwtsadt,  
270 1984; Grisogono & Belušić, 2008; Baas et al., 2018).

271 More recent studies introduced wind-shear dependent formulation of  $l_s$  to account  
272 for the deformation of eddies - whose size is above a so-called Corrsin scale - by vertical  
273 wind shear (e.g. Grisogono and Belušić (2008); Grisogono (2010); Rodier et al. (2017)).  
274 Grisogono and Belušić (2008) proposed a mixing-length formulation including both the  
275 effect of stratification and vertical wind shear  $S^2$  that reads:

$$l_s = c_l \frac{\sqrt{e}}{2\sqrt{S^2}(1 + \sqrt{Ri}/2)} \quad (27)$$

The final mixing-length  $l$ , being either ground-limited or stratification-limited is the minimum between  $l_n$  and  $l_s$ . In the model implementation, we choose a commonly-used continuous interpolation formulation:

$$l = \left( \frac{1}{l_n^\delta} + \frac{1}{l_s^\delta} \right)^{-1/\delta} \quad (28)$$

276  $\delta = 1$  by default. The two expressions of  $l_s$  can be used independently in the param-  
277 eterization but unless otherwise stated, the results presented in the rest of the paper have  
278 been obtained with formulation dependent on both stratification and wind shear (Eq. 27).  
279 In practice,  $l$  is also lower bounded by a value  $l_{min} = 1$  cm to prevent it from reaching value  
280 below the Kolmogorov length scale in planetary atmospheric motions (Chen et al., 2016).  
281 As  $l_s$  depends on the TKE, in practice  $l$  is calculated with an explicit value of the TKE i.e.  
282 the value at the beginning of the time-step.

283

## 2.5 Surface layer scheme matching

284

285

286

Neglecting the vertical diffusion term of TKE  $\mathcal{T}$ , Eq. 7 in stationary conditions ( $\partial_t e = 0$ ) can be re-arranged to give a first-order turbulent closure like expressions of the eddy diffusion coefficients for momentum and heat (Cuxart et al., 2006):

$$K_m = l^2 \sqrt{S^2} F_m(Ri) \quad (29)$$

$$K_h = l^2 \sqrt{S^2} F_h(Ri) \quad (30)$$

where

$$F_m(Ri) = S_m^{3/2} \sqrt{c_\epsilon} \left(1 - \frac{Ri}{Pr}\right)^{1/2} \quad (31)$$

$$F_h(Ri) = S_m^{7/4} Pr^{-1} \sqrt{c_\epsilon} \left(1 - \frac{Ri}{Pr}\right)^{1/2} \quad (32)$$

are first-order like stability functions. Near the ground in the surface layer,  $l \approx \kappa z$  and England and McNider (1995) then show that  $F_{m,h}$  functions are identical to the stability functions involved in the bulk expressions of the surface drag coefficients used to calculate surface fluxes of momentum and heat in models :

$$C_{m,h} = \frac{\kappa^2}{\log(z/z_{0m}) \log(z/z_{0m,h})} F_{m,h} \quad (33)$$

287

288

289

290

291

with  $z_{0m}$  and  $z_{0h}$  the surface roughness lengths for momentum and heat respectively. Provided turbulence in the surface layer can be assumed to be close to a stationary state, using the same formulations for  $S_m$  and  $Pr$  in both the turbulent diffusion and surface layer schemes leads to a fully consistent formulation of turbulent fluxes from the surface layer up to the top of the boundary-layer.

292

## 2.6 Degrees of freedom of the scheme and adjustable parameters

293

294

295

296

297

298

299

300

Table 1 summarises all the 10 adjustable parameters of the new parameterization and their ranges of acceptable values as previously introduced in the text. The 8 first parameters in bold are those affecting the simulation of the neutral and stable boundary layers and taken into account in the tuning phase in the next section. It is worth mentioning that we also lower-bound the turbulent diffusion coefficients with the kinematic molecular viscosity and conductivity of the air, which are not tuning parameters per se but pressure and temperature dependent - thus planet dependent - quantities.

300

## 3 Implementation in General Circulation Models, evaluation and tuning

301

### 3.1 Implementation in the LMDZ GCM and Mars Planetary Climate Model

302

303

304

305

306

307

308

309

310

311

312

313

314

The ATKE parameterization has been implemented in the LMDZ Earth GCM (Hourdin et al., 2020; Cheruy et al., 2020), atmospheric component of the French IPSL Coupled-Model (Boucher et al., 2020) involved in the Coupled Model Intercomparison Project (CMIP) exercises. The turbulent-mixing parameterization of LMDZ has received a lot of attention in the past two decades, particularly regarding the convective boundary layer and the very stable boundary layer. It is a hybrid scheme in the sense that turbulent fluxes are expressed as a sum of a K-diffusion term - from the TKE-1 scheme of Yamada (1983) and revisited in Hourdin et al. (2002) and Vignon, Hourdin, et al. (2017) - and a non-local transport term by convective plumes (Rio et al., 2010; Hourdin et al., 2019). Despite those efforts, recent tests revealed that the latest version of the model - the CMIP6 version - still exhibits numerical instabilities in near-neutral boundary layers in presence of strong wind shear. As a proof of concept, the ATKE scheme has also been implemented in the Mars Planetary Climate Model (Mars PCM, Forget et al. (1999)). This model also uses a hybrid scheme

**Table 1.** Name, definition and range of acceptable values for the adjustable parameters. Parameters are dimensionless exception  $l_\infty$  which is a length in m. Parameters in bold are those which affect the simulation of the neutral and stable boundary layer.

Name	Definition	Range
$c_\epsilon$	controls the value of the dissipation length scale	[1.2 - 10]
$c_e$	controls the value of the diffusion coefficient of TKE	[1 - 5]
$l_\infty$	asymptotic mixing length far from the ground	[15 - 75]
$c_l$	controls the value of the mixing length in stratified conditions	[0.1 - 2]
<b><math>Ri_c</math></b>	critical Richardson number controlling the slope of $S_m$ in stable conditions	[0.19 - 0.25]
<b><math>S_{min}</math></b>	minimum value of $S_m$ in very stable conditions	[0.025 - 0.1]
<b><math>Pr_n</math></b>	neutral value of the Prandtl number	[0.7 - 1]
$\alpha_{Pr}$	linear slope of $Pr$ with $Ri$ in the very stable regime	[3 - 5]
$r_\infty$	ratio between $c_\infty$ and $c_n$ controlling the convective limit of $S_m$	[1.2 - 5.0]
$Pr_\infty$	value of $Pr$ in the convective limit	[0.3 - 0.5]

315 with a TKE-1 diffusion scheme inspired from Yamada (1983) and a dry parameterization of  
 316 convective plumes (Colaïtis et al., 2013). Colaïtis et al. (2013) have pointed out that the  
 317 default TKE-1 scheme of Hourdin et al. (2002) leads to numerical oscillations in strongly  
 318 stratified Martian nighttime conditions. They addressed this issue by imposing a mini-  
 319 mum mixing coefficient  $K_{min}$  whose value depends on the boundary layer height following  
 320 Holtslag and Boville (1993).

## 321 **3.2 Parametric sensitivity of the ATKE scheme and tuning**

### 322 **3.2.1 Initial test on the GABLS1 case and parametric sensitivity**

323 The ATKE scheme is first tested on single column simulations using the 1D version of  
 324 LMDZ with a 95-level vertical grid introduced in Hourdin et al. (2019). We run 1D simu-  
 325 lations on the GEWEX Atmospheric Boundary Layer Study 1 (GABLS1) single column model  
 326 intercomparison exercise. The latter consists in a no-radiation idealized 9 hour simulation of  
 327 the development of a weakly stable boundary layer, with a constant zonal geostrophic wind  
 328 of  $8 \text{ m s}^{-1}$  and a constant surface cooling of  $-0.25 \text{ K h}^{-1}$  (Cuxart et al., 2006). The fair  
 329 convergence of 3D LES on this case - with the exact same initial and boundary conditions as  
 330 those for single column models - make LES suitable references for GABLS1. Nonetheless, to  
 331 sample the small variability between LES runs, we consider hereafter 5 reference LES which  
 332 correspond to the MO-1m, MO-2m, UIB-2m, IMUK-1m, IMUK-2m simulations listed in  
 333 Table 2 of Beare et al. (2006), the suffix referring to the vertical resolution.

334 Given the ranges of acceptable values associated with each of the  $n = 8$  free param-  
 335 eters affecting the simulation of the stable boundary layer listed in Table 1, we need to  
 336 run simulations with different sets of parameters to assess the parametric sensitivity of the  
 337 scheme. For this purpose, we use the HighTune explorer statistical tool originally developed  
 338 in the Uncertainty Quantification community and now applicable in atmospheric modeling  
 339 (Couvreur et al., 2021). This tool allows to make a first perturbed physics ensemble exper-  
 340 iment through an exploration of the initial  $n$ -dimension hypercube of parameters defined  
 341 by the intervals given in Table 1 using a Latin Hyper Cube sampling method. Here 80  
 342 (10 times  $n$ ) sets of parameters or free parameters' vectors are sampled. Unless otherwise  
 343 stated, the simulations are run with a 15 min time step, i.e. the typical value used for the  
 344 LMDZ physics and that used for the ensemble of CMIP6 simulations.

345 Figure 2 shows the results of this *a priori* sensitivity analysis to free parameters' values  
 346 for the vertical profiles of potential temperature, wind speed and TKE averaged over the

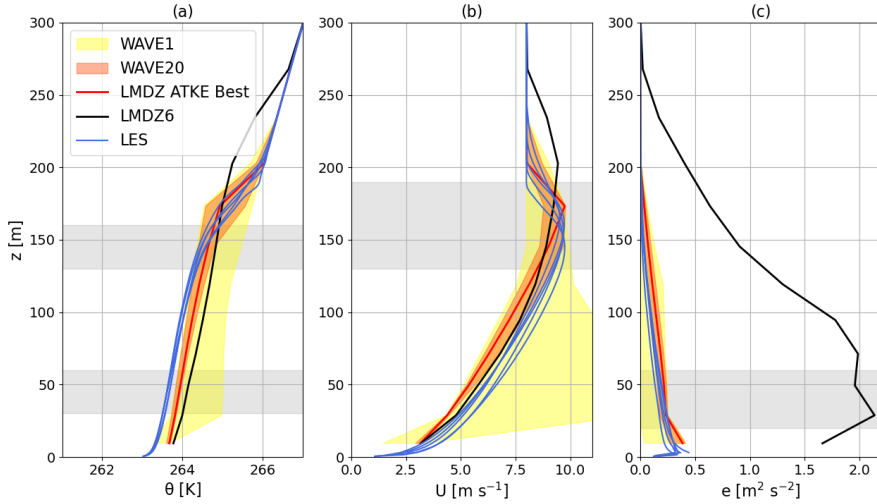


**Figure 2.** Evolution of envelopes of the vertical profiles of potential temperature (panel a), wind speed (panel b) and TKE (panel c) after 9 hours of GABLS1 simulation. Yellow and orange envelopes correspond to waves 1 and 20 respectively i.e. to the 1st and 20th set of 80 simulations during the tuning exercise. Blue curves show the 5 reference LES. The red curve shows the ‘best’ LMDZ simulation. The black curve shows the CMIP6 version of LMDZ for comparison. The horizontal light grey band show the vertical ranges over which the metrics are calculated for each variable. In panel c, note that the full (resolved+subgrid) TKE from the LES is shown.

347 eighth hour of the simulation. The yellow envelope displays the variability (minimum and  
 348 maximum values) amongst the 80 simulations from this first so-called ‘wave’ of simulations.  
 349 Albeit encompassing the five reference LES coming from the GABLS1 LES intercomparison  
 350 exercise (Beare et al., 2006), this yellow envelope highlights the large range of vertical  
 351 profiles obtained. This is a signature of the high sensitivity of the results to the parameters as  
 352 they are varied across the range given in Table 1. In particular, very strong and unrealistic  
 353 momentum decoupling manifesting as very strong wind speed gradient near the surface is  
 354 allowed by the scheme in regions of the parameter space where the negative feedback of  
 355 the wind shear on the mixing length (Eq. 27) is overappreciated. Interestingly, Figure 3b  
 356 shows that such a decoupling is never simulated when using the buoyancy-only dependent  
 357 length scale (Eq. 26). However, even if the yellow envelop is reasonable for the potential  
 358 temperature and wind speed (Figure 3a,b), the use of the buoyancy-only dependent length  
 359 scale can lead to unrealistically strong values of TKE in the middle of the boundary layer  
 360 (Figure 3c) owing to overly high mixing length values.

361 Overall, the large width of the yellow envelope in Figure 2 and the possible large discrep-  
 362 ancy with respect to the LES call for a reduction of the parameter space and a calibration  
 363 of the ATKE scheme.  
 364

### 365 **3.2.2 History matching with iterative refocusing**

366 For this purpose, we follow a history matching with iterative refocusing procedure  
 367 which in practice is performed with HighTune explorer. This procedure is made of 6 steps  
 368 and is fully described in Couvreur et al. (2021) and Hourdin et al. (2021). We refer the

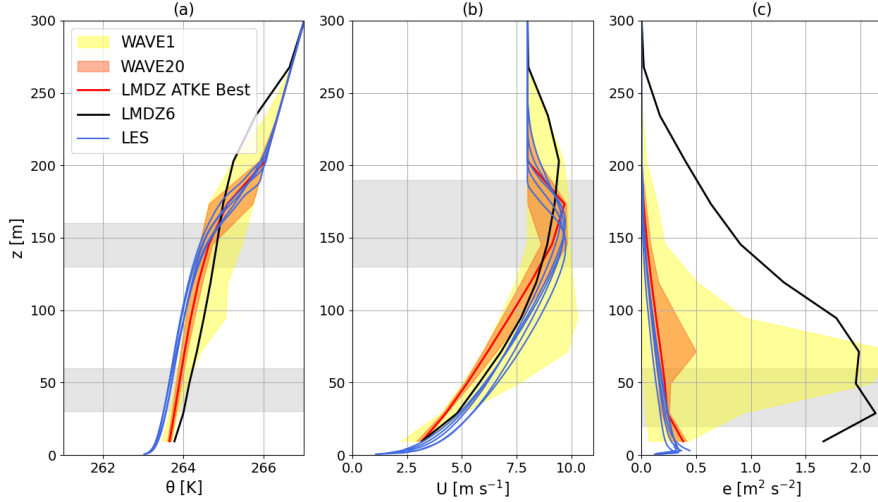


**Figure 3.** Same as Figure 2 but for simulations using the buoyancy length-scale formulation (Eq. 26) instead of the stratification and wind-shear dependent formulation (Eq. 27) in stable conditions.

369 reader to the aforementioned papers for details on the method and describe here the main  
 370 steps for our application.

371 *Step 1* We first define 5 metrics, i.e. targets for the model with respect to the LES  
 372 reference, to properly capture the boundary layer structure. Those metrics are the potential  
 373 temperature at the bottom (average between 30 and 60 m) and top (average between 130  
 374 and 160 m) part of the boundary layer, the zonal wind speed at the low-level jet height  
 375 (average between 130 and 190 m) and the TKE at the bottom (average between 20 and 60  
 376 m) and middle (average between 60 and 100 m) part of the boundary layer. All metrics are  
 377 calculated on hourly-mean profiles between the 8th and 9th hour of the simulation, when  
 378 the stable boundary layer is well developed.

379 *Step 2* We then define the initial parameter space consisting in a 8-dimension space  
 380 corresponding to the 8 parameters in bold in Figure 1 and their associated range of possible  
 381 values.

382 *Step 3* This parameter space is then sampled 80 times and experimented on GABLS1  
 383 simulation as in Sect. 3.2.1.

384 *Step 4* Based on those 80 simulations, an emulator is built for each metric based on  
 385 a Gaussian Process providing values for the expectation and variance at any location in the  
 386 parameter space.

*Step 5* We then compare the simulated metrics with respect to those from the LES  
 reference through the calculation of an implausibility  $I$  for each metrics at each point  $\lambda$  of  
 the parameter space:

$$I(\lambda) = \frac{|r - E[e_m(\lambda)]|}{\sqrt{\sigma_r^2 + \sigma_d^2 + \text{Var}(e_m(\lambda))}} \quad (34)$$

387 where the numerator is the absolute difference between the reference metrics  $r$  and the  
 388 corresponding expectation from the emulator  $E[e_m(\lambda)]$ ; and the denominator is the stan-  
 389 dard deviation of this difference, which includes the reference uncertainty (i.e. the spread

390 between LES  $\sigma_r^2$ ), the uncertainty associated to the emulator ( $Var(e_m(\lambda))$ ), and model struc-  
 391 tural uncertainty ( $\sigma_d^2$ , see Couvreur et al. (2021) for details). As the latter is not a priori  
 392 known, one has to prescribe an arbitrary ‘tolerance to error’ (see thorough discussion on the  
 393 rationale behind this tolerance in Hourdin et al. (2021)) that we set to 0.25 K for potential  
 394 temperature,  $0.25 \text{ m s}^{-1}$  for wind speed and  $0.01 \text{ m}^2 \text{ s}^{-2}$  for TKE. History matching then  
 395 rules out a part of the parameter space that corresponds to unacceptable model behaviour  
 396 - i.e. with an implausibility higher than a given cut-off value of 3 - and keeps a not-ruled  
 397 out yet (NROY) space.

398 *Step 6* Iterative refocusing then consists in sampling 80 new free parameter vectors  
 399 in the NROY space and reiterates over several tuning ‘waves’ from step 4 to 6.

400 Note that this procedure is not an optimization method providing in the end a single  
 401 set of parameters, but a method ruling-out a non-plausible part of the initial parameter  
 402 space and giving the space of acceptable free parameters - given the chosen metrics and  
 403 tolerances - once it has converged.

404 The results after 20 waves of tuning are shown with orange envelopes for the potential  
 405 temperature, wind speed and TKE profiles in Figure 2. Compared to the initial and first  
 406 wave (yellow envelopes), one can first notice the convergence towards LES curves. Consider-  
 407 able improvement is obtained with respect to the CMIP6 version of LMDZ, with a shallower  
 408 and more realistic - compared to LES - boundary-layer height, a more peaked low-level jet  
 409 and lower and much closer-to-LES TKE values. Nonetheless, the potential temperature  
 410 (resp. wind speed) in the first tens of meters above the surface remains slightly overesti-  
 411 mated (resp. underestimated). Such biases can be reduced by adding metrics targeting the  
 412 lowermost part of the profiles and increasing the vertical resolution close to the surface (not  
 413 shown).  
 414

415 We now examine the 10 ‘best’ simulations obtained during the tuning exercise. The  
 416 adjective ‘best’ is employed here as in Hourdin et al. (2021) in the sense that the maximum  
 417 (across metrics) value of the ratio of the distance to LES divided by the tolerance to error  
 418 is the smallest at the end of the tuning exercise. Note that this choice of 10 simulations and  
 419 the denomination ‘best’ goes beyond the history matching philosophy as there is *a priori*  
 420 no reason to prefer specific configurations than others in the final NROY spaces given the  
 421 chosen metrics and tolerances. A choice is done here to illustrate the behaviour of the ATKE  
 422 scheme for single sets of parameters obtained at the end of the tuning process in 1D and  
 423 3D simulations.

424 Figure 4a,c) show that they reproduce fairly well the profiles of heat and momentum  
 425 turbulent fluxes, i.e. two quantities that were not directly targeted during the tuning.  $K_{m,h}$   
 426 values are also much lower than those in the CMIP6 physics simulation (Figure 4b,d) which  
 427 concurs with conclusions regarding the profiles of TKE in Figure 2c. In addition, Figure  
 428 5 reveals the good numerical stability and convergence properties of the TKE in these  
 429 simulations, as well as the considerable improvement regarding these aspects with respect  
 430 to the CMIP6 version of the LMDZ physics. This makes us confident with the robustness and  
 431 efficiency and the numerical resolution method for the TKE evolution equation presented  
 432 in 2.2.2.

433 When inspecting more deeply the NROY space after 20 waves of tuning (Figure 6),  
 434 one can notice that its final shape has been mostly constrained by the  $c_l$  and  $c_\epsilon$ , and to a  
 435 lesser extent by  $l_\infty$ . This does not absolutely mean that the other 5 parameters do not play  
 436 role in the overall behaviour of the scheme but this shows that the representation of the  
 437 GABLS1 weakly stable boundary layer with ATKE mostly depends upon the value of  $c_l$ ,  $c_\epsilon$   
 438 and  $l_\infty$ . This point is further shown by the strong similarity between Figure 7 - which has  
 439 been produced with a tuning on  $c_l$ ,  $c_\epsilon$  and  $l_\infty$  only - and Figure 2. Such a result is not that  
 440 surprising since the turbulent diffusion in weakly stable boundary layer mostly results from

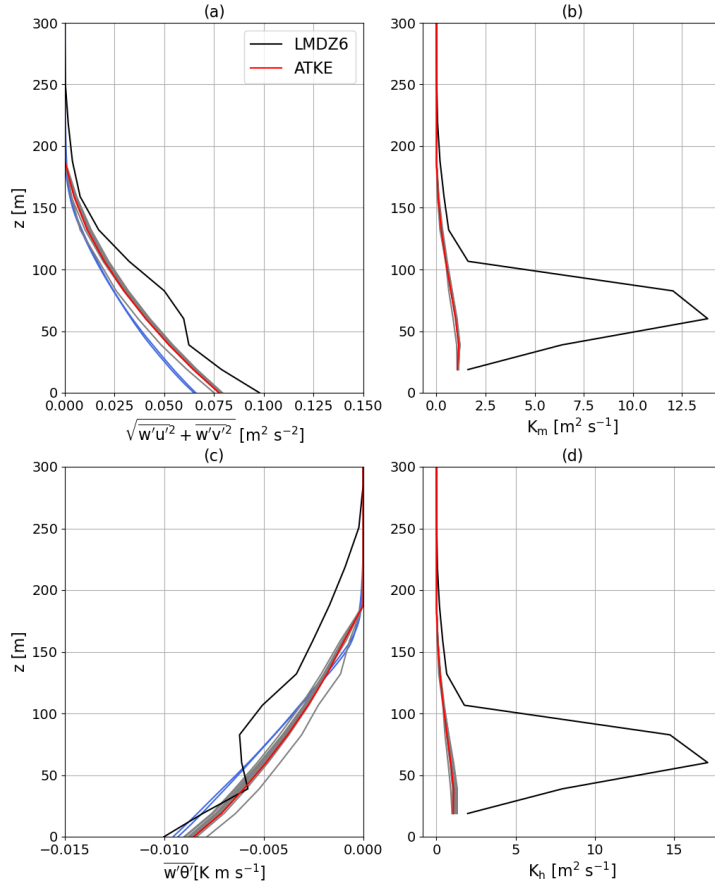


**Figure 4.** Vertical profiles of momentum flux (panel a), heat flux (panel c), eddy diffusivity coefficient for momentum (panel b) and heat (panel d) after 9 hours of GABLS1 simulation. Grey curves show the LMDZ simulations run with the 10 best parameter vectors after the tuning exercise. Blue curves in panels a and c show the 5 reference LES. The red curve shows the ‘best’ LMDZ simulation obtained during the tuning exercise (see main text for details). The black curve shows the CMIP6 version of LMDZ for comparison.

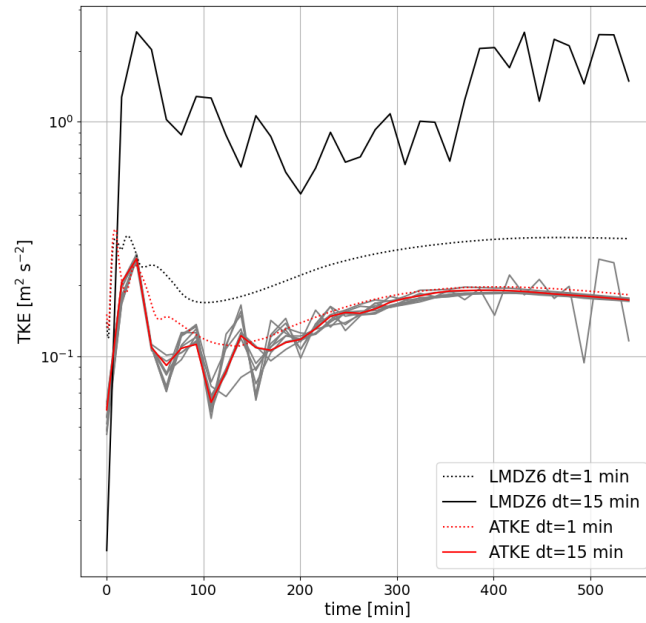


**Figure 5.** Time evolution of the TKE at 40 m a.g.l. in LMDZ single column model GABLS1 simulations. Solid grey curves show the simulations run with the 10 best parameter vectors after the tuning exercise and a 15 min time step. The solid and dotted red curves shows simulations run with the best parameter vector and a time step of 15 and 1 min respectively. The solid and dotted black curves shows simulations run with CMIP6 version of LMDZ and a time step of 15 and 1 min respectively.

441 eddies whose size and energy are controlled by wind shear intensity and TKE dissipation.  
 442 In addition, the weak dependence upon  $c_e$  may have somewhat been expected given the  
 443 relatively weak contribution of the transport term  $\mathcal{T}$  is the overall TKE budget (not shown).  
 444 Regarding  $S_{min}$ ,  $Ri_c$  and  $\alpha_{Pr}$ , one may expect a more important role of those parameters in  
 445 very stable boundary layers i.e. with a stratification more pronounced compared to that in  
 446 GABLS1. Their values might thus be more constrained if we were to tune the ATKE scheme  
 447 over a more stable boundary layer case such as GABLS4 (Couvreur et al., 2020) instead  
 448 of or in addition to GABLS1. However LES do not converge that well on GABLS4 which  
 449 makes the tuning exercise more delicate. Moreover, the role of radiation in determining  
 450 the structure of the boundary-layer becomes increasingly important as stability increases  
 451 (Edwards, 2009) and in addition to turbulent diffusion, the coupling between turbulence  
 452 and radiation becomes an essential feature to capture with models. We therefore leave this  
 453 aspect for further research.

### 454 3.3 Challenging the Antarctic and Martian stable boundary layers

455 We now conduct two short and arbitrary applications of the ATKE parameterization  
 456 in simulations with the LMDZ GCM and Mars PCM.

#### 457 3.3.1 Stable boundary layer regimes at Dome C, Antarctic Plateau

458 First, we verify that the proposed scheme is able to reproduce the dichotomous be-  
 459 haviour of the stable boundary layer at Dome C on the Antarctic Plateau that is, a very  
 460 stable regime with strong temperature surface-based inversions and collapsed turbulence  
 461 versus a weakly stable state with weak inversions. The sharp transition between those 2  
 462 regimes occurs in a narrow range of wind speed (Vignon, van de Wiel, et al., 2017; Baas  
 463 et al., 2019). Such a test was proposed in Vignon et al. (2018) to verify the ability of the  
 464 CMIP6 version of LMDZ to reproduce the overall dynamics of the stable boundary layers  
 465 and it is performed here as capturing the Dome C boundary layer was identified as a *target*  
 466 during the development of LMDZ for CMIP6 (Cheruy et al., 2020). This is an aspect that  
 467 we want to conserve throughout the development of the LMDZ physics and particularly  
 468 when introducing a new turbulent diffusion scheme. It is also worth noting that such a test  
 469 was also used for the recent development of the CanAM model (He et al., 2019) as well  
 470 as for verifying the robustness of LES of the stable boundary layer (van der Linden et al.,  
 471 2019). We follow here the exact same LMDZ simulation configuration as in Vignon et al.  
 472 (2018) that is, one year (2015) simulations are conducted with the zooming capability of  
 473 the LMDZ to refine a  $64 \times 64$  global grid to reach a  $50 \times 50$  km on the Dome C. One slight  
 474 difference though with respect to Vignon et al. (2018) is that we use the 95-level vertical grid  
 475 used in the previous section instead of the 79-level grid in the reference paper. Nudging in  
 476 wind, temperature and humidity towards ERA5 reanalyses (Hersbach et al., 2020) is applied  
 477 outside the zoom area to evaluate the sub-components of the physics of the model apart  
 478 from likely deficiencies in representing the large scale meteorological fields. The reader is  
 479 referred to Vignon et al. (2018) for details on the simulation configuration as well as the  
 480 surface snow treatment in LMDZ. The simulation has been run with the CMIP6 version of  
 481 the LMDZ physics as well as by an adapted versions using the ATKE diffusion scheme and  
 482 the 10 ‘best’ sets of parameters found from the single column model tuning.

483 A simple diagnostics to assess the representation of the two stable boundary layer  
 484 regimes is to investigate the dependence of the surface-based temperature inversion upon  
 485 the wind speed in clear sky conditions. Data align along a well-defined ‘inverted-S’ shape  
 486 curve (Vignon, van de Wiel, et al., 2017; van de Wiel et al., 2017), the two horizontal  
 487 branches corresponding to the two regimes and the vertical one to the non-linear transition  
 488 between them as the wind speed increases or decreases (Figure 8a). As shown in Figure 8b,  
 489 the CMIP6 version of LMDZ reasonably captures the strong surface-atmosphere decoupling  
 490 in very stable conditions and the 2-regime behaviour. LMDZ with the ATKE scheme run  
 491 with the ‘best’ set of parameters (Figure 8c) retained in Sect. 3.2 reproduces even more

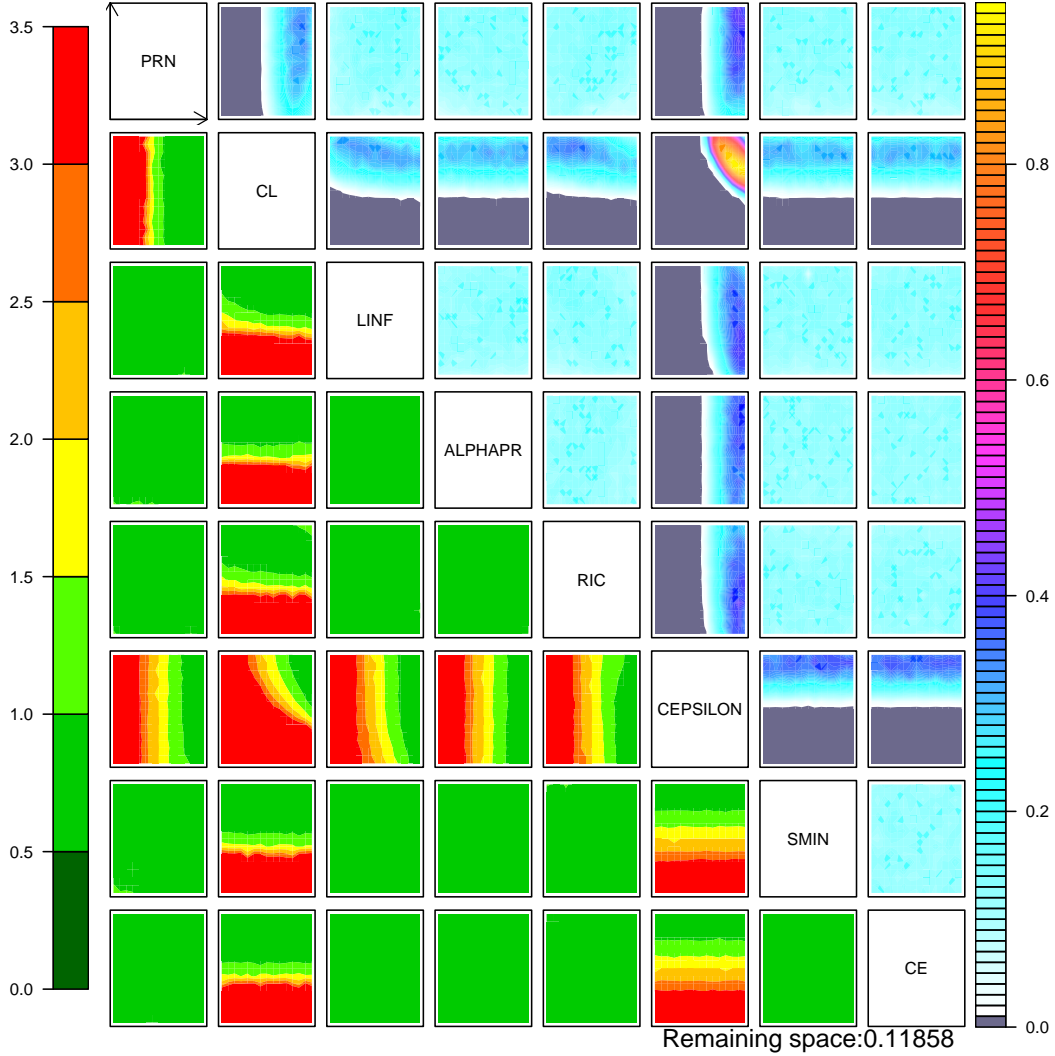


**Figure 6.** Implausibility matrix after 20 waves of history matching exploration. The upper-right triangle is made of sub-matrices that show the fraction of points with implausibility lower than the chosen cutoff while the sub-matrices of the lower-left triangle show the minimum value of the implausibility when all the parameters are varied except those used as x- and y-axis, the name of which are given on the diagonal of the main matrix. The number at the bottom of the graph shows the NROY space value (fraction of the initial parameter space) after 20 waves.

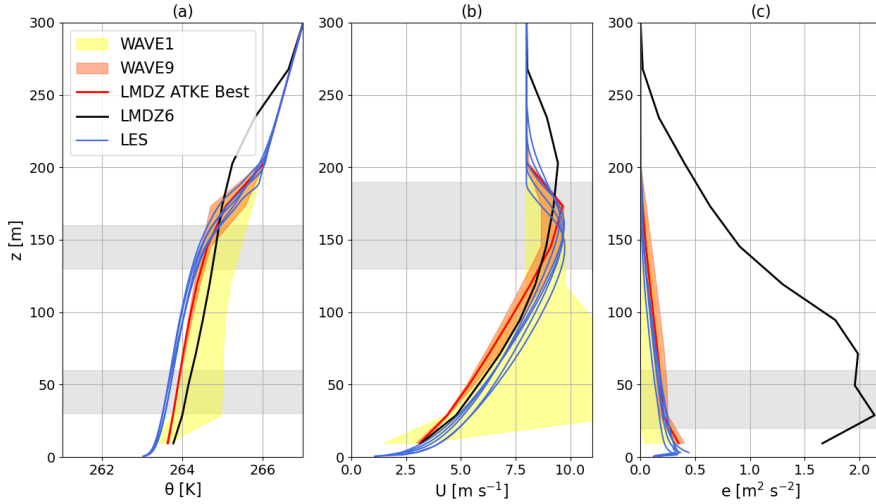


**Figure 7.** Same as Figure 2 but after a tuning on  $c_e$ ,  $c_l$  and  $l_\infty$  only. The other parameters have been arbitrarily set to the following values:  $Ri_c = 0.2$ ,  $S_{min} = 0.05$ ,  $Pr_n = 0.8$ ,  $\alpha_{Pr} = 4.5$  and  $c_e = 2.0$ . Note that we have stopped the tuning exercise at the 9th wave here since convergence has been attained.

492 realistically reproduce the 2-regime behaviour - that is, the reversed ‘S’ shape pattern - and  
 493 the decoupling in very stable conditions despite an overestimation of the strong temperature  
 494 inversions. The latter can be attributed to an overly weak downward longwave radiative  
 495 flux from the very dry and cold Dome C atmosphere in clear-sky conditions (Vignon et al.,  
 496 2018).

497 An important point here is that such results are obtained with all the 10 ‘best’ sets  
 498 of parameters after 20 waves of tuning on GABLS1 (Figures 8c-l) and despite the fact that  
 499 such a GABLS1-based tuning has not substantially constrained parameters that may be *a*  
 500 *priori* important in very stable conditions such as  $S_{min}$ ,  $Ri_c$  and  $\alpha_{Pr}$ . In fact, the transition  
 501 between the weakly and very stable regimes of the stable boundary-layer primarily relies on  
 502 the ability of a TKE-l scheme to allow for a turbulence collapse in very stable conditions  
 503 (Vignon et al., 2018). This is the case with the ATKE scheme - whatever the  $S_{min}$ ,  $Ri_c$   
 504 and  $\alpha_{Pr}$  value chosen in their corresponding ranges of acceptable values - as no artificial  
 505 threshold or lower-bound has been prescribed to maintain a certain amount of TKE in very  
 506 stable conditions.

### 507 3.3.2 Nocturnal stable boundary layer collapse on Mars

508 Mars has a thinner and much less dense atmosphere compared to Earth and its plan-  
 509 etary boundary layer exhibits stronger diurnal variations (Spiga et al., 2010b; Petrosyan et  
 510 al., 2011) with a abrupt collapse at the day-night transition. During night-time, the Mar-  
 511 tian boundary layer exhibits numerous similarities with that of the polar regions on Earth  
 512 such as strong surface-based temperature inversions associated with very weak turbulence  
 513 (Banfield et al., 2020), the latter being able to re-activate through wind shear production  
 514 associated with low-level jets (Chatain et al., 2021).

515 This extreme environment enables us to challenge the versatility of ATKE param-  
 516 eterization and compare its performance with the default TKE-l scheme used in the current  
 517 Mars PCM (Colaïtis et al., 2013).

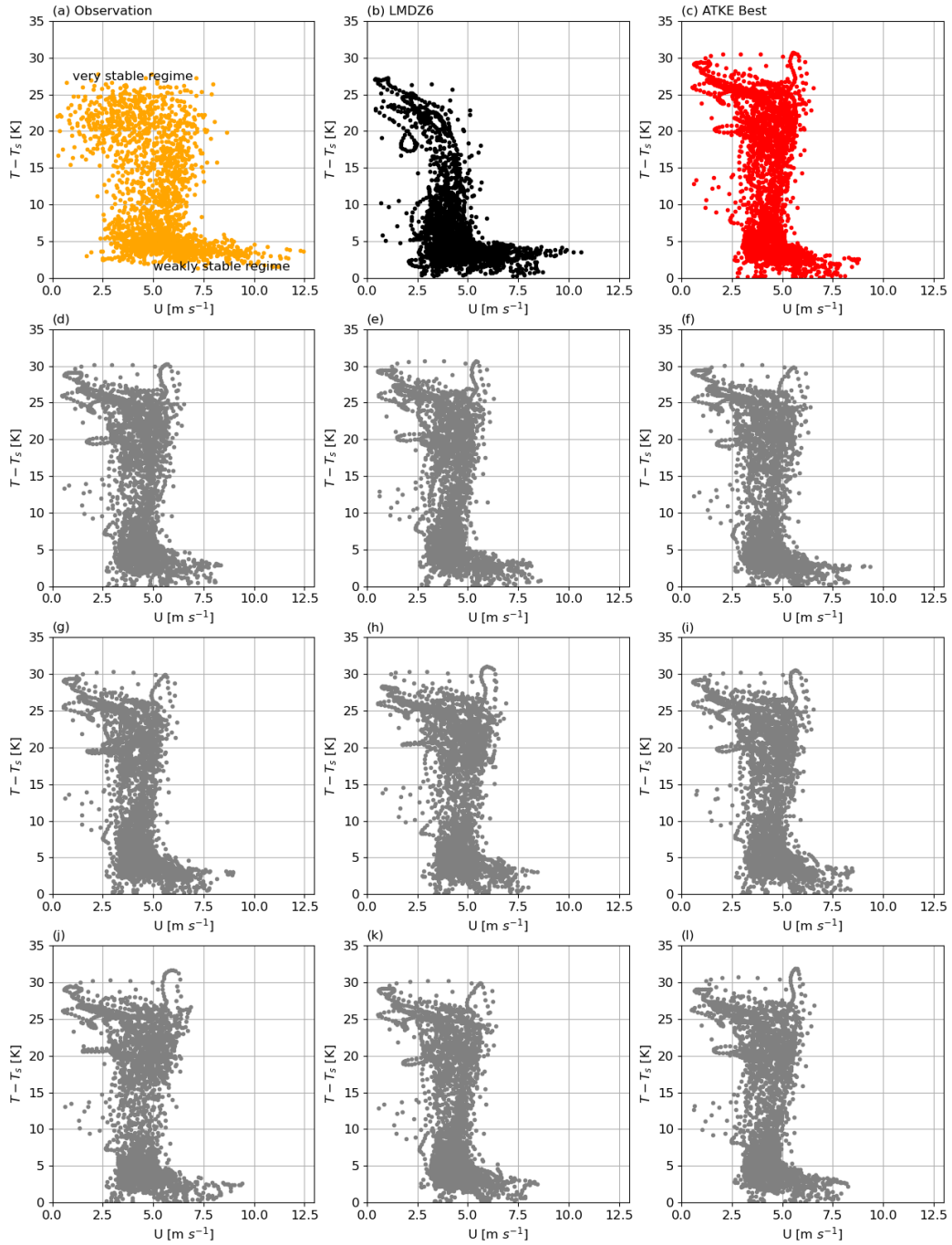


**Figure 8.** Temperature inversion between 10 m and the ground surface plotted as a function of the 10-m wind speed in clear-sky conditions (downward longwave radiative flux  $< 100 \text{ W m}^{-2}$ ) from April to September 2015. Panel a shows results from in situ observations. Panel b (resp. c) show the LMDZ simulation in the CMIP6 physics configuration (resp. with the ATKE scheme using the best set of parameters retained in Sect. 3.2). Panels d to l show results from 9 simulations with the ATKE scheme using 9 following ‘best’ sets of parameters after the tuning phase on GABLS1. Dome C measurement data are from Genthon et al. (2021).

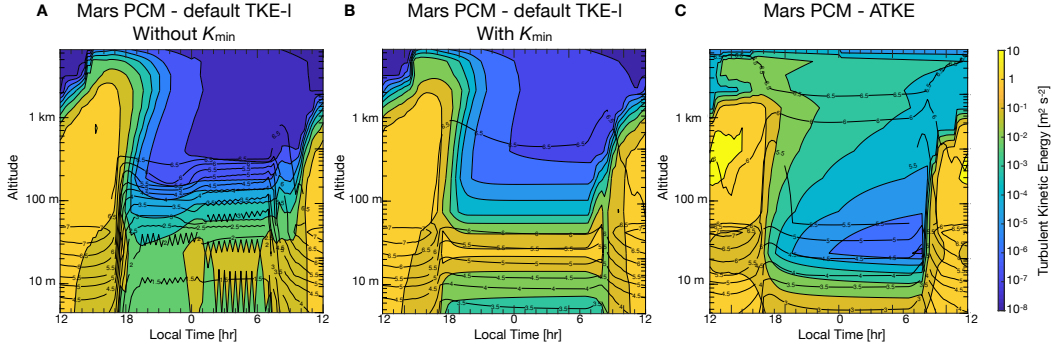


**Figure 9.** Evolution of the TKE through the Martian day in a) the baseline physics configuration; b) the same configuration with no minimum mixing coefficient  $K_{min}$ ; c) the simulation using the ATKE scheme for turbulent diffusion. Black contours indicate the wind speed in  $\text{m s}^{-1}$ .

518 As a first test, we compare the two parameterizations using the single-column version  
 519 of the Mars PCM to assess the overall behaviour of the diurnal cycle of the boundary  
 520 layer and the numerical stability of the model. The single-column version of the Mars  
 521 PCM uses the same physics as the 3D model (Lange et al., 2023) and a vertical grid with  
 522 6 levels in the first km above the ground. No lateral advection of heat and momentum  
 523 is prescribed, the initial temperature profile is set to 180 K and the zonal wind speed is  
 524 nudged towards a constant value of  $7 \text{ m s}^{-1}$  which corresponds to values measured at the  
 525 Mars Equator by the InSight lander (Banfield et al., 2020). Simulations are performed at  
 526 the Equator, with no dust aerosols, and ran for several Martian days until the diurnal cycle  
 527 reaches an equilibrium after 10 days. The nocturnal boundary layer simulated is weakly  
 528 to moderately stable, with a near-surface gradient Richardson not exceeding 0.1. Figure  
 529 9 shows the evolution of the TKE (colour shading) and wind speed (contours) in the first  
 530 km above the ground surface during a typical diurnal cycle. As explained in Sect. 3.1, the  
 531 nocturnal TKE field simulated by the default TKE-I scheme of the Mars PCM is affected  
 532 by strong numerical oscillations (Figure 9a) which are mitigated when adding a minimum  
 533 mixing coefficient  $K_{min}$  (Figure 9b). When using the ATKE scheme with the ‘best’ set of  
 534 parameters retained from the tuning on GABLS1 in Sect. 3.2.2 (Figure 9c) and with no  
 535 prescription of  $K_{min}$ , the structure of the nocturnal boundary layer is well captured and no  
 536 numerical oscillations affect the TKE and wind fields. Unlike in Figure 9b, the TKE exhibits  
 537 a continuous decrease with increasing height in the nocturnal boundary layer, which better  
 538 concurs with the typical TKE structure in weakly stable boundary layers (e.g., (Acevedo et  
 539 al., 2015)).

540 We then assess the performance of the ATKE model by performing simulations with  
 541 the 3D Mars PCM and comparing the results to in situ wind observations collected by the  
 542 InSight lander deployed at a latitude  $4.5^\circ \text{ N}$  and a longitude of  $135^\circ \text{ E}$ . InSight continuously  
 543 monitored the wind at a height of 1.2 m for almost one martian year with an unprecedented  
 544 time resolution (Banfield et al., 2020). Two striking phenomena have been detected. First,  
 545 a dramatic reduction of the wind speed, following the collapse of the boundary layer is  
 546 observed around 17-18 local time during the clear season (Figure 10a) i.e., the first half  
 547 of the Martian year when a relatively small amount of dust is present in the Martian sky  
 548 (Kahre et al., 2017). The abruptness of this change is related to both the very low thermal  
 549 inertia of the Martian ground surface and the thinness of the Martian atmosphere. Second,  
 550 during the dusty season i.e. the second half of the Martian year, substantial night-time  
 551 turbulence is observed (Chatain et al., 2021) and the decrease in near-surface wind speed  
 552 is less pronounced (Figure 10d). Those two phenomena have been shown to be poorly

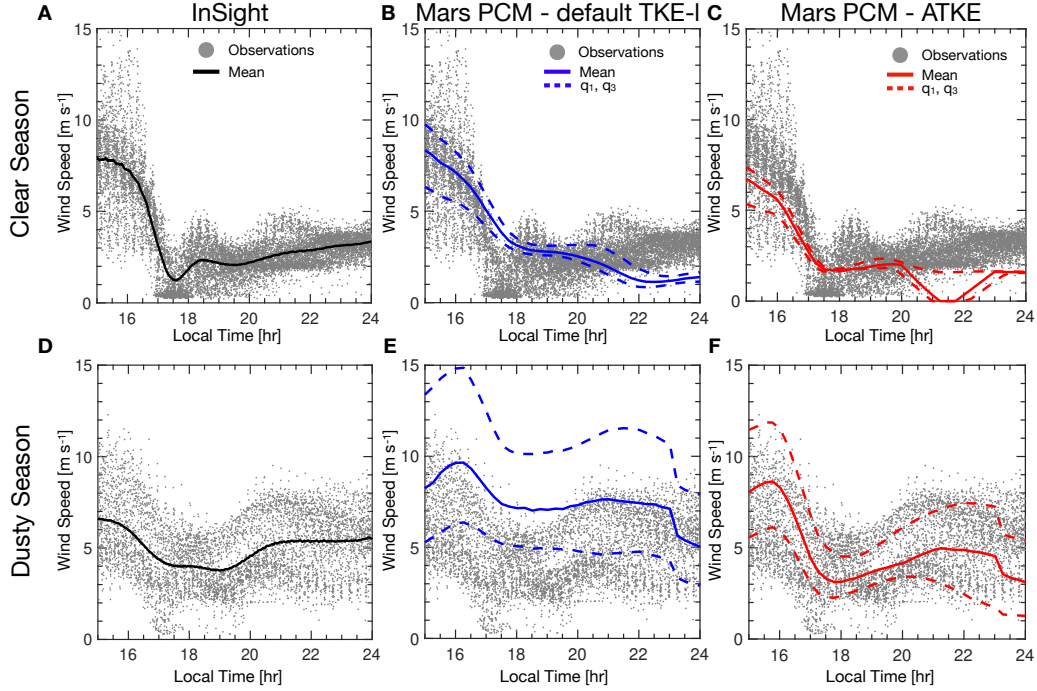


**Figure 10.** Comparison between InSight wind speed measurements (grey dots and black curves in panels a and d ) and Mars PCM simulations using the default TKE-l scheme (b, e) and the ATKE scheme (c, f). For model fields, the mean wind speed over the period considered is presented in solid lines, and the diurnal variability is shown with the envelope of dashed lines ( $q_1$  and  $q_3$  referring to the first and third quartiles).

553 reproduced by the Mars PCM, in particular, the collapse of winds at sunset (Forget et al.,  
554 2021).

555 Here, as a proof of concept, we run the 3D Mars PCM using either the default TKE-l  
556 scheme and the ATKE scheme with the ‘best’ set of parameters from the GABLS1 tuning i.e.  
557 with no specific tuning for Martian conditions. Global simulations are performed over one  
558 complete martian year with a resolution of  $3.75^\circ$  in latitude and  $135.9^\circ$  in longitude. Initial  
559 conditions are derived from 10-year simulations which provide equilibrium states of water  
560 and  $\text{CO}_2$  cycles (Pottier et al., 2017). The seasonal and geographic variations of dust opacity  
561 in the sky are prescribed using dust observations by (Montabone et al., 2015). Results are  
562 presented in Figure 10. Concurring with Forget et al. (2021), the model in its standard  
563 configuration fails to reproduce the sharp transition from high to low wind speeds at sunset  
564 (Figure 10b). This aspect is significantly improved when using the ATKE scheme (Figure  
565 10c). However, the wind speed in the second part of the night remains underestimated in  
566 both configurations which questions the representation of the surface-atmosphere decoupling  
567 in this period (Chatain et al., 2021). In the dusty season, the current model overestimates  
568 the surface wind speed owing to an excess of turbulent mixing (Figure 10e), while the ATKE  
569 parameterization leads to more realistic wind speeds (Figure 10f).

570 Overall, this preliminary experiment demonstrates: i) the applicability of the ATKE  
571 parameterization on Mars and the promising results that can be obtained with a set of  
572 parameters not specifically tuned for Mars conditions and; ii) the improvement of the model  
573 both numerically and physically in stable conditions. Nonetheless, Mars simulations with  
574 the ATKE scheme would further benefit from a more adapted tuning using references such as  
575 Mars LES (Spiga et al., 2010a) or InSight observations (Banfield et al., 2020). It is also worth

576 noting that the Mars atmosphere, particularly at the poles i.e. far from the InSight landing  
 577 site, exhibits particularities that cannot be properly captured with the current version of  
 578 the ATKE scheme. A key aspect is that air buoyancy can be created by compositional  
 579 vertical gradients of both water vapor and carbon dioxide, i.e. the prevailing gas of Mars'  
 580 atmosphere. In particular, during the winter polar night, CO<sub>2</sub> condenses upon the ice cap  
 581 surface (e.g., (Weiss & Ingersoll, 2000)) changing dramatically the near-surface atmospheric  
 582 composition. Such an effect cannot be taken into account given with Brünt-Vaisala pulsation  
 583 and Richardson number expressions based on a virtual potential temperature. This aspect  
 584 deserves attention for further improvement of the ATKE scheme.

## 585 4 Summary and Conclusions

586 This study presents the development of a simple TKE-l parameterization of turbulent  
 587 eddy coefficients for the simulation of the neutral and stable boundary layer in large-scale  
 588 atmospheric models. The parameterization has been carefully designed such that all ad-  
 589 justable parameters have been clearly identified and their ranges of possible values defined  
 590 to help the calibration and assess the parametric sensitivity. Instead of using fixed and  
 591 empirical expressions of stability functions and turbulent Prandtl number, we have derived  
 592 fully tunable and heuristic formulae to improve the versatility of the scheme and its potential  
 593 applicability for planetary atmospheres composed of an ideal and perfect gas. A wind-shear  
 594 and buoyancy dependent formulation for the mixing length in stratified conditions is con-  
 595 sidered. A 2-step numerical treatment of the TKE equation is further proposed and shows  
 596 good convergence and stability properties at typical time steps used in large scale atmo-  
 597 spheric models. The parametric sensitivity of the ATKE scheme has been assessed with  
 598 the HighTune explorer tools using 1D simulations of the GABLS1 weakly stable boundary  
 599 layer case with the single-column version of LMDZ. Using a History-Matching approach,  
 600 we carried out a first calibration of the scheme allowing us to reduce the initial parameter  
 601 space to keep an ensemble that satisfies the representation of weakly stable boundary layer.  
 602 Substantial improvement with respect to the CMIP6 version of LMDZ has been achieved in  
 603 terms of vertical profiles of temperature, wind, TKE and turbulent fluxes of momentum and  
 604 heat, as well as in terms of numerical stability. However this tuning experiment restricted  
 605 to the weakly stable GABLS1 case has not enabled us to clearly evidence a potential added  
 606 value of a wind-shear and buoyancy dependent formulation for the mixing length in strat-  
 607 ified conditions compared to a buoyancy only-dependent one, even if the vertical profile of  
 608 TKE is slightly better captured.

609 The ability of the ATKE scheme to simulate the stable boundary layer as well as its  
 610 applicability to planetary atmospheres have then been assessed through simulations of the  
 611 Antarctic and Martian boundary layer with the LMDZ and Mars Planetary Climate model  
 612 respectively. In particular the 2-regime behaviour of the stable boundary layer at Dome C,  
 613 a challenge for turbulent diffusion schemes in GCMs, is reasonably well captured with the  
 614 ATKE scheme. In addition, promising results have been obtained for the representation of  
 615 the nocturnal Martian boundary layer with improvements regarding the numerical stability  
 616 compared to the original model. Such results pave the way for a Mars-specific tuning of the  
 617 ATKE scheme in the future.

618 A prospect of our work is to verify the physical and numerical robustness of the  
 619 ATKE parameterization in atmospheric flows with extremely strong wind shear such as  
 620 katabatic winds developing over ice caps. Such an application could also make it possible to  
 621 assess a potential added value of a wind shear-dependent formulation of the mixing length.  
 622 Moreover, in view of a fully reliable application in a climate model such as LMDZ, the  
 623 key parameters of the ATKE scheme - especially  $c_l$  and  $c_\epsilon$  - should be included in a more  
 624 thorough tuning exercise including parameters from other parameterizations and considering  
 625 additional metrics on convective boundary layer simulations (Hourdin et al., 2021).

626 Last but not least, we would like to emphasize that this work was initiated and fos-  
 627 tered during collaborative work sessions dedicated to the transfer of knowledge and critical  
 628 questioning on the physics and assumptions behind the parameterizations used in planetary  
 629 GCMs. Those sessions spontaneously emerged following students' questions and gathered  
 630 atmospheric and planetary scientists experts and non experts of turbulent mixing and pa-  
 631 rameterization development. The motivations behind the ATKE scheme development went  
 632 beyond the need to advance the turbulent diffusion scheme in our models but were also - and  
 633 maybe firstly - a reason and a need to teach and learn the parameterization development in  
 634 a 'learning-by-doing' way.

## 635 Appendix A A gravity-invariant formulation of our TKE-1 turbulent dif- 636 fusion scheme

637 For the sake of universality of a turbulent diffusion parameterization and in particular  
 638 for potential application on different planets, one may want to develop a framework as in-  
 639 dependent as possible upon planet's characteristics, in particular upon planet's gravity. In  
 640 the main paper, gravity appears in the expression of the Brünt Väisälä frequency thus in  
 641 the expression of the gradient Richardson number and in the buoyancy term of the TKE  
 642 evolution equation Eq 7. In this appendix, we briefly introduce a framework using geopo-  
 643 tential as vertical coordinate and in which gravity is no longer involved. Such a framework  
 644 is proposed here as a prospect for a further new implementation of the parameterisation.

Let's introduce the geopotential  $\phi$  defined such that  $d\phi = g dz$  as well as a 're-scaled'  
 time  $\tau$  defined by  $d\tau = g dt$ . The diffusion equation of a quantity  $c$  (Eq. 5) can be written in  
 the form:

$$\frac{\partial c}{\partial \tau} = \frac{1}{\rho} \frac{\partial}{\partial \phi} \left( \rho K_c^\phi \frac{\partial c}{\partial \phi} \right) \quad (\text{A1})$$

645 where  $K_c^\phi = g K_c$ . In such a framework, assuming down-gradient expression of tur-  
 646 bulent fluxes and the same closures for the TKE dissipation and transport terms as in the  
 647 main manuscript, the TKE evolution equation A1 reads:

$$\frac{\partial e}{\partial \tau} = K_m^\phi [(S^\phi)^2 - Pr(Ri)(N^\phi)^2] + \frac{1}{\rho} \frac{\partial}{\partial \phi} (\rho c_e K_m^\phi \frac{\partial e}{\partial \phi}) - \frac{e^{3/2}}{c_\epsilon l^\phi} \quad (\text{A2})$$

648 with  $l^\phi = gl$ ,  $(S^\phi)^2 = (\partial_\phi u)^2 + (\partial_\phi v)^2$  and  $(N^\phi)^2 = \frac{1}{\theta_v} \frac{\partial \theta_v}{\partial \phi}$ .

One can then express  $K_m^\phi = l^\phi(\phi, e, Ri) S_m(Ri) \sqrt{e}$ . Noting the gravity independent  
 form of the gradient Richardson number  $Ri = (N^\phi)^2 / (S^\phi)^2$ , the expressions for  $S_m(Ri)$  and  
 $Pr(Ri)$  can be taken identically from Eq. 20 and 23 as they are gravity-independent. For  
 the mixing length  $l^\phi$  expression, one can use a similar approach as in Sect. 2.4 replacing  
 the neutral-limit formulation with

$$l_n^\phi = \frac{\kappa \phi l_\infty^\phi}{\kappa \phi + l_\infty^\phi} \quad (\text{A3})$$

649  $l_\infty^\phi$  being a tuning parameter. In such a way Eq. A1 and A2 combined with the  
 650 proposed expressions for  $K_m$ ,  $Pr$  and  $l^\phi$  establish a complete gravity-invariant formulation  
 651 of the turbulent diffusion parameterization.

## 652 Open Research Section

653 The latest version of the LMDZ source code can be downloaded freely from the LMDZ  
 654 web site. The version used for the specific simulation runs for this paper is the 'svn' re-  
 655 lease 4781 from 21 December 2023, which can be downloaded and installed on a Linux

656 computer by running the `install_lmdz.sh` script available here: [http://www.lmd.jussieu](http://www.lmd.jussieu.fr/~tilde/pub/install_lmdz.sh)  
 657 [.fr/~tilde/pub/install\\_lmdz.sh](http://www.lmd.jussieu.fr/~tilde/pub/install_lmdz.sh). The Mars PCM used in this work can be down-  
 658 loaded with documentation from the SVN repository at [https://svn.lmd.jussieu.fr/](https://svn.lmd.jussieu.fr/Planeto/trunk/LMDZ.MARS/)  
 659 [Planeto/trunk/LMDZ.MARS/](https://svn.lmd.jussieu.fr/Planeto/trunk/LMDZ.MARS/). Forcings for the GABLS1 single-column cases are provided  
 660 under the DEPHY-SCM standard at the following link: [https://github.com/GdR-DEPHY/](https://github.com/GdR-DEPHY/DEPHY-SCM/)  
 661 [DEPHY-SCM/](https://github.com/GdR-DEPHY/DEPHY-SCM/). GABLS1 LES used in the intercomparison exercise of Beare et al. (2006) are  
 662 distributed here: [https://gabls.metoffice.gov.uk/lem\\_data.html](https://gabls.metoffice.gov.uk/lem_data.html)  
 663 Dome C temperature and wind speed data are freely distributed on PANGAEA data repos-  
 664 itories at <https://doi.org/10.1594/PANGAEA.932512> and [https://doi.org/10.1594/](https://doi.org/10.1594/PANGAEA.932513)  
 665 [PANGAEA.932513](https://doi.org/10.1594/PANGAEA.932513). InSight wind data can be retrieved from the Planetary Data System  
 666 (Jose Rodriguez-Manfredi, 2019).

## 667 Acknowledgments

668 This project has received funding from the European Research Council (ERC) under the  
 669 European Union’s Horizon 2020 research and innovation programme (grant no. 951596)  
 670 through the AWACA project. The part of the work related to the Martian atmosphere is  
 671 supported by the ANR project MAGIS. We acknowledge support from the DEPHY research  
 672 group, funded by CNRS/INSU and Météo-France, as well as from the PEPR TRACCS  
 673 project (no. ANR-22-EXTR-0008) funded from the Agence Nationale de la Recherche -  
 674 France 2030. Éric Bazile is gratefully acknowledged for fruitful discussions. This study was  
 675 conducted using the ESPRI (Ensemble de Services Pour la Recherche l’IPSL) computing and  
 676 data center (<https://mesocentre.ipsl.fr>) which is supported by CNRS, Sorbonne Université,  
 677 Ecole Polytechnique, and CNES and through national and international grants. Simulations  
 678 were performed using HPC resources from the IDRIS (Institut du Développement et des  
 679 Ressources en Informatique Scientifique, CNRS, France), project RLMD AD010107632R1.  
 680 Simulations with the Mars PCM were performed using HPC resources of Centre Informa-  
 681 tique National de l’Enseignement Supérieur (CINES) under the allocation n°A0100110391  
 682 made by Grand Equipement National de Calcul Intensif (GENCI).

## 683 References

- 684 Acevedo, O. C., Mahrt, L., Puhales, F. S., Costa, F. D., Medeiros, L. E., & Degrazia, G. A.  
 685 (2015). Contrasting structures between the decoupled and coupled states of the stable  
 686 boundary layer. *Q J R Meteorol Soc*, *142*(695), 693-702. (doi: 10.1002/qj.2693)
- 687 André, J. C., Moor, G. D., Lacarrère, P., & du Vachat, R. (1978). Model-  
 688 ing the 24-hour evolution of the mean and turbulent structures of the plane-  
 689 tary boundary layer. *Journal of Atmospheric Sciences*, *35*(10), 1861 - 1883.  
 690 Retrieved from [https://journals.ametsoc.org/view/journals/atsc/35/10/1520-](https://journals.ametsoc.org/view/journals/atsc/35/10/1520-0469_1978_035_1861_mtheot_2_0_co_2.xml)  
 691 [-0469\\_1978\\_035\\_1861\\_mtheot\\_2\\_0\\_co\\_2.xml](https://journals.ametsoc.org/view/journals/atsc/35/10/1520-0469_1978_035_1861_mtheot_2_0_co_2.xml) doi: [https://doi.org/10.1175/1520-](https://doi.org/10.1175/1520-0469(1978)035(1861:MTHEOT)2.0.CO;2)  
 692 [-0469\(1978\)035\(1861:MTHEOT\)2.0.CO;2](https://doi.org/10.1175/1520-0469(1978)035(1861:MTHEOT)2.0.CO;2)
- 693 Audouin, O., Roehrig, R., Couvreux, F., & Williamson, D. (2021). Modeling the gabls4  
 694 strongly-stable boundary layer with a gcm turbulence parameterization: Parametric  
 695 sensitivity or intrinsic limits? *Journal of Advances in Modeling Earth Systems*, *13*(3),  
 696 e2020MS002269. doi: <https://doi.org/10.1029/2020MS002269>
- 697 Baas, P., Van De Wiel, B., Van der Linden, S., & Bosveld, F. (2018). From near-neutral to  
 698 strongly stratified: Adequately modelling the clear-sky nocturnal boundary layer at  
 699 cabauw. *Boundary-Layer Meteorology*, *166*, 217–238.
- 700 Baas, P., van de Wiel, B. J. H., van Meijgaard, E., Vignon, E., Genthon, C., van der  
 701 Linden, S. J. A., & de Roode, S. R. (2019). Transitions in the wintertime near-  
 702 surface temperature inversion at dome c, antarctica. *Quarterly Journal of the Royal*  
 703 *Meteorological Society*, *145*(720), 930-946. doi: <https://doi.org/10.1002/qj.3450>
- 704 Banfield, D., Spiga, A., Newman, C., Forget, F., Lemmon, M., Lorenz, R., . . . others (2020).  
 705 The atmosphere of mars as observed by insight. *Nature Geoscience*, *13*(3), 190–198.
- 706 Bazile, E., Marquet, P., Bouteloup, Y., & Bouyssel, F. (2011). The turbulent kinetic energy

- (tke) scheme in the nwp models at météo-france. In *Workshop on diurnal cycles and the stable boundary layer, ecmwf* (pp. 127–136).
- 707  
708
- 709 Beare, R. J., Macvean, M. K., Holtslag, A. A. M., Cuxart, J., Esau, I., Golaz, J.-C.,  
710 ... Sullivan, P. (2006). An intercomparison of large-eddy simulations of the stable  
711 boundary layer. *Boundary-Layer Meteorology*, *118*(2), 247–272. doi: 10.1007/s10546-  
712 -004-2820-6
- 713 Betts, A. K. (1973). Non-precipitating cumulus convection and its parameteri-  
714 zation. *Quarterly Journal of the Royal Meteorological Society*, *99*(419), 178-  
715 196. Retrieved from [https://rmets.onlinelibrary.wiley.com/doi/abs/10.1002/](https://rmets.onlinelibrary.wiley.com/doi/abs/10.1002/qj.49709941915)  
716 [qj.49709941915](https://rmets.onlinelibrary.wiley.com/doi/abs/10.1002/qj.49709941915) doi: <https://doi.org/10.1002/qj.49709941915>
- 717 Blackadar, A. K. (1962). The vertical distribution of wind and turbulent exchange in neutral  
718 atmosphere. *J Geophys Res*, *67*, 3095-3102.
- 719 Boucher, O., Servonnat, J., Albright, A. L., Aumont, O., Balkanski, Y., Bastrikov, V.,  
720 ... Vuichard, N. (2020). Presentation and evaluation of the ipsl-cm6a-lr climate  
721 model. *Journal of Advances in Modeling Earth Systems*, *12*(7), e2019MS002010. doi:  
722 10.1029/2019MS002010
- 723 Bougeault, P., & Lacarrère, P. (1989). Parametrization of orography-induced turbulence in  
724 a mesobeta-scale model. *Monthly-Weather Rev*, *117*, 1872-1891.
- 725 Chatain, A., Spiga, A., Banfield, D., Forget, F., & Murdoch, N. (2021). Sea-  
726 sonal variability of the daytime and nighttime atmospheric turbulence experi-  
727 enced by insight on mars. *Geophysical Research Letters*, *48*(22), e2021GL095453.  
728 Retrieved from [https://agupubs.onlinelibrary.wiley.com/doi/abs/10.1029/](https://agupubs.onlinelibrary.wiley.com/doi/abs/10.1029/2021GL095453)  
729 [2021GL095453](https://agupubs.onlinelibrary.wiley.com/doi/abs/10.1029/2021GL095453) doi: <https://doi.org/10.1029/2021GL095453>
- 730 Chen, W., Lovejoy, S., & Muller, J.-P. (2016). Mars’ atmosphere: The sister planet,  
731 our statistical twin. *Journal of Geophysical Research: Atmospheres*, *121*(20), 11,968-  
732 11,988. doi: <https://doi.org/10.1002/2016JD025211>
- 733 Cheruy, F., Ducharne, A., Hourdin, F., Musat, I., Vignon, , Gastineau, G., ... Zhao, Y.  
734 (2020). Improved near-surface continental climate in ipsl-cm6a-lr by combined evolu-  
735 tions of atmospheric and land surface physics. *Journal of Advances in Modeling Earth*  
736 *Systems*, *12*(10), e2019MS002005. doi: <https://doi.org/10.1029/2019MS002005>
- 737 Colaitis, A., Spiga, A., Hourdin, F., Rio, C., Forget, F., & Millour, E. (2013). A ther-  
738 mal plume model for the Martian convective boundary layer. *Journal of Geophysical*  
739 *Research: Planets*, *118*(7), 1468-1487. doi: 10.1002/jgre.20104
- 740 Couvreur, F., Bazile, E., Rodier, Q., Maronga, B., Matheou, G., Chinita, M. J., ... others  
741 (2020). Intercomparison of large-eddy simulations of the antarctic boundary layer  
742 for very stable stratification. *Boundary-Layer Meteorology*, *176*(3), 369–400. doi:  
743 10.1007/s10546-020-00539-4
- 744 Couvreur, F., Hourdin, F., Williamson, D., Roehrig, R., Volodina, V., Villefranche, N., ...  
745 Xu, W. (2021). Process-based climate model development harnessing machine learn-  
746 ing: I. a calibration tool for parameterization improvement. *Journal of Advances in*  
747 *Modeling Earth Systems*, *13*(3), e2020MS002217. Retrieved from [https://agupubs](https://agupubs.onlinelibrary.wiley.com/doi/abs/10.1029/2020MS002217)  
748 [.onlinelibrary.wiley.com/doi/abs/10.1029/2020MS002217](https://agupubs.onlinelibrary.wiley.com/doi/abs/10.1029/2020MS002217) doi: [https://doi](https://doi.org/10.1029/2020MS002217)  
749 [.org/10.1029/2020MS002217](https://doi.org/10.1029/2020MS002217)
- 750 Cuxart, J., Holtslag, A. A. M., Beare, R. J., Bazile, E., Beljaars, A., Cheng, A., ... Xu, K.-  
751 M. (2006). Single-column model intercomparison for a stably stratified atmospheric  
752 boundary layer. *Boundary-Layer Meteorol*, *118*(2), 273-303. (doi:10.1007/s10546-005-  
753 3780-1)
- 754 Deardoff, J. W. (1980). Stratocumulus-capped mixed layers derived from a threee dimen-  
755 sionnal model. *Boundary-Layer Meteorol*, *18*, 495-527.
- 756 Delage, Y. (1997). Parametrising sub-grid scale vertical transport in atmospheric models  
757 under statically stable conditions. *Boundary-Layer Meteorol*, *82*, 23-48.
- 758 Deleersnijder, E. (1992). *Modélisation hydrodynamique tridimensionnelle de la circulation*  
759 *générale estivale de la région du détroit de bering (in french)* (Unpublished doctoral  
760 dissertation). Université Catholique de Louvain.
- 761 Derbyshire, S. H. (1990). Nieuwstadt’s stable boundary layer revisited. *Q J R Meteorol*

- 762           *Soc*, 126, 127-158.
- 763 Dufresne, J.-L., & Ghattas, J. (2009). Description du schéma de la couche limite turbulente  
764 et l'interface avec la surface planétaire dans lmdz. *ORCHIDEE documentation*.  
765 Retrieved from [http://forge.ipsl.jussieu.fr/orchidee/attachment/wiki/](http://forge.ipsl.jussieu.fr/orchidee/attachment/wiki/Documentation/CouplingLMDZ/Dufresne,%20Ghattas%20-%202009-Coupling-ORC-LMDZ.pdf)  
766 [Documentation/CouplingLMDZ/Dufresne,%20Ghattas%20-%202009-Coupling](http://forge.ipsl.jussieu.fr/orchidee/attachment/wiki/Documentation/CouplingLMDZ/Dufresne,%20Ghattas%20-%202009-Coupling-ORC-LMDZ.pdf)  
767 [-ORC-LMDZ.pdf](http://forge.ipsl.jussieu.fr/orchidee/attachment/wiki/Documentation/CouplingLMDZ/Dufresne,%20Ghattas%20-%202009-Coupling-ORC-LMDZ.pdf) (in french)
- 768 Edwards, J. M. (2009). Radiative processes in the stable boundary layer: Part i. radiatives  
769 aspects. *Boundary-Layer Meteorology*, 131(1). doi: 10.1007/s10546-009-9364-8
- 770 Emanuel, K. A. (1991). A scheme for representing cumulus convection in large-scale models.  
771 *Journal of Atmospheric Sciences*, 48(21), 2313 - 2329. doi: [https://doi.org/10.1175/](https://doi.org/10.1175/1520-0469(1991)048(2313:ASFRCC)2.0.CO;2)  
772 [1520-0469\(1991\)048\(2313:ASFRCC\)2.0.CO;2](https://doi.org/10.1175/1520-0469(1991)048(2313:ASFRCC)2.0.CO;2)
- 773 England, D. E., & McNider, R. T. (1995). Stability functions based upon shear functions.  
774 *Boundary-Layer Meteorol*, 74, 113-130.
- 775 Forget, F., Banfield, D., Spiga, A., Millour, E., Borella, A., Lange, L., ... Banerdt, W. B.  
776 (2021). More than one Martian year of meteorology observed by the InSight Lander. In  
777 *European planetary science congress* (p. EPSC2021-273). doi: 10.5194/epsc2021-273
- 778 Forget, F., Hourdin, F., Fournier, R., Hourdin, C., Talagrand, O., Collins, M., ... Huot,  
779 J.-P. (1999). Improved general circulation models of the martian atmosphere from  
780 the surface to above 80 km. *Journal of Geophysical Research: Planets*, 104(E10),  
781 24155-24175. Retrieved from [https://agupubs.onlinelibrary.wiley.com/doi/](https://agupubs.onlinelibrary.wiley.com/doi/abs/10.1029/1999JE001025)  
782 [abs/10.1029/1999JE001025](https://agupubs.onlinelibrary.wiley.com/doi/abs/10.1029/1999JE001025) doi: <https://doi.org/10.1029/1999JE001025>
- 783 Genthon, C., Veron, D., Vignon, E., Six, D., Dufresne, J.-L., Madeleine, J.-B., ... Forget,  
784 F. (2021). 10 years of temperature and wind observation on a 45 m tower at dome  
785 c, east antarctic plateau. *Earth System Science Data*, 13(12), 5731-5746. Retrieved  
786 from <https://essd.copernicus.org/articles/13/5731/2021/> doi: 10.5194/essd-  
787 13-5731-2021
- 788 Girard, C., & Delage, Y. (1990). Stable schemes for nonlinear vertical diffusion  
789 in atmospheric circulation models. *Monthly Weather Review*, 118(3), 737 -  
790 745. Retrieved from [https://journals.ametsoc.org/view/journals/mwre/118/](https://journals.ametsoc.org/view/journals/mwre/118/3/1520-0493_1990_118_0737_ssfvnd.2_0.co_2.xml)  
791 [3/1520-0493\\_1990\\_118\\_0737\\_ssfvnd.2\\_0.co\\_2.xml](https://journals.ametsoc.org/view/journals/mwre/118/3/1520-0493_1990_118_0737_ssfvnd.2_0.co_2.xml) doi: [https://doi.org/10.1175/](https://doi.org/10.1175/1520-0493(1990)118(0737:SSFNVD)2.0.CO;2)  
792 [1520-0493\(1990\)118\(0737:SSFNVD\)2.0.CO;2](https://doi.org/10.1175/1520-0493(1990)118(0737:SSFNVD)2.0.CO;2)
- 793 Golaz, J.-C., Larson, V. E., & Cotton, W. R. (2002). A pdf-based model for boundary  
794 layer clouds. part i: Method and model description. *Journal of the Atmospheric*  
795 *Sciences*, 59(24), 3540 - 3551. Retrieved from [https://journals.ametsoc.org/](https://journals.ametsoc.org/view/journals/atsc/59/24/1520-0469_2002_059_3540_apbmf.2_0.co_2.xml)  
796 [view/journals/atsc/59/24/1520-0469\\_2002\\_059\\_3540\\_apbmf.2\\_0.co\\_2.xml](https://journals.ametsoc.org/view/journals/atsc/59/24/1520-0469_2002_059_3540_apbmf.2_0.co_2.xml) doi:  
797 [https://doi.org/10.1175/1520-0469\(2002\)059\(3540:APBMFB\)2.0.CO;2](https://doi.org/10.1175/1520-0469(2002)059(3540:APBMFB)2.0.CO;2)
- 798 Grisogono, B. (2010). Generalizing 'z-less' mixing length for stable boundary layers.  
799 *Quarterly Journal of the Royal Meteorological Society*, 136(646), 213-221. doi:  
800 <https://doi.org/10.1002/qj.529>
- 801 Grisogono, B., & Belušić, D. (2008). Improving mixing length-scale for stable boundary lay-  
802 ers. *Quarterly Journal of the Royal Meteorological Society*, 134(637), 2185-2192. Re-  
803 trieved from <https://rmets.onlinelibrary.wiley.com/doi/abs/10.1002/qj.347>  
804 doi: <https://doi.org/10.1002/qj.347>
- 805 He, Y., McFarlane, N. A., & Monahan, A. H. (2019). A new tke-based parameterization of  
806 atmospheric turbulence in the canadian global and regional climate models. *Journal of*  
807 *Advances in Modeling Earth Systems*, 11(5), 1153-1188. doi: [https://doi.org/10.1029/](https://doi.org/10.1029/2018MS001532)  
808 [2018MS001532](https://doi.org/10.1029/2018MS001532)
- 809 Hersbach, H., Bell, B., Berrisford, P., Hirahara, S., Horányi, A., Muñoz-Sabater, J., ...  
810 Thépaut, J.-N. (2020). The era5 global reanalysis. *Quarterly Journal of the Royal*  
811 *Meteorological Society*, 146, 1999-2049. doi: 10.1002/qj.3803
- 812 Holtslag, A. A. M., & Boville, B. A. (1993). Local versus non-local boundary layer diffusion  
813 in a global climate model. *J Clim*, 6, 1825-1842.
- 814 Holtslag, A. A. M., Svensson, G., Baas, P., Basu, S., Beare, B., Beljaars, A. C. M., ...  
815 Van de Wiel, B. J. H. (2013). Stable boundary layers and diurnal cycles. *Bull Amer*  
816 *Meteor Soc*, 94, 1691-1706. (doi:10.1175/BAMS-D-11-00187.1.)

- 817 Hourdin, F., Couvreaux, F., & Menut, L. (2002). Parameterization of the dry convective  
818 boundary layer based on a mass flux representation of thermals. *J Atmos Sci*, *59*,  
819 1105-1123.
- 820 Hourdin, F., Jam, A., Rio, C., Couvreaux, F., Sandu, I., Lefebvre, M.-P., ... Idelkadi, A.  
821 (2019). Unified parameterization of convective boundary layer transport and clouds  
822 with the thermal plume model. *Journal of Advances in Modeling Earth Systems*,  
823 *11*(9), 2910-2933. doi: <https://doi.org/10.1029/2019MS001666>
- 824 Hourdin, F., Rio, C., Grandpeix, J.-Y., Madeleine, J.-B., Cheruy, F., Rochetin, N., ...  
825 Ghattas, J. (2020). Lmdz6a: the atmospheric component of the ipsl climate model  
826 with improved and better tuned physics. *Journal of Advances in Modeling Earth*  
827 *Systems*. doi: 10.1029/2019MS001892
- 828 Hourdin, F., Williamson, D., Rio, C., Couvreaux, F., Roehrig, R., Villefranque, N., ...  
829 Volodina, V. (2021). Process-based climate model development harnessing machine  
830 learning: Ii. model calibration from single column to global. *Journal of Advances in*  
831 *Modeling Earth Systems*, *13*(6), e2020MS002225. Retrieved from [https://agupubs](https://agupubs.onlinelibrary.wiley.com/doi/abs/10.1029/2020MS002225)  
832 [.onlinelibrary.wiley.com/doi/abs/10.1029/2020MS002225](https://agupubs.onlinelibrary.wiley.com/doi/abs/10.1029/2020MS002225) doi: [https://doi](https://doi.org/10.1029/2020MS002225)  
833 [.org/10.1029/2020MS002225](https://doi.org/10.1029/2020MS002225)
- 834 Jose Rodriguez-Manfredi. (2019). *Apss twins data*. NASA Planetary Data System. Re-  
835 trieved from [https://pds.nasa.gov/ds-view/pds/viewBundle.jsp?identifier=](https://pds.nasa.gov/ds-view/pds/viewBundle.jsp?identifier=urn:nasa:pds:insight_twins&version=3.2)  
836 [urn:nasa:pds:insight\\_twins&version=3.2](https://pds.nasa.gov/ds-view/pds/viewBundle.jsp?identifier=urn:nasa:pds:insight_twins&version=3.2) doi: 10.17189/1518950
- 837 Kahre, M. A., Murphy, J. R., Newman, C. E., Wilson, R. J., Cantor, B. A., Lemmon, M. T.,  
838 & Wolff, M. J. (2017). The Mars dust cycle. In *The atmosphere and climate of Mars*  
839 (p. 295-337). Cambridge University Press. doi: 10.1017/9781139060172.010
- 840 Kalnay, E., & Kanamitsu, M. (1988). Time schemes for strongly nonlinear  
841 damping equations. *Monthly Weather Review*, *116*(10), 1945 - 1958. Re-  
842 trieved from [https://journals.ametsoc.org/view/journals/mwre/116/10/1520](https://journals.ametsoc.org/view/journals/mwre/116/10/1520-0493_1988_116_1945_tsfsnd_2_0_co_2.xml)  
843 [-0493\\_1988\\_116\\_1945\\_tsfsnd\\_2\\_0\\_co\\_2.xml](https://journals.ametsoc.org/view/journals/mwre/116/10/1520-0493_1988_116_1945_tsfsnd_2_0_co_2.xml) doi: [https://doi.org/10.1175/1520](https://doi.org/10.1175/1520-0493(1988)116(1945:TSFSND)2.0.CO;2)  
844 [-0493\(1988\)116\(1945:TSFSND\)2.0.CO;2](https://doi.org/10.1175/1520-0493(1988)116(1945:TSFSND)2.0.CO;2)
- 845 Kolmogorov, A. N. (1941). Energy dissipation in locally isotropic turbulence. *Doklady AN*  
846 *SSSR*, *32*, 19-21.
- 847 Lange, L., Forget, F., Dupont, E., Vandemeulebrouck, R., Spiga, A., Millour, E., ...  
848 Bierjon, A. (2023). Modeling slope microclimates in the mars planetary climate  
849 model. *Journal of Geophysical Research: Planets*, *128*(10), e2023JE007915. doi:  
850 10.1029/2023JE007915
- 851 Lenderink, G., & Holtslag, A. A. M. (2000). Evaluation of the kinetic energy approach  
852 for modeling turbulent fluxes in stratocumulus. *Monthly Weather Review*, *128*(1), 244  
853 - 258. Retrieved from [https://journals.ametsoc.org/view/journals/mwre/128/](https://journals.ametsoc.org/view/journals/mwre/128/1/1520-0493_2000_128_0244_eotkea_2_0_co_2.xml)  
854 [1/1520-0493\\_2000\\_128\\_0244\\_eotkea\\_2\\_0\\_co\\_2.xml](https://journals.ametsoc.org/view/journals/mwre/128/1/1520-0493_2000_128_0244_eotkea_2_0_co_2.xml) doi: [https://doi.org/10.1175/](https://doi.org/10.1175/1520-0493(2000)128(0244:EOTKEA)2.0.CO;2)  
855 [1520-0493\(2000\)128\(0244:EOTKEA\)2.0.CO;2](https://doi.org/10.1175/1520-0493(2000)128(0244:EOTKEA)2.0.CO;2)
- 856 Lenderink, G., & Holtslag, A. A. M. (2004). An updated length-scale formulation for  
857 turbulent mixing in clear and cloudy boundary layers. *Quarterly Journal of the*  
858 *Royal Meteorological Society*, *130*(604), 3405-3427. Retrieved from [https://rmets](https://rmets.onlinelibrary.wiley.com/doi/abs/10.1256/qj.03.117)  
859 [.onlinelibrary.wiley.com/doi/abs/10.1256/qj.03.117](https://rmets.onlinelibrary.wiley.com/doi/abs/10.1256/qj.03.117) doi: [https://doi.org/](https://doi.org/10.1256/qj.03.117)  
860 [10.1256/qj.03.117](https://doi.org/10.1256/qj.03.117)
- 861 Li, D. (2019). Turbulent prandtl number in the atmospheric boundary layer - where  
862 are we now? *Atmospheric Research*, *216*, 86-105. Retrieved from [https://](https://www.sciencedirect.com/science/article/pii/S0169809518307324)  
863 [www.sciencedirect.com/science/article/pii/S0169809518307324](https://www.sciencedirect.com/science/article/pii/S0169809518307324) doi: [https://](https://doi.org/10.1016/j.atmosres.2018.09.015)  
864 [doi.org/10.1016/j.atmosres.2018.09.015](https://doi.org/10.1016/j.atmosres.2018.09.015)
- 865 Li, D., Katul, G. G., & Zilitinkevich, S. S. (2016). Closure schemes for stably stratified  
866 atmospheric flows without turbulence cutoff. *Journal of the Atmospheric Sciences*,  
867 *73*(12), 4817 - 4832. doi: <https://doi.org/10.1175/JAS-D-16-0101.1>
- 868 Louis, J.-F. (1979). A parametric model of vertical eddy fluxes in the atmosphere. *Boundary-*  
869 *Layer Meteorol*, *17*, 187-202. (doi: 10.1007/BF00712379)
- 870 Louis, J. F., Tiedtke, M., & Geleyn, J.-F. (1982). A short history of the operational pbl  
871 parametrization at ECMWF. *Paper presented at the ECMWF workshop on boundary*

- 872 *layer parametrization, ECMWF, Reading.*
- 873 Mašek, J., Ďurán, I. B., & Brožková, R. (2022). Stable numerical implementation of  
874 a turbulence scheme with two prognostic turbulence energies. *Monthly Weather*  
875 *Review*, 150(7), 1667 - 1688. Retrieved from [https://journals.ametsoc.org/  
876 view/journals/mwre/150/7/MWR-D-21-0172.1.xml](https://journals.ametsoc.org/view/journals/mwre/150/7/MWR-D-21-0172.1.xml) doi: [https://doi.org/10.1175/  
877 MWR-D-21-0172.1](https://doi.org/10.1175/MWR-D-21-0172.1)
- 878 Mellor, G. L., & Yamada, T. (1974). A hierarchy of turbulence closure models for planetary  
879 boundary layers. *J Atmos Sci*, 30, 1061-1069.
- 880 Mellor, G. L., & Yamada, T. (1982). Development of a turbulence closure model for  
881 geophysical fluid problems. *Rev Geophys Space Phys*, 20(4), 851-875.
- 882 Montabone, L., Forget, F., Millour, E., Wilson, R., Lewis, S., Cantor, B., ... Wolff, M.  
883 (2015). Eight-year climatology of dust optical depth on mars. *Icarus*, 251, 65–95. doi:  
884 10.1016/j.icarus.2014.12.034
- 885 Nieuwtsadt, F. T. M. (1984). The turbulent structure of the stable, nocturnal boundary  
886 layer. *J Atmos Sci*, 41, 2202-2217.
- 887 Petrosyan, A., Galperin, B., Larsen, S. E., Lewis, S. R., Määttänen, A., Read, P. L., ...  
888 Vázquez, L. (2011). The martian atmospheric boundary layer. *Reviews of Geo-*  
889 *physics*, 49(3). Retrieved from [https://agupubs.onlinelibrary.wiley.com/doi/  
890 abs/10.1029/2010RG000351](https://agupubs.onlinelibrary.wiley.com/doi/abs/10.1029/2010RG000351) doi: <https://doi.org/10.1029/2010RG000351>
- 891 Pottier, A., Forget, F., Montmessin, F., Navarro, T., Spiga, A., Millour, E., ... Madeleine,  
892 J.-B. (2017). Unraveling the martian water cycle with high-resolution global climate  
893 simulations. *Icarus*, 291, 82–106. doi: 10.1016/j.icarus.2017.02.016
- 894 Rio, C., Hourdin, F., Couvreur, F., & Jam, A. (2010). Resolved versus parametrized  
895 boundary-layer plumes. Part II: continuous formulations of mixing rates for mass-flux  
896 schemes. *Boundary-layer Meteorol.* (Doi:10.1007/s10546-010-9478)
- 897 Rodier, Q., Masson, V., Couvreur, F., & Paci, A. (2017). Evaluation of a buoyancy and  
898 shear based mixing length for a turbulence scheme. *Frontiers in Earth Science*, 5, 65.  
899 doi: 10.3389/feart.2017.00065
- 900 Sandu, I., Beljaars, A., Bechtold, P., Mauritsen, T., & Balsamo, G. (2013). Why is it so  
901 difficult to represent stably stratified conditions in numerical weather prediction (nwp)  
902 models. *J Adv Model Earth Syst*, 5, 117-133. (doi: 10.1002/jame.20013)
- 903 Spiga, A., Forget, F., Lewis, S. R., & Hinson, D. P. (2010a). Structure and dynamics of  
904 the convective boundary layer on mars as inferred from large-eddy simulations and  
905 remote-sensing measurements. *Quarterly Journal of the Royal Meteorological Society*,  
906 136(647), 414-428. Retrieved from [https://rmets.onlinelibrary.wiley.com/doi/  
907 abs/10.1002/qj.563](https://rmets.onlinelibrary.wiley.com/doi/abs/10.1002/qj.563) doi: <https://doi.org/10.1002/qj.563>
- 908 Spiga, A., Forget, F., Lewis, S. R., & Hinson, D. P. (2010b). Structure and dynamics of  
909 the convective boundary layer on Mars as inferred from large-eddy simulations and  
910 remote-sensing measurements. *Quarterly Journal of the Royal Meteorological Society*,  
911 136(647), 414-428. doi: 10.1002/qj.563
- 912 Stull, R. B. (1990). *An introduction to boundary layer meteorology*. Kluwer, Boston.
- 913 Sun, J. (2011). Vertical variations of mixing lengths under neutral and stable conditions  
914 during cases-99. *Journal of Applied Meteorology and Climatology*, 50(10), 2030 - 2041.  
915 Retrieved from [https://journals.ametsoc.org/view/journals/apme/50/10/jamc-  
916 -d-10-05006.1.xml](https://journals.ametsoc.org/view/journals/apme/50/10/jamc-d-10-05006.1.xml) doi: <https://doi.org/10.1175/JAMC-D-10-05006.1>
- 917 Tiedtke, M. (1989). A comprehensive mass flux scheme for cumulus parameterization in  
918 large-scale models. *Monthly Weather Review*, 117(8), 1779 - 1800. doi: [https://  
919 doi.org/10.1175/1520-0493\(1989\)117<1779:ACMFSF>2.0.CO;2](https://doi.org/10.1175/1520-0493(1989)117<1779:ACMFSF>2.0.CO;2)
- 920 van der Linden, S. J., Edwards, J. M., van Heerwaarden, C. C., Vignon, E., Genthon, C.,  
921 Petenko, I., ... van de Wiel, B. J. (2019). Large-eddy simulations of the steady  
922 wintertime antarctic boundary layer. *Boundary-Layer Meteorology*, 173(2), 165–192.  
923 doi: 10.1007/s10546-019-00461-4
- 924 van de Wiel, B. J. H., Moene, A. F., H., D. R. W., & Jonker, H. J. J. (2008). Local similarity  
925 in the stable boundary layer and mixing-length approaches: consistency of concepts.  
926 *Boundary-Layer Meteorol*, 128, 103-116.

- 927 van de Wiel, B. J. H., Moene, A. F., Steeneveld, G. J., Baas, P., Bosveld, F. C., & Holstlag,  
 928 A. A. M. (2010). A conceptual view on inertial oscillations and nocturnal low-level  
 929 jets. *J Atmos Sci*, *67*, 2679-2689. (doi: 10.1175/2010JAS3289.1)
- 930 van de Wiel, B. J. H., Vignon, E., Baas, P., van Hooijdonk, I. G. S., van der Linden,  
 931 S. J. A., van Hooft, J. A., ... Genthon, C. (2017). Regime transition in near-  
 932 surface temperature inversions: a conceptual model. *J Atmos Sci*, *74*, 1057-1073.  
 933 (doi:10.1175/JAS-D-16-0180.1)
- 934 Venayagamoorthy, S. K., & Stretch, D. D. (2010). On the turbulent prandtl number in  
 935 homogeneous stably stratified turbulence. *Journal of Fluid Mechanics*, *644*, 359-369.  
 936 doi: 10.1017/S002211200999293X
- 937 Vignon, E., Hourdin, F., Genthon, C., Gallée, H., Bazile, E., Lefebvre, M.-P., ... Van de  
 938 Wiel, B. J. H. (2017). Parametrization of the boundary layer over the antarctic plateau  
 939 in a general circulation model: 1D simulations against summertime observations at  
 940 Dome C. *J Geophys Res Atmos*, *122*. (doi: 10.1002/2017JD026802)
- 941 Vignon, E., Hourdin, F., Genthon, C., Van de Wiel, B. J. H., , Gallée, H., ... Beaumet, J.  
 942 (2018). Modeling the dynamics of the atmospheric boundary layer over the antarctic  
 943 plateau with a general circulation model. *Journal of Advances in Modeling Earth*  
 944 *Systems*. (10.1002/2017MS001184)
- 945 Vignon, E., van de Wiel, B. J. H., van Hooijdonk, I. G. S., Genthon, C., van der Linden,  
 946 S. J. A., van Hooft, J. A., ... Casasanta, G. (2017). Stable boundary layer regimes  
 947 at Dome C, Antarctica: observation and analysis. *Q J R Meteorol Soc*, *143*(704),  
 948 1241-1253. (doi:10.1002/qj.2998)
- 949 Weiss, B. P., & Ingersoll, A. P. (2000). Cold spots in the martian polar regions: Evidence  
 950 of carbon dioxide depletion? *Icarus*, *144*(2), 432-435. doi: 10.1006/icar.1999.6302
- 951 Yamada, T. (1975). A simulation of the wangara atmospheric boundary layer data. *J Atmos*  
 952 *Sci*, *32*, 2309-2320.
- 953 Yamada, T. (1983). Simulations of nocturnal drainage flows by a  $q^2l$  turbulence closure  
 954 model. *J Atmos Sci*, *40*, 91-106.
- 955 Zilitinkevich, S., Elperin, T., Kleeorin, N., & Rogachevskii, I. (2007). Energy and flux-  
 956 budget turbulence closure model for stably stratified flows. Part I: Steady state, ho-  
 957 mogeneous regime. *Boundary-Layer Meteorol*, *125*, 167-191. (doi:10.1007/s10546-007-  
 958 9189-2)
- 959 Zilitinkevich, S., Elperin, T., Kleeorin, N., Rogachevskii, I., Esau, I., Mauritsen, T., & Miles,  
 960 M. W. (2008). Turbulence energetics in stably stratified geophysical flows: Strong  
 961 and weak mixing regimes. *Q J R Meteorol Soc*, *134*, 793-799. (doi:10.1002/qj.264)